Nonlinear Reduced Order Modeling of Structures Exhibiting a Strong Nonlinearity

by

Jinshan Lin

A Dissertation Presented in Partial Fulfillment
of the requirements for the Degree of
Doctor of Philosophy

Approved March 2020 by the
Graduate Supervisory Committee:

Marc Mignolet, Chair
Hanqing Jiang
Jay Oswald
Stephen Spottswood
Subramaniam Rajan

ARIZONA STATE UNIVERSITY

May 2020

ABSTRACT

The focus of this dissertation is first on understanding the difficulties involved in constructing reduced order models of structures that exhibit a strong nonlinearity/strongly nonlinear events such as snap-through, buckling (local or global), mode switching, symmetry breaking. Next, based on this understanding, it is desired to modify/extend the current Nonlinear Reduced Order Modeling (NLROM) methodology, basis selection and/or identification methodology, to obtain reliable reduced order models of these structures. Focusing on these goals, the work carried out addressed more specifically the following issues:

i) optimization of the basis to capture at best the response in the smallest number of modes,

ii) improved identification of the reduced order model stiffness coefficients,

iii) detection of strongly nonlinear events using NLROM.

For the first issue, an approach was proposed to rotate a limited number of linear modes to become more dominant in the response of the structure. This step was achieved through a proper orthogonal decomposition of the projection on these linear modes of a series of representative nonlinear displacements. This rotation does not expand the modal space but renders that part of the basis more efficient, the identification of stiffness coefficients more reliable, and the selection of dual modes more compact. In fact, a separate approach was also proposed for an independent optimization of the duals. Regarding the second issue, two tuning approaches of the stiffness coefficients were proposed to improve the identification of a limited set of

critical coefficients based on independent response data of the structure. Both approaches led to a significant improvement of the static prediction for the clamped-clamped curved beam model. Extensive validations of the NLROMs based on the above novel approaches was carried out by comparisons with full finite element response data. The third issue, the detection of nonlinear events, was finally addressed by building connections between the eigenvalues of the finite element software (Nastran here) and NLROM tangent stiffness matrices and the occurrence of the 'events' which is further extended to the assessment of the accuracy with which the NLROM captures the full finite element behavior after the event has occurred.

ACKNOWLEDGEMENTS

Firstly, I would like to express my very great appreciation to my advisor Dr. Mignolet for his valuable and constructive suggestions during the planning and development of this research work. Without his guidance the work would not have been finished. His willingness to give his time so generously has been very much appreciated. Besides, I would like to offer my special thanks to Dr. Julian Wang for his patient instructions whenever I met problem and technical support during the research. My grateful thanks are also extended to Dr. Murthy, Dr. Song, Bret Wainwright and Dr. Yuting Wang for nice discussions when I met problem in research. Additionally, my sincere thank also goes to Dr. Jiang who provided me lab support in my first year of PhD study. I would like to thank Dr. Oswald, Dr. Rajan and Dr. Spottswood for serving on my committee. Last but not the least, I gratefully acknowledge the support of this work by the AFRL-University Collaborative Center in Structural Sciences (Cooperative Agreement FA8650-13-2-2347) with Dr. Ben Smarslok as program manager.

TABLE OF CONTENTS

Page

CHAPTER Page

CHAPTER Page

LIST OF TABLES

Table Page

Table Page

LIST OF FIGURES

Figure Page

Figure Page

Figure Page

Figure Page

Figure Page

Figure Page

Figure Page

Figure Page

Figure Page

Figure Page

Figure Page

Figure Page

Figure Page

CHAPTER 1 INTRODUCTION AND BACKGROUND

In the last 4 decades, finite element methods have revolutionized structural analyses and design by providing the capability to model complex geometries, boundary conditions, loadings, and material properties and provide results with guaranteed accuracy, potential for refinement, and, generally speaking, speed. Commercial finite element software, such as Nastran, ABAQUS, and ANSYS have extraordinary arrays of elements, boundary conditions, solutions schemes, to address a wide variety of problems. While these capabilities were growing and the computing speeds and resources were increasing so were the demands: long term dynamic analyses necessary to estimate fatigue life, geometric and material nonlinearities to reflect large deformations of more flexible or more heavily loaded structures, multi-physics analyses to reflect the coupling of the structure with its surrounding, consideration of uncertainties, etc. While these advanced capabilities are available in commercial finite element software, they come with substantial CPU time penalty that prevent them from being used as efficient design tools.

If the structure can be assumed to behave linearly, most of the above requirements can be fairly easily met by using modal methods in which the response of the structure can be expanded in terms of a very limited number of its modes thereby providing a dramatic reduction of the computations. Moreover, these modes can be determined from the underlying finite element model and thus modal analysis complements the finite element methodology to enable a series of additional capabilities.

A similar effort for structures in the nonlinear geometric regime was initiated by at least 2001 [1] in a study that proposed and performed a first validation of a nonlinear

reduced order modeling approach in which the response is, as in the modal analysis of linear structures, expressed as a linear combination of the (linear) modes. Then, these authors replaced the linear stiffness matrix by cubic polynomials of the generalized coordinates to model the geometric nonlinear effects. Moreover, the coefficients of these multidimensional polynomials were identified from standard outputs of a finite element code and the underlying finite element model. Then, the reduced order model could be constructed non-intrusively thereby allowing to use it with Nastran, Abaqus, and similar software and thereby achieving a complementarity with these standard analysis and design tools. Owing to its significantly reduced number of independent variables the response of the reduced order model could be computed much faster than the one of the original, potentially large sized, finite element model.

Since 2001, significant efforts have been dedicated by a limited number of researchers to improving the above reduced order modeling strategy in the following directions (see [2] for a slightly dated review):

(i) extension of the basis,

(ii) alternative identification methods of the coefficients of the cubic polynomials,

(iii) validations to more complex structures and with various physical features,

(iv) methodology extensions.

A short period after the original paper, it was recognized [3,4] that the basis of low frequency modes of the linear structure would not represent well the response of the structure, most notably it would not be able to capture the membrane stretching. This stretching is, for thin walled structures, a primarily “in plane” deformation while the linear

modes are primarily “transverse”. Noting that the membrane deformations are small and typically high frequency, it was suggested [3], that they be statically condensed (Implicitly Condensed or IC) in the much larger transverse motions to obtain the response of the structure. However, in a post processing effort, the membrane motions are recovered (Implicit Condensation with Expansion or ICE) to allow accurate predictions of the entire displacement field as well as stresses.

A different strategy was proposed in [4,5] that expands the basis to include not only low frequency linear modes of the structures but also a series of enrichments that capture the membrane deformations that are induced by large motions of the linear modes of the basis. These enrichments were referred to as “dual modes” and were shown to be determinable from standard outputs of finite element codes so that the non-intrusiveness was preserved.

Finally, efforts were also dedicated [6-10] to use higher frequency/in-plane linear modes of the structure. This framework guarantees the completeness of the basis, a very important property, and yielded good results on “simple” structures, e.g., [6,7]. Unfortunately, it was shown to be very difficult to implement efficiently on complex models, see [10], more so than the dual mode-based approach, see [11] for comparison.

The identification of the coefficients of the cubic polynomials has also received significant attention in part due to the modeling induced by the cubic restoring force. As shown in [2,3,12], the cubic nonlinearity is exact under some assumptions, e.g., Kirchhoff-St Venant material, von Karman strains, but is otherwise an approximation of the structural

behavior predicted by most commercial finite elements, see discussions in [13,14] regarding Nastran.

Two different viewpoints have been adopted for the identification of the coefficients. The first one has been (as in the original paper of [1]) to apply sets of forces to the finite element modeled structure and compute the corresponding responses. Then, project these forces and the finite element responses on the basis and impose the satisfaction of the reduced order model governing equations to obtain conditions to be satisfied by the coefficients, e.g., see [2]. Note that this effort can be done with static forces only since the nonlinear terms in the model relate only to deformations, not their rate.

The second perspective has been the reverse of the above one, i.e., impose displacements that are consistent with the basis and determine from the finite element model the forces which are required to achieve them. Then, as above, the forces are projected on the basis and the satisfaction of the reduced order model governing equations is imposed to obtain the necessary conditions for the coefficients. This strategy, developed by [15], is particularly convenient because an appropriate (and simple) selection of the imposed displacement fields leads to an identification of the coefficients by very small groups, 3 at most, and thus to a lack of conditioning issues that may be encountered in the other approach. This scheme is however not applicable (with the exception of flat structures, see [16]) to reduced order models based solely on linear modes (i.e., with implicit condensation).

Since the number of coefficients of the cubic polynomials grows rapidly, as $M^4/6$ with the number M of modes in the basis, a modification of the imposed displacement

approach has been proposed [11] in which the tangent stiffness matrix of the finite element model is extracted for each imposed deformed shape. Projecting this matrix on the basis and matching it to the reduced order model tangent stiffness matrix then provides M (M +1)/2 equations for every deformed shape as opposed to M modal forces. This approach is then much more efficient to identify the coefficients, requiring only of the order of $M^2/2$ deformed shapes and finite element computations vs. $M^3/6$ in the original approach.

The imposed displacement-based identification approaches require the user selection of the magnitude of these displacements their shapes being part of the algorithm. Often, the identified values of the coefficients are nearly independent of this magnitude, but a definite sensitivity has been observed for some structures. In such cases, the multiple level approach of [17] should be used; it seeks the range of magnitudes of the displacements in which the coefficients are most constant, a sign of good identification. The identification of the coefficients from experimental data has also been investigated, see [18].

The validation of the reduced order modeling approaches to a broad array of different structural model is a fundamental component of the formulation and development of these methods. Indeed, at the contrary of linear structures, nonlinear ones may exhibit fundamentally different behaviors and thus one purpose of the validations is to assess whether the reduced order modeling approach is valid broadly or only limited to a class of structures with specific response properties. Another purpose of the validations is to assess the impact of differences in the structural modeling, cubic for the reduced order model but likely something else (usually unclear because of proprietary concerns) for the finite element model, especially when the deformations become large and/or when the

nonlinearity is very strong. Since its first paper [4], the ASU group has constructed nonlinear reduced order model for 35 different structures ranging from straight beams to complex multibay [11,19] and orthogrid panels with up to 200,000 degrees of freedom finite element models [20-22], see [13,16,23-27] for a sample of these including cantilevered, free, and spring supported structures as well as some exhibiting a notch or a crack. The number of modes in the reduced order models which have been developed in these investigations have ranged from 2 to 85 and very good to excellent predictions, as compared to their full finite element counterparts, have been obtained in about 32 of these 35 cases.

Extensions of the reduced order methodology have focused primarily on the inclusion of heating effects with the temperature itself represented in a modal expansion format, see [21,30-33] to account for the complex temperature distributions that can result from aerodynamic heating in hypersonic flight. The extension of the methodology to account for uncertainties in the structure has also been successfully pursued [12, 14, 34-35]. Efforts have also been dedicated to the analysis of structures composed of substructures, e.g., by component mode synthesis [36,37] or the recently defined component-centric approach [38]. Finally, the coupling with the acoustic pressure field has been investigated in [39-40] and the consideration of piezoelectric effects addressed in [41] by relying on the thermal analogy.

Regardless of the structure to be modeled, there are two key issues in constructing a non-intrusive reduced order model: obtaining an a priori basis that represents well the

response of the structure and accurately identifying the nonlinear stiffness coefficients. The severity of these issues is increased when considering structures with strong nonlinearity.

Consider first the basis which has been determined by first selecting a set of linear modes of the structure, then determining "dual modes" which capture the effects of the geometric nonlinearity when the response is otherwise dominated by either one or a pair of the linear modes. Among the strongly nonlinear behaviors analyzed in this dissertation are those induced by a bifurcation. In such cases, the basis that is needed after the bifurcation may be quite different from the one needed before it occurs – even in terms of linear modes as will be demonstrated in a symmetry breaking example. While the linear modes of the structure are known to form a basis, no such result exists for the dual modes. They have been successfully used in a large number (over 30) of structures with definite nonlinearity but not behavior changes. It is thus unclear that they would still be appropriate, in the current format or not, for strongly nonlinear situations such as bifurcations.

In fact, predicting well the occurrence of a bifurcation will require not only that the corresponding deflection be well captured by the basis but also that the coefficients of the nonlinear reduced order model be accurately estimated. Past experiences have demonstrated that not all these coefficients can be considered reliably estimated owing to differences in nonlinear formulation between Nastran and the reduced order modeling. Those that dominate the response when (i) one or two low frequency linear modes are larger than the others and (ii) the dual mode generalized coordinates are much smaller than those of the linear modes, are typically well estimated but the others are not/may not be. When very large deflections occur along multiple linear and dual modes, as is the case with

the post snap-through behavior of a clamped-clamped curved beam, most coefficients have a significant effect and thus must reliably be identified. If they are not, the prediction could be very poor or simply nonexistent because the reduced order model governing equations are not stable.

The above challenges will be discussed in further details in the next few chapters and remedies will be proposed and successfully validated.

CHAPTER 2 OBJECTIVES

2.1 Status of Unsuccessful/Partially Successful NLROMs

As stated in the previous chapter, the ASU group successfully developed nonlinear structural reduced order models (ROM) for 32 of the 35 structures that have been considered over the years. Moreover, good predictive capabilities were obtained for 2 of the 32 structures but only when using an unorthodox basis (for 1 structure) or when excluding part of the loading domain (for the other structure).

Not surprisingly, these structures that have not been fully satisfactorily modeled are those which exhibit the strongest nonlinearity, most notably snap-through or buckling. These structures, their behavior, and the NLROM status are described below:

1) The clamped-clamped curved beam introduced in [7] and considered with snap-throughs in [42]. The desired analysis extended to the occurrence of snap-throughs and included the effects of a temperature field as well. Good predictions of the response without and with limited temperature were obtained but mostly using a basis formed by the linear modes of the straight beam (the unorthodox basis referred above) and by zeroing out, without strong argument, a series of stiffness coefficients. The most significant challenge encountered when building various NLROMs of this structure was instability – the NLROM marching would most often become unstable at the snap-through load.
2) The shallow cylindrical shell introduced by Drs J.J. Hollkamp and R. Gordon in [32]. In unpublished efforts, the ASU group encountered difficulties in obtaining

a basis, dual modes in particular, providing a good modeling of the response over the entire range of response levels including the mode switching point.

3) The Culler-McNamara panel defined in [43] and considered by NLROMs without and with temperatures in [27,30,31]. A structural NLROM was obtained that provides a very good modeling of the structural behavior in the response range of the problem. However, just outside that range, most notably when subjected to an upward loading, the panel exhibits a local buckling that involves strongly the stiffener, and which was never successfully captured by the published NLROM. More specifically, it was found that (i) the NLROM basis developed a priori (without the knowledge of the local buckling) did not represent well the buckled shape and (ii) the NLROM became unstable in the neighborhood of the buckling point.
4) The two joined wings discussed in [44]. The NLROM obtained for these models does not account correctly for the buckling, nor any post-buckling behavior. Besides the particular odd behavior of these wings, it has been noted that the cubic relationship between generalized coordinates and restoring force central to the NLROM is not consistent with the Nastran data even for the fundamental mode.
5) The full cylindrical shell analyzed in [32,33] subjected to tension and shear. The NLROM model could not capture the transition of the deformations through a series of different wrinkling patterns at nearly constant load, not the ensuing short post-buckling behavior.

In view of the above challenges, the focus of this thesis is first on understanding the difficulties in constructing reduced order models for structures exhibiting a strong nonlinearity and second on building reliable nonlinear reduced order models by modifying/extending current NLROM methodology. Of particular interest here are the first three structures in the above list only as the difficulties with the joined wings appear related to the core assumption of the NLROMs and thus should be the focus of a dedicated extension of the methodology. The full cylindrical shell of [32,33] may also suffer from the same issue or may simply be an extremely complex problem. Either way, its consideration should be revisited but only after fully successful NLROMs of the first structures are developed in a systematic manner.

2.2 Specific Objectives of the Present Investigation

Reviewing the above status of the NLROM efforts previously focused on the structures (1)-(3) it appears that the challenges can be regrouped as:

(i) difficulty in obtaining a basis that represents well the deformations of the structure, and/or

(ii) identifying a NLROM that is numerically stable in the range of deformations considered.

Understanding these issues as they relate to the structures (1)-(3) and possibly others and resolving them in a generic (not ad hoc) manner are the specific objectives.

In regard to the basis selection, the perspective of the present work remains that it be constructed from a limited information on the dynamics of the structure, i.e., primarily

linear modes and their associated duals as well as a limited set of static deformations resulting from “standard” loads (e.g., uniform pressure). Basic physical understanding of the structural behavior may also be expected, e.g., the potential for a clamped-clamped curved beam to experience snap through.

However, the existence of a local buckling under a particular loading condition should not be assumed as prior information because a comprehensive analysis of the structural behavior through the potential loading space is not a desirable or feasible option. Such an effort would dramatically undermine the computational benefits of the reduced order models, especially in the context of multi-physics problems such as the aero-structural-thermal coupled behavior of the Culler-McNamara panel, see for example [27,30,31,43] where it may not even be feasible.

Under the above restrictions, it may not be possible to construct a priori a basis that will always capture well the response. The potential for an inaccurate representation of the response is especially high in critical conditions, e.g., occurrence of buckling, and this investigation will focus as well on detecting such conditions and failures of the NLROM. This detection would be the first step in adapting the NLROM to the unexpected loading conditions, possibly along the lines of the Reduced ROMs (RROMs) developed in a different investigation [45].

2.3 Validation Structures for the Present Investigation

The clamped-clamped curved beam, the shallow cylindrical shell, and the Culler-McNamara panel are briefly described in the ensuing sections and their properties and behavior summarized.

2.3.1 Curved Beam

The geometry of the beam of [7,42] is showed in Figure 1.

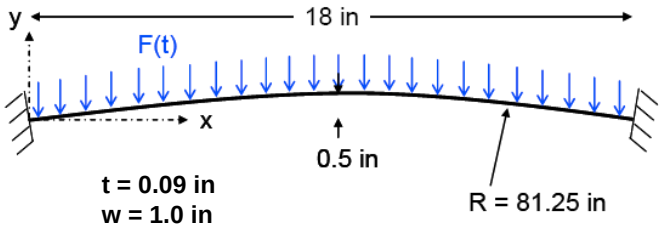

Figure 1. Curved Beam Geometry [7,42].

The beam was clamped on both ends, had an elastic modulus of 10.6×10^{6} psi, shear modulus of 4.0×10^{6} psi, and density of 2.588×10^{-4} lbf-sec^2/in^4. A finite element model with 144 CBEAM elements was developed in Nastran.

Consider first the behavior of the beam under static loads, more specifically a downward uniform pressure is assumed applied on the beam. The displacement is small if the pressure is small and the relation between pressure and displacement is very close to linear for the curved beam under small pressure. When increasing the value of pressure, the relation become more and more nonlinear. In fact, once the value exceeds a threshold value, the displacement will increase suddenly and sharply, and the beam has snapped-through, see Figure 2. When the magnitude of the pressure is reduced, from high to low,

the beam also experiences a snap-through (referred to here as snap-back) when the pressure is decreased below a threshold value, which is not the same one as in the loading process. Accordingly, there exists two stable static configurations of the beam in a particular range of pressures. These various behaviors lead to a load-deformation curve that is drastically nonlinear.

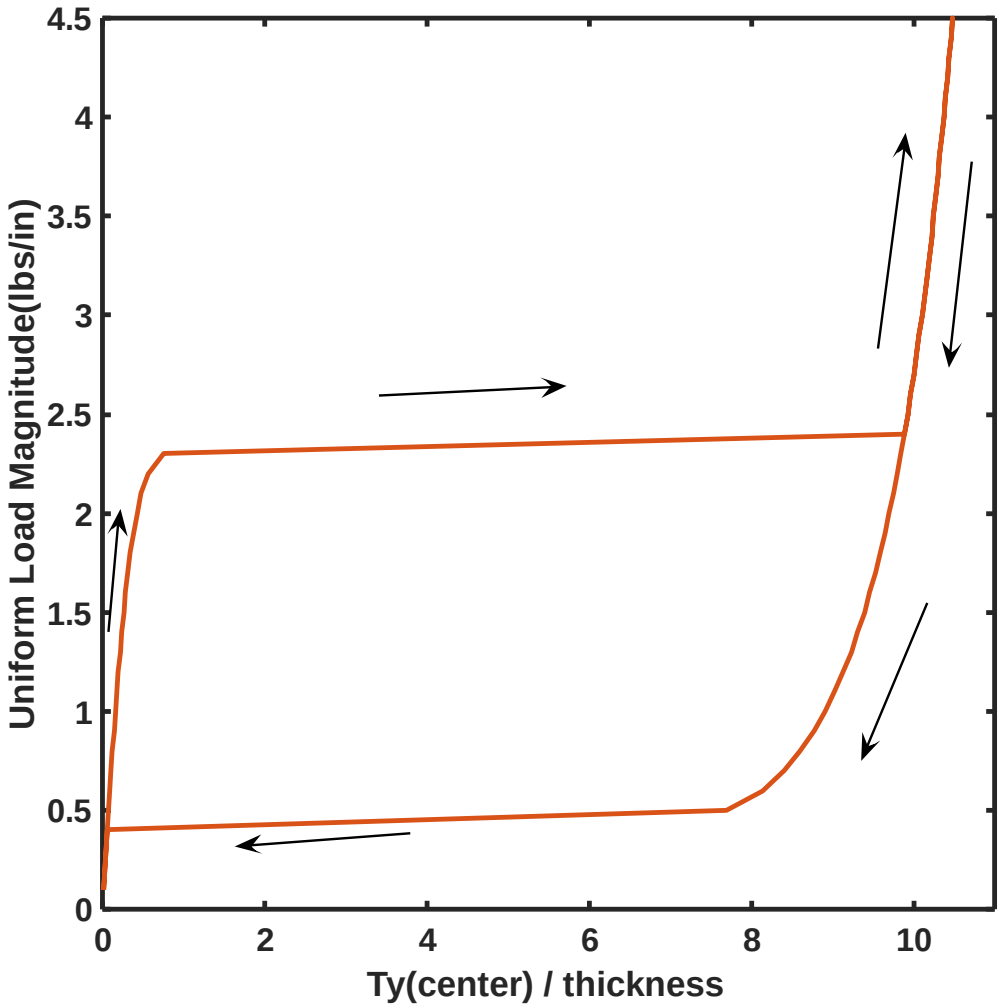

Figure 2. Vertical (Transverse) Displacement of the Beam Center as a Function of the Applied Uniform Pressure (Positive Downward). The Arrows Indicate the Loading Direction.

For dynamic cases, depending on the magnitude and frequency of the excitation, the occurrence of snap-through events varies from very rare, to frequent, to continuous as shown in Figure 3.

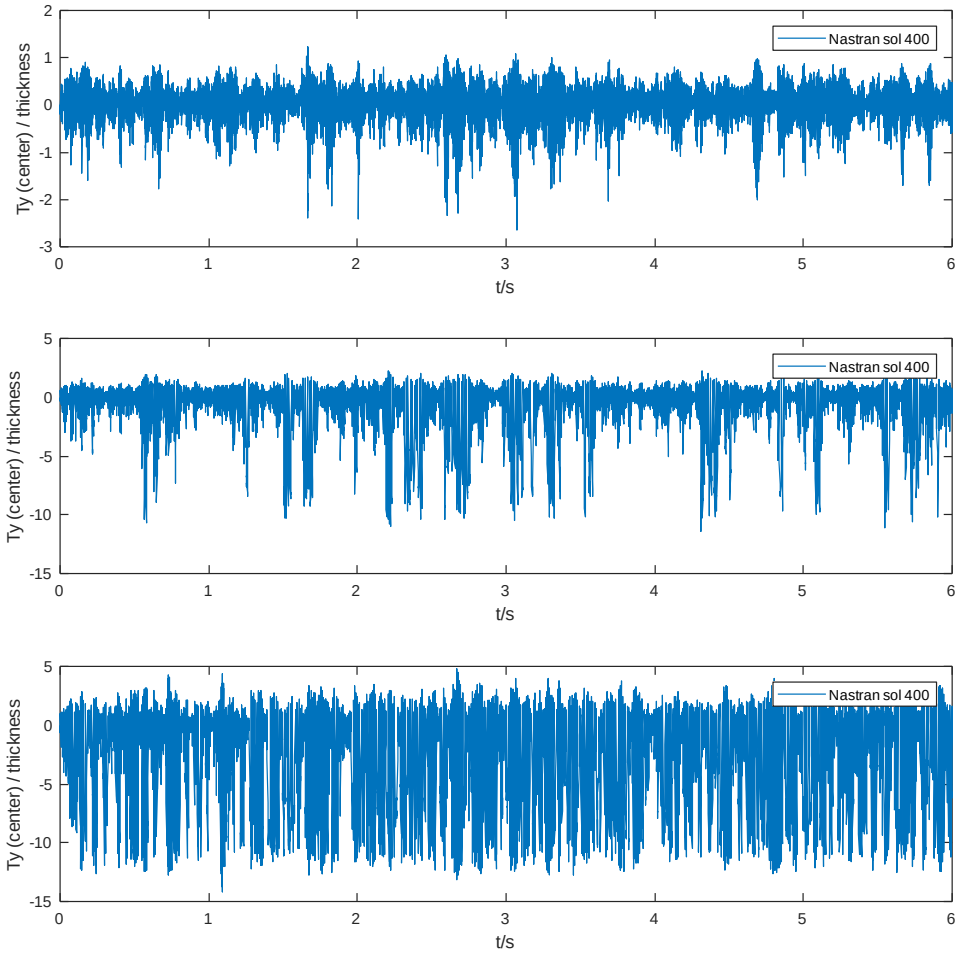

Figure 3. Typical Time Histories of the Transverse Displacement of the Center of the Curved Beam under Different Levels Excitations Showing No Snap-Through (Top), Occasional Snap-Throughs (Middle), and Frequent Snap-Throughs (Bottom).

2.3.2 Shallow Cylindrical Panel

The second validation structure is the shallow cylindrical shell introduced in [32] and which is shown in

. The panel is clamped on all the edges, has dimensions of 9.75 in by 15.75 in (projected length in the curved direction) by 0.048 in thick and a constant radius of curvature of 100 in in the x-y plane. The material properties are as follows: Young's modulus of 2.85×10^{6} psi, its Poisson's ratio is 0.3 and the density equals 7.84×10^{-4} lbf-sec^2/in^4. A finite element model with 39×63 shell (CQUAD4) elements was developed in Nastran and the panel is clamped on all 4 edges.

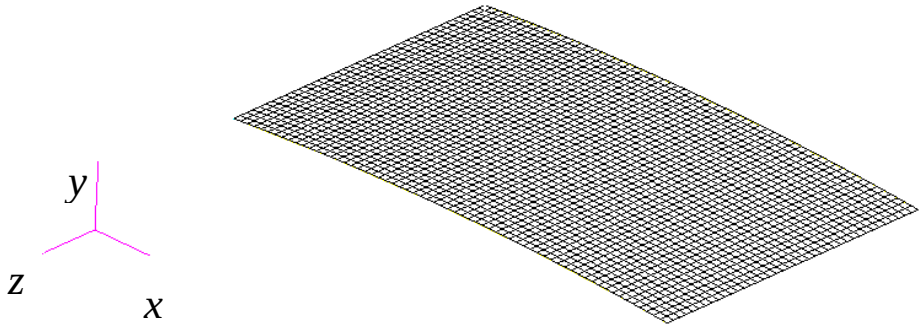

Figure 4. Finite Element Model of the Shallow Cylindrical Shell [32].

For this curved panel, one of the strongly nonlinear behaviors is mode switching. Specifically, under a small downward uniform pressure, the deformation is single-welled as show in Figure 5(a) for which the only maximum displacement occurs at the center of the panel. The displacement decreases from the center to the sides. However, for large enough pressures, the deformation becomes double-welled as showed in Figure 5(b) and exhibits two peaks.

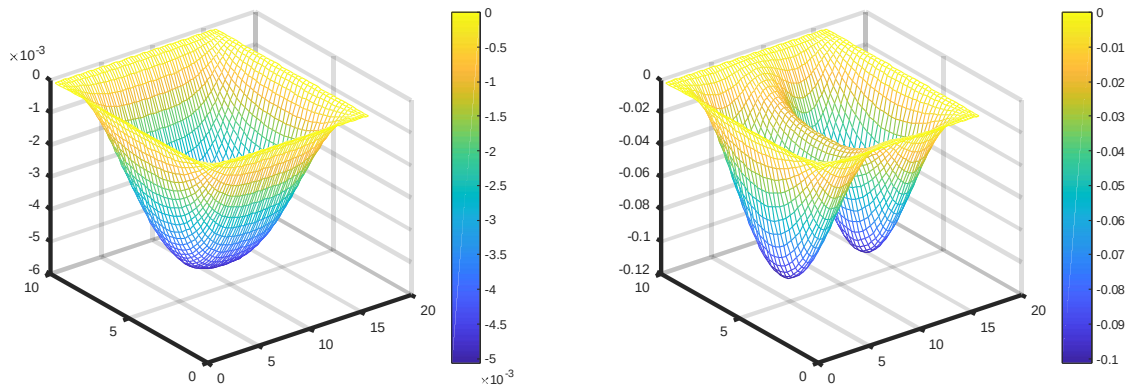

a) b)

Figure 5. Deflections of the Shallow Cylindrical Shell under Uniform Pressure. (a) Low Pressure, Single-welled Deformation, (b) High Pressure, Double-welled Deformation.

Another interesting feature of this panel is the occurrence under appropriately large dynamic pressure (uniform) of a symmetry breaking of the response. It is seen from Figure 4 that the panel has two axes of symmetry. Thus, when a uniform pressure is imposed (static or dynamic), there exists a deformation pattern that also exhibits that double symmetry. Statically, it appears that this is the only solution and similarly in the dynamic setting under "low" excitation. However, under large enough dynamic pressure, asymmetric deformations appear signaling that the symmetric solution has become physically unstable.

The occurrence of symmetry breaking is a good example of the information about the structural response that cannot be expected available as the basis is constructed. A basis composed of doubly symmetric transverse modes is thus expected to be selected and the asymmetric response will not be predicted correctly. The key need will thus be to predict the occurrence of the symmetry breaking from the NLROM to flag the potential for inadequacy of the basis.

2.3.3 Culler-McNamara or Representative hypersonic panel

The representative hypersonic panel first considered by Culler and McNamara [43] is shown in Figure 6. It is composed of a skin and two parallel stiffeners of dimensions shown in Figure 6(a) and thicknesses of 0.065 in and 0.0325 in for the skin and stiffener. The panel is made of a composite material (advanced carbon-carbon 4) with the following properties: Young's modulus$_{11}$ of 15×10^6 psi, Young modulus$_{22}$ of 15×10^6 psi, density of 0.065 lbm/in^3, shear modulus$_{12}$ equals 2.5×10^6 psi, and the Poisson's ratio$_{12}$ is 0.3. The Nastran finite element model is composed of 2400 identical 4-node plate (CQUAD4) elements, of sizes 0.25 in by 0.25 in, resulting in 2499 nodes. For ease of plotting, the panel will sometimes be shown as "flattened", i.e., with the two stiffeners rotated in the plane of the skin, as shown in Figure 6(b).

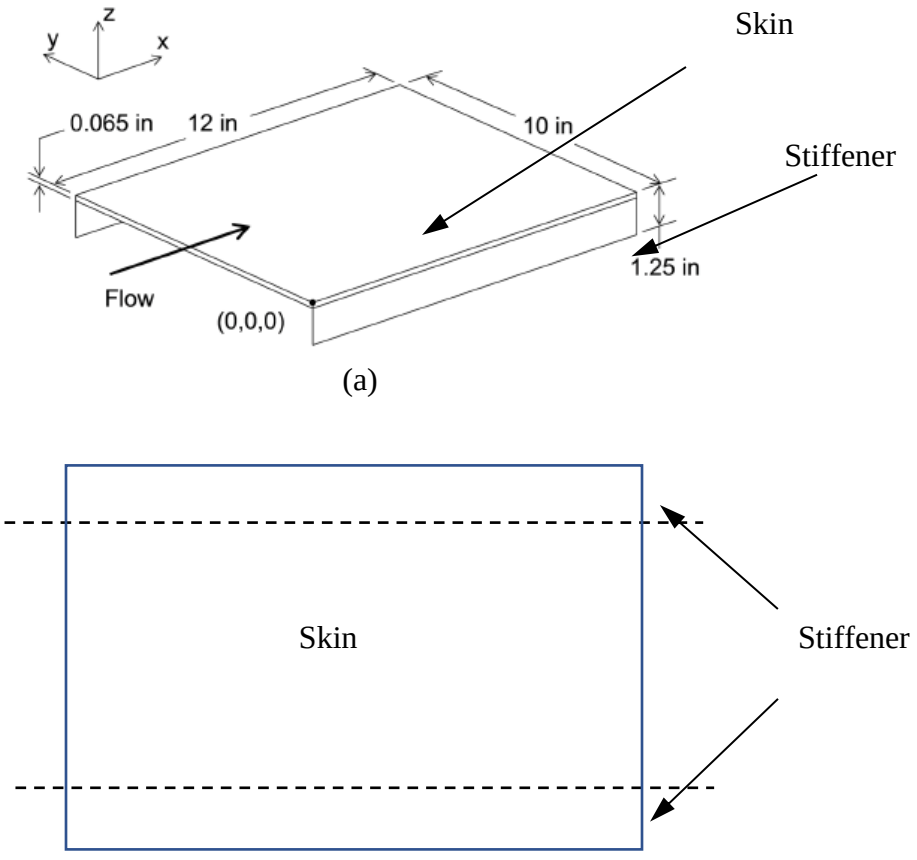

Figure 6. (a) The Representative Hypersonic Panel [43]. (b) Its "Flattened" Version.

The boundary conditions are:

(1) At the leading edge, x=0 and z=0, zero displacements are enforced for all degrees of freedom except for the y translations which are free.

(2) At the trailing edge, x=12 in and z=0, zero displacements are enforced for all degrees of freedom except x and y translations, which are free. Springs also act on the nodes of the trailing edge in the x direction with a spring constant of 2378 lbs/in.

(3) At the panel center, x=6 in, y=5 in, and z=0, zero displacements in y translations are imposed.

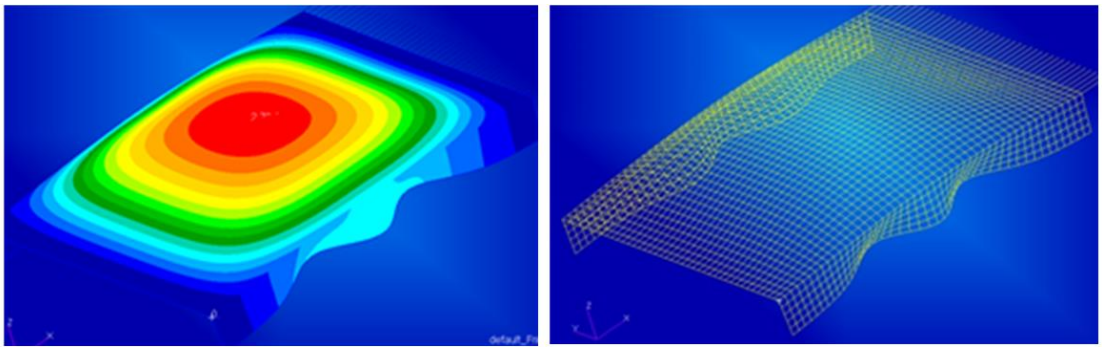

Figure 7. Local Bucking of the Representative Hypersonic Panel – Different Views.

In analyzing the response of this panel in [27], it was found that it exhibits a local buckling which, as shown in Figure 7, affects primarily the stiffeners and the skin near the fold line. This local bucking decreases sharply the eigenvalue of tangent stiffness matrix but not to zero like a global buckling or the snap-through of the curved beam.

CHAPTER 3 NLROM FORMULATION REVIEW

For completeness, the formulation of the nonlinear reduced order modeling is reviewed below detailing in order the 3 key aspects of governing equations derivation, dual mode construction and non-intrusive identification of the stiffness coefficients.

3.1 NLROM Governing Equations

The nonlinear reduced order modeling method utilized here can be viewed as the extension to the nonlinear geometric situation of the modal models developed in linear structures. The derivation of the equations of motion is taken from [2]. In NLROM, the displacement field $\mathbf{u}$ expressed as

$$\mathbf{u}(t) = \sum_{n=1}^{M} q_n(t)\boldsymbol{\psi}^{(n)} \qquad (1)$$

where $\mathbf{u}$ is the displacement of all degrees of freedom of all nodes, $\boldsymbol{\psi}^{(n)}$ are the basis functions, and q_n are the corresponding generalized coordinates. The basis functions $\boldsymbol{\psi}^{(n)}$ result from the mode selection process discuss in the next section and are constant vectors. A key property of these functions is that they must satisfy the geometric boundary conditions. In a dynamic analysis, the displacements vary with time, so $\mathbf{u}$ is a function of time and so are the generalized coordinates.

Since the basis functions are intended to be constant and must satisfy the geometric boundary conditions, these conditions cannot be time dependent. Thus, the equations of motion of the structure must be expressed in the undeformed configuration. From finite

deformation elasticity theory, the momentum balance of an infinitesimal element is (summation over repeated indices is assumed in all equations unless otherwise stated)

$$\frac{\partial}{\partial X_k}\left(P_{ik}\right)+\rho_0 b_i^0=\rho_0 \ddot{u}_i \text{ for } \mathbf{X}\in\Omega_0 \qquad (2)$$

where $\mathbf{P}$ is the first Piola-Kirchhoff stress tensor, $\mathbf{X}$ is the coordinate of the undeformed configuration, ρ_0 is the density in the reference configuration, and $\mathbf{b}^0$ is the vector of body forces. The displacement vector is

$$\mathbf{u}=\mathbf{x}-\mathbf{X} \qquad (3)$$

where $\mathbf{x}$ is the coordinate of the current configuration. Moreover, the stress tensor $\mathbf{P}$ can be expressed as

$$P_{ik}=F_{ij}S_{jk} \qquad (4)$$

where $\mathbf{S}$ denotes the second Piola-Kirchhoff stress tensor and $\mathbf{F}$ is the deformation gradient tensor defined as:

$$F_{ij}=\frac{\partial x_i}{\partial X_j}=\delta_{ij}+\frac{\partial u_i}{\partial X_j} \qquad (5)$$

where δ_{ij} denotes the Kronecker delta.

Consider now the boundary conditions, Ω_0 is the domain occupied by the structure ($\mathbf{x}$) and $\partial\Omega_0$ is its boundary which may be composed of two parts. One is $\partial\Omega_0^t$ on which

the traction $\mathbf{t}^0$ are prescribed. The other one is $\partial\Omega_0^u$ on which the displacement are specified (assumed zero here). The boundary conditions are thus

$$F_{ij}\, S_{jk}\, n_k^0 = t_i^0 \tag{6}$$

and

$$\mathbf{u} = \mathbf{0} \text{ for } \mathbf{X} \in \partial\Omega_0^u \tag{7}$$

To complete the formulation of the elasticity problem, it remains to specify material behavior. A St Venant-Kirchhoff model is assumed here in which the relation between the second Piola-Kirchhoff stress tensor $\mathbf{S}$ and the Green strain tensor $\mathbf{E}$ is linear. That is, defining

$$E_{ij} = \frac{1}{2}\left(F_{ki}\, F_{kj} - \delta_{ij}\right) \tag{8}$$

the constitutive relation is

$$S_{ij} = C_{ijkl}\, E_{kl} \tag{9}$$

where C_{ijkl} denotes the fourth order elasticity tensor.

To get the governing equation of finite dimensional reduced order models, a test function $\underline{v} = \underline{v}(\underline{X})$ is used to form the weak form where $\underline{v}$ is sufficiently differentiable and $\underline{v} = \underline{0}$ on $\partial\Omega_0^u$. Multiplying Eq. (2) by this function and using Eq. (4), one has

$$v_i \frac{\partial}{\partial X_k}\left(F_{ij}\, S_{jk}\right) + v_i \rho_0\, b_i^0 = v_i \rho_0\, \ddot{u}_i \qquad (10)$$

where

$$v_i \frac{\partial}{\partial X_k}\left(F_{ij}\, S_{jk}\right) = \frac{\partial}{\partial X_k}\left(v_i F_{ij}\, S_{jk}\right) - \frac{\partial v_i}{\partial X_k}(F_{ij}\, S_{jk}) \qquad (11)$$

Inserting this relation in Eq. (10) and integrating over the entire domain Ω_0 yields

$$\int_{\Omega_0} \rho_0 v_i\, \ddot{u}_i \mathrm{d}\underline{\mathrm{X}} + \int_{\Omega_0} \frac{\partial v_i}{\partial X_k}(F_{ij}\, S_{jk})\, \mathrm{d}\underline{\mathrm{X}} = \int_{\Omega_0} \rho_0 v_i\, b_i^0 \mathrm{d}\underline{\mathrm{X}} + \int_{\Omega_0} \frac{\partial}{\partial X_k}\left(v_i F_{ij}\, S_{jk}\right) \mathrm{d}\underline{\mathrm{X}} \qquad (12)$$

Applying Gauss' theorem and imposing the boundary condition Eq. (6) yields

$$\int_{\Omega_0} \rho_0 v_i\, \ddot{u}_i \mathrm{d}\underline{\mathrm{X}} + \int_{\Omega_0} \frac{\partial v_i}{\partial X_k}(F_{ij}\, S_{jk})\, \mathrm{d}\underline{\mathrm{X}} = \int_{\Omega_0} \rho_0 v_i\, b_i^0 \mathrm{d}\underline{\mathrm{X}} + \int_{\partial\Omega_0^t} v_i t_i^0 \mathrm{d}s\,. \qquad (13)$$

In the context of the above continuum, the reduced order model Eq. (1) is

$$u_i(\mathbf{X}, t) = \sum_{\mathrm{n}=1}^{\mathrm{M}} q_n(t) \Psi_i^{(n)}(\mathbf{X})$$

in which the basis functions $\boldsymbol{\Psi}^{(n)}(\mathbf{X})$ satisfy the boundary conditions and are assumed to be sufficiently differentiable (by construction). Then, they are appropriate test functions. Selecting $v_i = \Psi_i^{(m)}$ in Eq. (13), in which the displacement field u_i is expressed as in Eq. (1) yields after some algebraic manipulations the governing equations for the nonlinear reduced order models as

$$M_{ij}\ddot{q}_j + K_{ij}^{(1)} q_j + K_{ijl}^{(2)} q_j q_l + K_{ijlp}^{(3)} q_j q_l q_p = F_i \qquad (14)$$

where

$$M_{mn} = \int_{\Omega_0} \rho_0 \Psi_i^{(m)} \Psi_i^{(n)} \, \mathrm{d}\underline{X} \qquad (15)$$

$$K_{mn}^{(1)} = \int_{\Omega_0} \frac{\partial \Psi_i^{(m)}}{\partial X_k} C_{iklp} \frac{\partial \Psi_l^{(n)}}{\partial X_p} \, d\underline{X} \qquad (16)$$

$$K_{mnp}^{(2)} = \frac{1}{2}\left[\hat{K}_{mnp}^{(2)} + \hat{K}_{pmn}^{(2)} + \hat{K}_{npm}^{(2)} \right] \qquad (17)$$

$$\hat{K}_{mnp}^{(2)} = \int_{\Omega_0} \frac{\partial \Psi_i^{(m)}}{\partial X_j} C_{ijkl} \frac{\partial \Psi_r^{(n)}}{\partial X_k} \frac{\partial \Psi_r^{(p)}}{\partial X_l} \, d\underline{X} \qquad (18)$$

$$\hat{K}_{msnp}^{(3)} = \frac{1}{2} \int_{\Omega_0} \frac{\partial \Psi_i^{(m)}}{\partial X_j} \frac{\partial \Psi_i^{(s)}}{\partial X_k} C_{jklw} \frac{\partial \Psi_r^{(n)}}{\partial X_k} \frac{\partial \Psi_r^{(p)}}{\partial X_l} \, d\underline{X} \qquad (19)$$

$$F_m = \int_{\Omega_0} \rho_0 \Psi_i^{(m)} b_i^0 \, \mathrm{d}\underline{X} + \int_{\partial\Omega_0^t} \Psi_i^{(m)} t_i^0 \, \mathrm{d}s \qquad (20)$$

Equation (14) is the governing equation appropriate for structures with no energy dissipation which is usually not the situation in real life. To render the NLROM of practical significance, damping is added to model the dissipation mechanisms in real structures. In this investigation, a linear damping model will be assumed to focus on the nonlinear geometric effects resulting from the restoring force, but it is recognized that a nonlinear damping, such as the one utilized in [45], may be more appropriate, especially to model

effects where the damping plays a dominant role. With this assumption, Eq. (14) is modified to read

$$M_{ij}\ddot{q}_j + D_{ij}\dot{q}_j + K_{ij}^{(1)} q_j + K_{ijl}^{(2)} q_j q_l + K_{ijlp}^{(3)} q_j q_l q_p = F_i \qquad (21)$$

A Rayleigh damping will be used consistently in the validation examples because it provides some flexibility on the damping modeling but also because it is readily implementable in Nastran to allow exact one to one comparison. Then,

$$D_{ij} = \alpha M_{ij} + \beta K_{ij}^{(1)} \qquad (22)$$

where α and β are constants of proportionality. They are specified as in the linear case, e.g. to have a particular modal damping ratio of certain modes as discussed in the validations.

As stated in the introduction, heated structures have also been considered in the literature and will be addressed here as well. In such cases, Eq. (21) must be extended to include the effects of thermal expansion and possibly the changes of material properties with temperature, see [21,28-31]. The temperature field could be represented by a series of temperature basis functions

$$T(\mathbf{X},t) = \sum_{n=1}^{\mu} \tau_n(t) T^{(n)}(\mathbf{X}) \qquad (23)$$

The constitutive relation become

$$S_{ij} = C_{ijkl}\left[E_{kl} - \alpha_{kl}(T - T_0)\right] \qquad (24)$$

where α is the thermal expansion tensor. When the thermal expansion must be accounted for, it was shown [28] that Eq. (21) should be replaced by

$$M_{ij}\ddot{q}_j + D_{ij}\dot{q}_j + K_{ij}^{(1)} q_j - K_{ijl}^{(th)} q_j \tau_l + K_{ijl}^{(2)} q_j q_l + K_{ijlp}^{(3)} q_j q_l q_p = F_i + F_{il}^{(th)} \tau_l \qquad (25)$$

where α and C are temperature independent. In the above equation, $K_{ijl}^{(th)}$ is a temperature induced stiffness coefficient relating to the likely constrained thermal expansion and $F_{il}^{(th)}\tau_l$ is similarly a thermal modal force both expressed as

$$K_{mnp}^{(th)} = \int_{\Omega_0} \frac{\partial \Psi_i^{(m)}}{\partial X_k} \frac{\partial \Psi_i^{(n)}}{\partial X_j} C_{jklr} \alpha_{lr} T^{(P)} d\underline{X} \qquad (26)$$

$$F_{mn}^{(th)} = \int_{\Omega_0} \frac{\partial \Psi_i^{(m)}}{\partial X_k} C_{iklr} \alpha_{lr} T^{(n)} d\underline{X} \qquad (27)$$

3.2 Basis Selection

Having established the form of the governing equations of the NLROM, the second critical task is the selection of the basis. Clearly, obtaining a perfect representation of the displacement would require that the number of basis functions (also referred to as modes and assumed linearly independent) be equal to the total number of degrees of freedom of the finite element model, or infinity for real structures which have infinite degrees of freedom. Accordingly, one would not expect any (significant) reduction in the computational effort since the benefits of reduced order models are associated with the

decrease in the number of degrees of freedom not with a transformation of the equations. However, if the basis is not complete, there would inevitably be truncation (or representation) error. This discussion leads to two contradictory requirements for the basis: (i) only have a small number of basis functions and (ii) induce a small truncation error.

The objective of basis selection is then to form a group of bases functions that will achieve both (i) and (ii) at best. While a formal optimization problem to find the basis might be formulated by relying on the above, a different approach is followed here seeking to achieve a given truncation error, 1% is usually used, with an "appropriately low" number of modes. When possible and mathematically straightforward, the number of modes will be reduced consistently with this error but efforts to "marginally" reduce the size of the basis are not undertaken because they would incur a computational cost or user time which would negatively impact the benefits of using NLROMs (see also discussion on Reduced ROMs in [45]). What is key for the present investigation is the process by which to construct a good basis, inducing a representation error of 1% or less and having a relatively small number of modes.

In linear dynamic problems, the selection of the basis has been well resolved and consists of the linear modes (or normal modes) of the structure which are the eigenvectors of the eigenproblem,

$$\hat{\mathbf{K}}^{(1)}\hat{\boldsymbol{\varphi}}_l = \omega_l^2\, \hat{\mathbf{M}}\hat{\boldsymbol{\varphi}}_l \qquad (28)$$

where ω_l are the natural frequencies and $\hat{\boldsymbol{\varphi}}$ are the (linear or normal) modes from which the basis is selected. Note that the number of modes is equal to the number of degrees of

freedom of the structure so that the conflicting issues of truncation and reduction are also present here. The selection of the modes to include on the basis depends on the excitation and more specifically on its band of energy. Assuming a low damping, the modes which will be most present in the response are those who are (i) strongly excited by the loading and (ii) low frequency. Given the excitation or the type of excitations, a formal selection process of the modes can then be conducted. Note that the energy of the excitation is limited to a particular band, the response of the structure is also limited to that band, i.e., there is no transfer of energy to lower or higher frequencies possible – at the contrary of nonlinear systems.

The basis functions to be used in nonlinear geometric problems should definitely include all of the modes that would be chosen if the problem was linear, but this is in general not sufficient. The structures of particular interest here are thin walled ones and the excitation may be expected to be primarily “transverse”. Then, the deflections are also primarily transverse, even in the nonlinear case and these components can be well represented by the low frequency/first few linear modes of the structure which are also transverse dominant. In general, it is advisable to take more of these linear modes than would be used in the linear case because a transfer of energy from low frequency to higher frequency often happens and modes not excited in the linear problem are excited in the nonlinear one.

Even though the transverse deflections are the largest by far, it is not sufficient to only model them. When these deflections become large, in-plane deflections do appear associated with the “membrane stretching”. While small, these deflections are typically

associated with very stiff motions and thus carry significant potential energy. In fact, they can be viewed as resulting from an energy transfer from low frequency to high frequencies as mentioned above. They must thus be included in the basis in the form of enrichments which are selected here as the dual modes first introduced in [5], see also [2,11]. Their construction is briefly reviewed below.

Dual modes can be viewed as associated with the transverse displacements described by the linear basis, i.e., the transverse modes. The general procedure to obtain these dual modes is to subject the system to forces that would induce displacements along the transverse modes in the linear case and assess what additional deformations happen. Since these deformations are small, the response is globally along the transverse mode or modes chosen which implies that the applied forces could be selected as those that induce a response exactly in that mode in the linear case. Note further that the expectations of the dual modes to be very stiff (high frequency) implies that their response would be quasi-static even if the transverse motions are fully dynamic. Accordingly, it is sufficient for the dual mode construction to proceed statically.

On that basis, denoting by $\boldsymbol{\Psi}$, the transverse mode of which the dual need to be determined, the applied loading on the structure $\mathbf{F}^{(\mathbf{m})}$ should be of the form

$$\mathbf{F}^{(\mathbf{m})} = \alpha \mathbf{K}_{\mathbf{FE}}^{(\mathbf{1})} \boldsymbol{\Psi} \qquad (29)$$

where α is the amplification factor used for adjusting the magnitude of loading. This factor should be large enough that nonlinear geometric effects are indeed present and are of the same order of magnitude as those observed in the NLROM solution to the actual loading.

Practically, a series of loadings of the form of Eq. (29) are applied with both positive and negative values in a range that induces peak deflections of the structure from very small (linear) to a few thicknesses (nonlinear).

Once the nonlinear displacements resulting from the loading of Eq. (29) have been obtained, their components along the transverse modes are removed through a Gram-Schmidt orthogonalization. Next, a Proper Orthogonal Decomposition (POD) is carried out on the remainders of the displacements and a group of eigenvectors/eigenvalues are obtained.

To minimize the number of modes in the basis, not all eigenvectors are selected as dual modes. There are two criteria for dual selection. One is the representation of the remainders, especially in the in-plane direction, the other one is the strain energy. The strain energy of a particular mode V is here assumed to be that of the linear structure, i.e.,

$$V = \frac{1}{2}\boldsymbol{\Psi}^{\mathbf{T}}\mathbf{K}^{(1)}\boldsymbol{\Psi} \qquad (30)$$

Since the motivation for the dual modes is to capture the nonlinear in-plane response, those that induce large reductions in the representation error in the in-plane direction could be taken as candidates. Moreover, since in-plane motions are typically quite stiff, the corresponding strain energy should also be large, and this is a second criterion for the selection of an eigenvector as a dual mode.

The next question to address is for which modes the dual construction should be carried out. The contributions of the various transverse modes in the nonlinear response of

the structure are not equal. In fact, there is usually a very large difference among these transverse modes. These contributions could be evaluated by comparing the projections on these modes of some representative nonlinear displacements obtained to guide the basis selection. The ones that have contributions significantly greater than the other ones could be considered as 'dominant' modes and their duals should be constructed.

Note however that owing to the nonlinearity of the response, the dual constructed for the sum of two transverse mode is not equal to the sum of the duals obtained by considering each mode separately. Thus, the vector $\boldsymbol{\Psi}$ in Eq. (29) should also include linear combinations of these dominant modes, typically by two up to three (see discussion in [5]) to reflect correctly the in-plane deformations when more than one mode is present in the response. While the non-dominant modes may not be large enough to represent the response of the structure at any time, they can potentially modify the dominant modes and thus linear combinations involving a dominant mode and a non-dominant one is also typically considered.

At the end of the dual construction process, the basis is finally obtained as

$$\Psi = \left[\hat{\boldsymbol{\varphi}}_t, \hat{\boldsymbol{\varphi}}_d\right] \qquad (31)$$

where $\hat{\boldsymbol{\varphi}}_t$ are linear modes, $\hat{\boldsymbol{\varphi}}_d$ are dual modes.

3.3 Identification of the NLROM Parameters

The last critical step of the NLROM construction is the non-intrusive identification of all its parameters, i.e., their estimation using standard input-output of commercial finite element codes. Proceeding as in the linear case, one obtains directly

$$M_{ij} = \Psi_p^{(i)} \hat{M}_{pr} \Psi_r^{(j)} \quad (32)$$

$$K_{ij}^{(1)} = \Psi_p^{(i)} \hat{K}_{pr}^{(1)} \Psi_r^{(j)} \quad (33)$$

where $\hat{\mathbf{M}}$ and $\hat{\mathbf{K}}^{(1)}$ are the finite element mass and linear stiffness matrices which can be outputted by commercial finite element software, e.g., Nastran. Damping can then be obtained from Eq. (22). It then remains to identify the parameters $\mathbf{K}^{(2)}$ and $\mathbf{K}^{(3)}$ which will be obtained, as discussed in the introduction, using the imposed displacement approach.

Under static conditions and ignoring thermal effects, the governing equations, Eq. (25), can be written as,

$$K_{ij}^{(1)} q_j + K_{ijl}^{(2)} q_j q_l + K_{ijlp}^{(3)} q_j q_l q_p = F_i \quad (34)$$

where F_i are the modal forces. The strategy devised in [15] is to impose several sets of displacements (i.e., the q_j), then to determine the corresponding modal forces using the finite element code, finally to impose the satisfaction of Eq. (34) in which the displacements and modal forces have been inserted. This process leads to sets of linear equations for the unknown stiffness coefficients from which they can be determined. The

specific sets of displacements are chosen to form small systems of equations for the coefficients vs. one large one. Specifically, they are sets:

i) displacements proportional to a single mode

Impose $q_j = q$, $q_j = -q$ and $q_j = 0.5q$; all other generalized coordinates = 0. Repeat for all values of j.

ii) displacements proportional to a linear combination of 2 modes

Impose $q_j = q_l = q$, $q_j = q_l = -q$, and $q_j = -q_l = q$ all other generalized coordinates = 0. Repeat for all distinct values of j and l.

iii) displacements proportional to a linear combination of 3 modes

Impose $q_j = q_l = q_k = q$, all other generalized coordinates = 0. Repeat for all distinct values of j, l, and k.

For set (i), the displacements imposed on the finite element model is

$$\underline{u} = q_n \underline{\Phi}^{(n)}, \hat{\underline{u}} = \hat{q}_n \underline{\Phi}^{(n)}, \tilde{\underline{u}} = \tilde{q}_n \underline{\Phi}^{(n)} \qquad (35)$$

To each displacement corresponds one group of equations from eq. (34) so the total equations are,

$$\begin{aligned} K_{in}^{(1)} q_n + K_{inn}^{(2)} q_n^2 + K_{innn}^{(3)} q_n^3 &= F_i \\ K_{in}^{(1)} \hat{q}_n + K_{inn}^{(2)} \hat{q}_n^2 + K_{innn}^{(3)} \hat{q}_n^3 &= \hat{F}_i \\ K_{in}^{(1)} \tilde{q}_n + K_{inn}^{(2)} \tilde{q}_n^2 + K_{innn}^{(3)} \tilde{q}_n^3 &= \tilde{F}_i \end{aligned} \qquad (36)$$

where i= 1,2, 3, …, M, and there is no summation over repeated indices. Equation (35) provides the values of $K_{in}^{(1)}, K_{inn}^{(2)}$, and $K_{innn}^{(3)}$ for all i and all of them by repeating for every n = 1, ..., M.

For set (ii), the displacements imposed on the finite element model are

$$\underline{u} = q_n \underline{\Phi}^{(n)} + q_m \underline{\Phi}^{(m)} \qquad (37)$$

where $n \le m$ and no summation over n or m. The coefficients $K_{in}^{(1)}, K_{inn}^{(2)}, K_{innn}^{(3)}$ and $K_{im}^{(1)}, K_{imm}^{(2)}, K_{immm}^{(3)}$ which have been found in step (i) can be taken as known in the corresponding modal force equations. Then, all coefficients of the form $K_{inm}^{(2)}, K_{innm}^{(3)}, K_{inmm}^{(3)}$ can be identified.

For set (iii), the displacement imposed on the finite element model is

$$\underline{u} = q_n \underline{\Phi}^{(n)} + q_m \underline{\Phi}^{(m)} + q_r \underline{\Phi}^{(r)} \qquad (38)$$

and it leads to the remaining coefficients $K_{inmr}^{(3)}$ with m, n, and r all different.

For each imposed displacement, M modal forces are obtained and thus M equations of the form of Eq. (34). The number of imposed displacements to identify the order $M^4/6$ stiffness coefficients is thus of order $M^3/6$.

More recently [11], a modification of the above approach was proposed in which the tangent stiffness matrix of the finite element model (projected on the basis) is matched to the NLROM one. The tangent stiffness matrix is by definition

$$K_{iu}^{(T)} = \frac{\partial F_i}{\partial q_u} \qquad (39)$$

and thus, for the NLROM, it is

$$K_{iu}^{(T)} = K_{iu}^{(1)} + \left[K_{iju}^{(2)} + K_{iuj}^{(2)} \right] q_j + \left[K_{ijlu}^{(3)} + K_{ijul}^{(3)} + K_{iujl}^{(3)} \right] q_j q_l \qquad (40)$$

This matrix should be matched to the tangent stiffness matrix of the finite element model projected on the basis, i.e., to

$$\mathrm{K}^{(\mathrm{T})} = \Psi^{\mathrm{T}} \mathrm{K}_{\mathrm{FE}}^{(\mathrm{T})} \Psi \qquad (41)$$

Note in this approach that M (M +1)/2 equations are obtained for every deformed shape as opposed to M modal forces. It is then much more efficient than the previous one to identify the coefficients, requiring only of the order of $M^2/2$ deformed shapes and finite element computations vs. $M^3/6$ in the original approach.

CHAPTER 4 BASIS OPTIMIZATION

4.1 Optimization of the Transverse Basis $\hat{\varphi}_l$

A standard observation made in regards to modal expansion of the form of Eq. (1) is that replacing the basis function $\psi^{(n)}$ by linear combinations of themselves does not change the capability of the sum to represent any particular function. It may thus be concluded that there is no value in performing a rotation of the linear modes to form the first, transverse part of the basis.

This conclusion is correct for the transverse basis alone, but it must be remembered that these transverse modes are the source of the dual modes. So, a transformation of the transverse modes will give rise to new dual modes which are not simple rotations of the prior duals because the duals are derived from a nonlinear problem. Accordingly, it is meaningful to investigate the role of a rotation of the transverse mode on the appropriateness of the duals and, more globally of the corresponding basis, in representing the response.

In this regard, it has long been noted that the duals are particularly efficient when there is only one mode that dominates the response. In fact, in most of the successful NLROMs, there is a strongly dominant single mode – typically the lowest frequency mode excited. Accordingly, it is proposed here to induce a rotation of the linear modes to capture, at best with one mode, the response of the structure in some typical nonlinear responses computed in advance for that purpose.

Emphasizing one mode vs. multiple ones has also some potential stability benefit. Indeed, it has often been observed that the cubic coefficients $K_{iujl}^{(3)}$ with $u \neq j \neq l$ are more sensitive to the conditions of the identification than their counterparts where $u = j = l$. When the response is primarily split between two or more modes, many more cubic coefficients are strongly involved in the equations than when there is a single mode. So, a single dominant mode response is likely to provide an increase accuracy/stability by reducing the number of terms on which the identification may be inaccurate (this issue results from the nonlinear geometric model of the finite element being different from the one assumed from the NLROM, see [13,14]).

Consider the curved beam of section 2.3.1 and shown in Figure 8 are its first 6 linear modes. Shown in Figure 9 are the displacement of the beam under downward pressures, one below the snap-through level and the other above it.

At first glance, the curves of Figure 8 and Figure 9 are quite different. There are a few nodal points on linear modes but not on the displacements. Using that linear basis to represent well the deformations is possible but this approximation will heavily involve several of the linear modes.

Based on the above discussion, a process was established to create a rotation of the basis (the 6 linear modes) so that one of them provides the best possible approximation of the observed (reference) static deformations. This process is as follows.

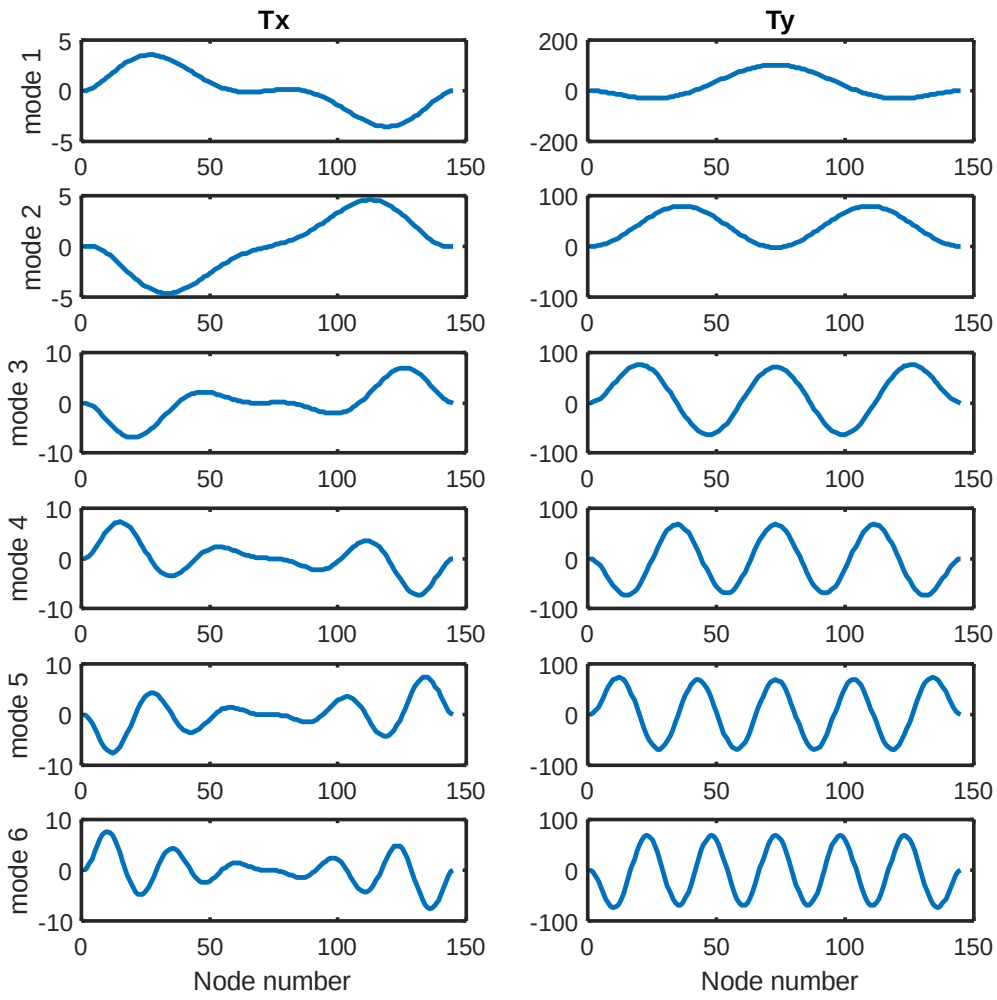

Figure 8. Mode Shape of the First 6 Linear Modes. In-plane (T_x, Left Column) and Transverse (T_y, Right Column) Deflections.

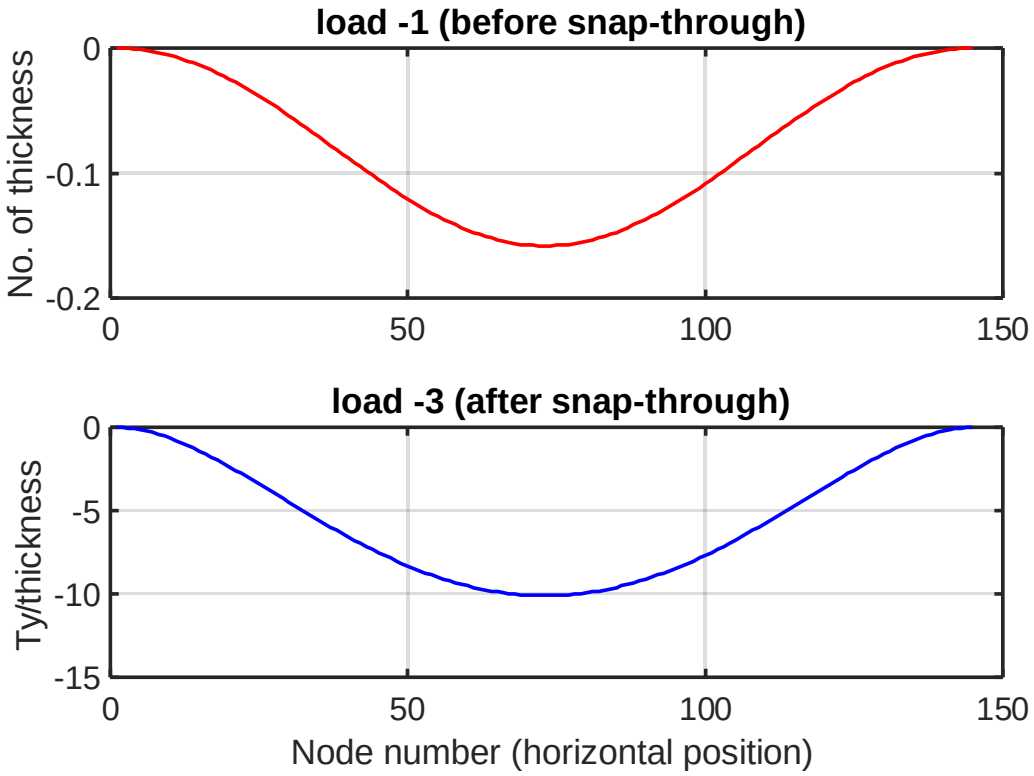

Figure 9. Deformation of the Curved Beam under Uniform Downward Loadings of 1 lb/in (Top) and 3 lbs/in (Bottom).

(1) Generate a series of nonlinear displacements from the finite element under loading that are relevant to the structure and its expected excitation. These nonlinear displacements are typically static ones, which are faster to determine, but dynamic ones are also applicable. These nonlinear displacements should span the range of expected deformations of the structure.

(2) Project the nonlinear displacements on the selected normal modes.

(3) Perform a POD analysis of the projection coefficients, selecting the eigenvectors corresponding to the largest eigenvalues.

(4) Using the eigenvectors, transform the original modes into modes that span the structure.

The application of this process to the curved beam using displacements under uniform pressures from -0.1 lb/in to -4.5 lbs/in led to the mode shown on Figure 10 (from the eigenvector with largest eigenvalue). Clearly, this new mode is much closer to the reference static displacements implying that it will be dominant in the response of the curved beam.

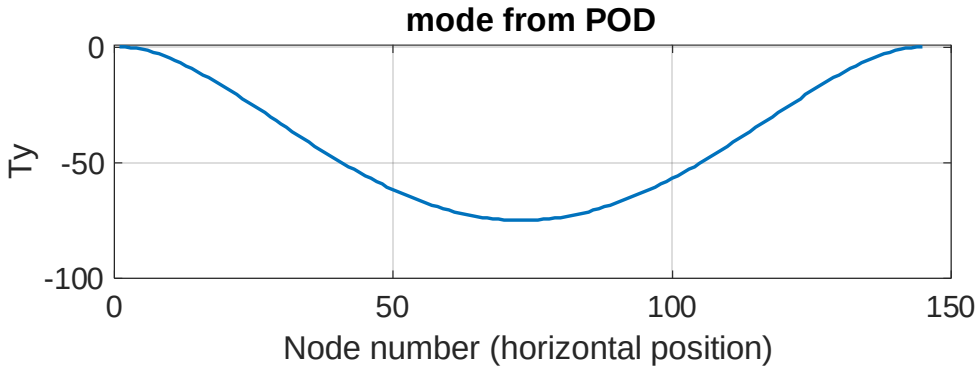

Figure 10. Mode Shape of the POD Mode.

It is not enough to consider only one mode and thus others must be appended. They could be chosen either as originating from additional eigenvectors of the POD analysis, especially those with eigenvalues larger than the floor, or from linear modes.

4.2 Optimization of the Dual Basis $\hat{\varphi}_d$

Past efforts have shown that the dual modes are often very efficient in complementing the transverse modes, i.e., that they represent well reference nonlinear responses with only a few modes. In some cases, a slow convergence of the representation with respect to the number of dual modes has been observed thereby penalizing the computational benefits of the NLROM but also, as pointed out above, potentially leading to stability problems of this model.

On that basis, it was questioned whether it would be possible to rotate a given basis of dual modes into one in which the number of dominant duals is reduced. This effort could be accomplished as done with the transverse basis by performing a POD of the projections of the reference deflections, but this strategy may lead to a set of dual modes too biased toward the reference data.

A different approach was adopted here that is similar in spirit to some aspects of the construction of the optimum thermal modes [46]. Specifically, recognize first that the dominant stiffness coefficient $K_{ijl}^{(2)}$ where '*i*' and '*j*' refer to linear (transverse) modes and '*l*' is associated with a dual. These terms are the most significant ones (besides the linear) because (i) they are the main coupling mechanism between the linear and the dual modes and thus induce the membrane softening effects and (ii) because they are multiplied by a first power of the dual modes generalized coordinates which are typically much smaller than their linear modes counterparts. So, quadratic terms involving two or more dual modes coordinates have typically small effects and are often neglected (as proposed in [47]). Cubic terms involving the dual modes are also known to be very small.

Given the linearity of the coefficients $K_{ijl}^{(2)}$ with respect to the dual mode l, see Eqs (17)-(18), it is concluded that the coefficient $\tilde{K}_{ijl}^{(2)}$ corresponding to a linear combination of dual modes

$$\tilde{\boldsymbol{\psi}}^{(l)} = \sum_n \gamma_n \boldsymbol{\psi}^{(n)} \qquad (42)$$

where the summation extend over the dual mode indices, would be given by

$$\tilde{K}_{ijl}^{(2)} = \sum_n \gamma_n K_{ijn}^{(2)} \qquad (43)$$

On this basis, one can define an optimization of the dual mode basis seeking to maximize, with respect to the parameters γ_n, one or a particular set of coefficients $\tilde{K}_{ijl}^{(2)}$ for specific values of *i* and *j*. Of particular interest would be the optimization of the dual associated with transverse mode 1, i.e., $\tilde{K}_{11l}^{(2)}$. Note in this effort that a normalization constraint should be imposed on the parameters γ_n to avoid an unbounded solution.

Define here $K_{ttd}^{(2)} = \left[K_{ttd_1}^{(2)}, K_{ttd_2}^{(2)}, ..., K_{ttd_n}^{(2)} \right]$ the vector of quadratic coefficients of interest where the first two indices could be any pair of transverse mode numbers but remain the same for all terms. Introduce similarly $\gamma = \left[\gamma_1, \gamma_2, ..., \gamma_n \right]^T$. The problem is then to maximize $\left| K_{ttd}^{(2)} \gamma \right|^2$ given $\gamma^T \gamma = 1$ (the constraint could be changed to be adapted to different problem) where

$$\left| K_{ttd}^{(2)} \gamma \right|^2 = \left(K_{ttd}^{(2)} \gamma \right)^T \left(K_{ttd}^{(2)} \gamma \right) = \gamma^T K_{ttd}^{(2)T} K_{ttd}^{(2)} \gamma \qquad (44)$$

Adding the constraint through a Lagrange multiplier, the objective function becomes

$$f = \gamma^T K_{ttd}^{(2)T} K_{ttd}^{(2)} \gamma + \lambda \left(\gamma^T \gamma - 1 \right) \qquad (45)$$

Rewriting in index format and differentiating yields

$$f = \gamma_i V_{ij} \gamma_j + \lambda \left(\gamma_i \gamma_i - 1 \right) \qquad (46)$$

$$\frac{\partial f}{\partial \gamma_k} = V_{kj}\gamma_j + V_{ik}\gamma_i + 2\lambda\gamma_k \qquad (47)$$

where $V = K_{ttd}^{(2)T} K_{ttd}^{(2)}$ and thus is symmetric so that

$$\frac{\partial f}{\partial \gamma_k} = 2V_{kj}\gamma_j + 2\lambda\gamma_k \qquad (48)$$

Setting the above derivative to zero to achieve the optimum leads to

$$V_{kj}\gamma_j = -\lambda\gamma_k \qquad (49)$$

Rewriting this equation in matrix form yields the eigenvalue problem

$$\mathbf{V}\,\boldsymbol{\gamma} = \lambda\,\boldsymbol{\gamma} \qquad (50)$$

The corresponding eigenvector(s) $\boldsymbol{\gamma}$ with largest eigenvalue(s) λ could then be used to rotate the dual modes as in Eq. (42).

Another strategy for the dual modes optimization is based on performing their modal analysis, i.e., solving the eigenvalue problem

$$K_{dd}\boldsymbol{\gamma} = \bar{\lambda}\, M_{dd}\boldsymbol{\gamma} \qquad (51)$$

where K_{dd}, M_{dd} are the dual blocks of the linear stiffness and mass matrices. Eigenvectors in Eq (51) associated with eigenvalues $\bar{\lambda}$ that are in the range of those of the linear modes should likely be eliminated as duplicating the role of the linear modes. Moreover, the eigenvectors with very large eigenvalues would lead to dual modes that are

extremely stiff and thus not likely to contribute significantly to the response. It is thus suggested that the eigenvectors with low eigenvalues but larger than those of the linear modes be kept and that the rotation be carried out as in Eq. (42)

CHAPTER 5 SYMMETRY AND TUNING OF COEFFICIENTS

5.1 Symmetry of Stiffness Matrix

The identification methods reviewed in section 3.3 provide estimates of each of the linear, quadratic, and stiffness coefficient of the reduced order model regardless of any condition that must link them. Such conditions however do exist and result from the fact that the nonlinear geometric restoring force is rooted in elasticity and thus must be a conservative force. Thus, any modal force F_i should be representable as

$$F_i = \frac{\partial V}{\partial q_i} \tag{52}$$

where V is the potential energy, and q_i is the generalized displacement. Since the potential energy V must be the same for all indices i, there is necessarily a connection between different modal forces, more specifically

$$\frac{\partial F_i}{\partial q_j} = \frac{\partial F_j}{\partial q_i} = \frac{\partial^2 V}{\partial q_i \partial q_j} \tag{53}$$

Accordingly, there must exist relations between different sets of stiffness coefficients. To derive these conditions which are referred to here as symmetry conditions, consider Eq. (34)

$$F_i = K_{ij}^{(1)} q_j + K_{ijl}^{(2)} q_j q_l + K_{ijlp}^{(3)} q_j q_l q_p$$

Assume a 3 modes model for which

$$F_1 = \frac{\partial V}{\partial q_1},\ F_2 = \frac{\partial V}{\partial q_2},\ F_3 = \frac{\partial V}{\partial q_3}$$

Then, different components of the modal forces will be considered, integrated to yield the corresponding contributions to the potential energy, and then differentiated to determine the associated terms on the other modal forces. Consider first the linear stiffness terms. On the modal force 1, there is a component $F_{1,L} = K_{12}^{(1)} q_2$ for which the corresponding component of the potential energy is $V_1 = \int F_{1,L}\, dq_1 = \int K_{12}^{(1)} q_2 dq_1 = K_{12}^{(1)} q_2 q_1$. Differentiation of this term with respect to q_2 to obtain the corresponding component of the modal force F_2 gives $F_{2,L} = \frac{\partial V_1}{\partial q_2} = K_{12}^{(1)} q_1$. However, the coefficient of q_1 in the expression of F_2 should be $K_{21}^{(1)}$. Thus, one must have $K_{21}^{(1)} = K_{12}^{(1)}$.

For the quadratic stiffness terms, consider the component $F_{1,Q} = K_{123}^{(2)} q_2 q_3$ for which the corresponding component of the potential energy is $V_2 = \int F_{1,Q}\, dq_1 = \int K_{123}^{(2)} q_2 q_3 dq_1 = K_{123}^{(2)} q_1 q_2 q_3$. Differentiating this expression with respect to q_2 and q_3 yields $F_{2,Q} = \frac{\partial V_2}{\partial q_2} = K_{123}^{(2)} q_1 q_3$ and $F_{3,Q} = \frac{\partial V_2}{\partial q_3} = K_{123}^{(2)} q_1 q_2$. Comparing these terms with those from Eq. (34) yields the symmetry relations $K_{123}^{(2)} = K_{213}^{(2)} = K_{312}^{(2)}$.

Proceeding similarly with all groups of terms leads to the set of symmetry relations listed in Table 1 (no sum for the repeated index, $i < j < l < p$).

Table 1. Symmetry Relations of Stiffness Coefficients.

	F_i	V	$\partial V / \partial q$	Symmetry of Stiffness
Linear stiffness	$K_{ij}^{(1)} q_j$	$K_{ij}^{(1)} q_i q_j$	$F_j = K_{ij}^{(1)} q_i$	$K_{ij}^{(1)} = K_{ji}^{(1)}$
Quadratic stiffness	$K_{ijl}^{(2)} q_j\, q_l$	$K_{ijl}^{(2)} q_i q_j\, q_l$	$F_j = K_{ijl}^{(2)} q_i q_l$ $F_l = K_{ijl}^{(2)} q_i q_j$	$K_{ijl}^{(2)} = K_{jil}^{(2)}$ $K_{ijl}^{(2)} = K_{lij}^{(2)}$
	$K_{ijj}^{(2)} q_j^2$	$K_{ijj}^{(2)} q_i q_j^2$	$F_j = 2K_{ijj}^{(2)} q_i q_l$	$K_{jij}^{(2)} = 2K_{ijj}^{(2)}$
	$K_{iij}^{(2)} q_i q_j$	$\frac{1}{2} K_{iij}^{(2)} q_i^2 q_j$	$F_j = \frac{1}{2} K_{iij}^{(2)} q_i^2$	$K_{jii}^{(2)} = \frac{1}{2} K_{iij}^{(2)}$
Cubic stiffness	$K_{ijlp}^{(3)} q_j\, q_l q_p$	$K_{ijlp}^{(3)} q_i q_j\, q_l q_p$	$F_j = K_{ijlp}^{(3)} q_i q_l q_p$ $F_l = K_{ijlp}^{(3)} q_i q_j q_p$ $F_p = K_{ijlp}^{(3)} q_i q_j q_l$	$K_{ijlp}^{(3)} = K_{jilp}^{(3)}$ $K_{ijlp}^{(3)} = K_{lijp}^{(3)}$ $K_{ijlp}^{(3)} = K_{pijl}^{(3)}$
	$K_{ijll}^{(3)} q_j\, q_l^2$	$K_{ijll}^{(3)} q_i q_j\, q_l^2$	$F_j = K_{ijll}^{(3)} q_i q_l^2$ $F_l = 2K_{ijll}^{(3)} q_i q_j q_l$	$K_{ijll}^{(3)} = K_{jill}^{(3)}$ $K_{lijl}^{(3)} = 2K_{ijll}^{(3)}$
	$K_{ijjp}^{(3)} q_j^2 q_p$	$K_{ijjp}^{(3)} q_i q_j^2 q_p$	$F_j = 2K_{ijjp}^{(3)} q_i q_j q_p$ $F_p = K_{ijjp}^{(3)} q_i q_j^2$	$K_{jijp}^{(3)} = 2K_{ijjp}^{(3)}$ $K_{pijj}^{(3)} = K_{ijjp}^{(3)}$
	$K_{iilp}^{(3)} q_i\, q_l q_p$	$\frac{1}{2} K_{iilp}^{(3)} q_i^2 q_l q_p$	$F_l = \frac{1}{2} K_{iilp}^{(3)} q_i^2 q_p$ $F_p = \frac{1}{2} K_{iilp}^{(3)} q_i^2 q_l$	$K_{liip}^{(3)} = \frac{1}{2} K_{iilp}^{(3)}$ $K_{piil}^{(3)} = \frac{1}{2} K_{iilp}^{(3)}$
	$K_{ijjj}^{(3)} q_j^3$	$K_{ijjj}^{(3)} q_i q_j^3$	$F_j = 3K_{ijjj}^{(3)} q_i q_j^2$	$K_{jijj}^{(3)} = 3K_{ijjj}^{(3)}$
	$K_{iiip}^{(3)} q_i^2 q_p$	$\frac{1}{3} K_{iiip}^{(3)} q_i^3 q_p$	$F_p = \frac{1}{3} K_{iiip}^{(3)} q_i^3$	$K_{piii}^{(3)} = \frac{1}{3} K_{iiip}^{(3)}$
	$K_{iill}^{(3)} q_i q_l^2$	$\frac{1}{2} K_{iill}^{(3)} q_i^2 q_l^2$	$F_l = K_{iill}^{(3)} q_i^2 q_l$	$K_{iill}^{(3)} = K_{liil}^{(3)}$

The symmetry relations can be used to check if the stiffness coefficients are well identified. If the symmetry is well respected for a particular set of coefficients, it could be assumed that these stiffness coefficients are well identified. If not, it can certainly be concluded that at least some of them are badly identified. The existence of the above symmetry relations will be used in connection with the tuning of stiffness coefficients in the following sections.

While not directly relevant here, it should be noted that the potential energy discussed here is the elastic strain energy and thus must be a positive function. This property is essential in proving the positive definiteness of the matrix $\boldsymbol{K}_B$, see [12].

5.2 Tuning of Stiffness Coefficients

The accurate NLROM prediction of discrete events, such as the snap-through or snap-back of the curved beam, requires that the NLROM coefficients induce the appropriate condition, here the existence of a zero eigenvalue of the tangent stiffness matrix, and at the appropriate loading condition. These conditions are not always met by the stiffness coefficients identified as discussed in section 3.3 in which case it might be desirable to develop a strategy to refine an existing identified NLROM.

Over the years, it has traditionally been concluded that the stiffness coefficients whose indices refer to all transverse modes, denoted here as $K_{tt}^{(1)}$, $K_{ttt}^{(2)}$, and $K_{tttt}^{(3)}$, and the linear and quadratic ones involving only one index referring to a dual mode, i.e., $K_{td}^{(1)}$, $K_{dt}^{(1)}$, $K_{dtt}^{(2)}$, and $K_{ttd}^{(2)}$ (note that the dual modes corresponding to indices larger than the

transverse ones) are “well enough” identified. On the contrary, the other coefficients have typically not satisfied the check of symmetry and have been considered neither accurate nor reliable. On that basis, it has been proposed to zero them out leading to “cleaned models” as compared to the “full models” in which all coefficients $K_{dd}^{(1)}$ are retained. One exception to the zeroing out of coefficients involving multiple indices of dual modes are the coefficients which have been found to be well identified by comparison with their values determined directly from the linear stiffness matrix.

For most structures, the generalized coordinates associated with the dual modes are much smaller than their transverse counterparts and thus the neglect of q_d^2 and q_d^3 terms in the cleaned model has often seemed adequate. In practice, cleaned models have been observed to be more stable than the full ones and effectively can be marched numerically faster since the number of products to carry out in the evaluation of the nonlinear stiffness terms is reduced.

The use of cleaned coefficients is however inconsistent with the derivation of the NLROM governing equations and the positive definiteness of the matrix $\boldsymbol{K}_B$ involving the linear, quadratic and cubic coefficients. Moreover, their use in problems exhibiting very delicate nonlinear behaviors, e.g., snap-through of a clamped-clamped curved beam, seems too brutal as small nonlinear stiffness terms may (and indeed do) have a much larger effect owing to the near zero effective stiffness.

The above discussion has motivated a separate effort focused on answering the following questions:

(a) are the coefficients deemed unreliable really so?

(b) if they are unreliable, how could we determine them more reliably than by the methods formulated so far?

(c) do these coefficients actually matter and in what conditions?

To achieve step (a) and, in part, step (c), requires the availability of another finite element software yielding NLROM coefficients that can be trusted and/or known to be consistent with NLROM modeling. Limited prior experience with the Air Force Research Laboratory (AFRL) finite element code based on [52] had suggested that it might be a good candidate. It was decided to use the symmetry of the coefficients as the test to determine whether this AFRL code could be considered as benchmark. Using this finite element on the clamped-clamped curved beam considered earlier in this investigation resulted in a near perfect matching of all relationships between coefficients, the numerical errors in their satisfaction was small enough that it could be construed as numerical noise vs. formulation differences. On that basis, the AFRL code beam modeling is considered a benchmark. Note that a NLROM model satisfying all relationships will be referred to here as "super symmetric"; it guarantees that the nonlinear stiffness forces are conservative, i.e., will not lead to spurious energy input/dissipation that, even small, may be detrimental to the prediction of the snap-through behavior.

Consistently with the above plan, the first task to address was the comparison of the stiffness coefficients identified from a Nastran model and those from the AFRL code model of the identical structure with the exact same basis functions. The structure selected for this comparison was the clamped-clamped curved beam and several bases were

considered, i.e., the three transverse and five dual (3T5D) and 6T7D (6L7D) models discussed in Chapter 6 as well as a 1T1D model which includes the first transverse and the first dual of the 3T5D one.

The model 1T1D has only two modes which are not sufficient to represent the behavior of the clamped-clamped curved beam. Accordingly, it is just used here to do a preliminary check on the symmetry of stiffness coefficients identified from different finite element models which is easy to implement since the number of basis is small. The comparison of coefficients performed for the 1T1D model is in Table 2. The values of the 18 coefficients (linear, quadratic, and cubic) obtained from Nastran and the AFRL code by application of the tangent stiffness matrix with either single or multiple levels are listed. Note that mode 1 is the transverse ("t") while mode 2 is a dual ("d").

As stated earlier, note how well the symmetry of the coefficients is met for the AFRL code model, e.g., $K_{112}^{(2)} = 2K_{211}^{(2)}$ and $K_{1122}^{(3)} = K_{2112}^{(3)}$ to all (7) significant digits outputted. For the Nastran model, the first comparison ($K_{112}^{(2)} = 2K_{211}^{(2)}$) is also satisfied to 7 digits but $K_{1122}^{(3)}$ and $K_{2112}^{(3)}$ differ by an order of magnitude in both single and multiple level identifications. For the coefficients of the cleaned model, the agreement between Nastran and the AFRL code is typically very good but it is hit and miss for the others: $K_{1122}^{(3)}$ is close but $K_{2112}^{(3)}$ is completely off. A similar situation occurs with quadratic coefficients, $K_{222}^{(2)}$ matches well across methods and codes but $K_{122}^{(2)}$ does not.

Table 2. Stiffness Coefficients of the 1T1D Model of the Clamped-Clamped Curved Beam Obtained from Nastran and AFRL Code Finite Element Models.

	Stiffness coefficient	single level (Nastran)	Multi levels (Nastran)	Multi levels (AFRL)
Linear	$K_{11}^{(1)}$	4.569850 10^{6}	4.569850 10^{6}	4.569849 10^{6}
	$K_{12}^{(1)}$	1.644244 10^{1}	1.639386 10^{1}	-4.530981 10^{2}
	$K_{21}^{(1)}$	1.644244 10^{1}	2.843700 10^{1}	-4.530981 10^{2}
	$K_{22}^{(1)}$	1.857135 10^{10}	1.857135 10^{10}	1.857093 10^{10}
Quadratic	$K_{111}^{(2)}$	1.105734 10^{9}	1.105734 10^{9}	1.106010 10^{9}
	$K_{112}^{(2)}$	-3.021570 10^{10}	-3.024704 10^{10}	-3.014157 10^{10}
	$K_{122}^{(2)}$	-2.353559 10^{9}	-2.353559 10^{9}	-3.825756 10^{9}
	$K_{211}^{(2)}$	-1.510785 10^{10}	-1.510785 10^{10}	-1.507079 10^{10}
	$K_{212}^{(2)}$	-1.517122 10^{9}	-3.112120 10^{9}	-7.651512 10^{9}
	$K_{222}^{(2)}$	1.080430 10^{11}	1.080430 10^{11}	1.093611 10^{11}
Cubic	$K_{1111}^{(3)}$	8.948197 10^{10}	8.948351 10^{10}	9.007757 10^{10}
	$K_{1112}^{(3)}$	3.020189 10^{9}	2.956064 10^{9}	-2.847274 10^{10}
	$K_{1122}^{(3)}$	1.226251 10^{12}	1.226218 10^{12}	1.242726 10^{12}
	$K_{1222}^{(3)}$	-3.637409 10^{11}	-3.637819 10^{11}	-3.992950 10^{11}
	$K_{2111}^{(3)}$	1.006726 10^{9}	9.773128 10^{8}	-9.490912 10^{9}
	$K_{2112}^{(3)}$	1.148455 10^{11}	1.149881 10^{11}	1.242726 10^{12}
	$K_{2122}^{(3)}$	-1.091223 10^{12}	-1.091379 10^{12}	-1.197885 10^{12}
	$K_{2222}^{(3)}$	-8.213170 10^{12}	-8.212456 10^{12}	6.695294 10^{12}

The large relative difference between the linear coupling terms $K_{12}^{(1)}$ and $K_{21}^{(1)}$ may be surprising but note that this a shallow curved beam. The coupling between

transverse and in-plane displacements should be small. The two modes are composed of one transverse mode which is focused on capturing transverse displacement and one dual mode which is focused on in-plane displacement. So, both of these coefficients should be much smaller than the diagonal terms and the values shown are admissible considering the large values of $K_{11}^{(1)}$ and $K_{22}^{(1)}$.

In the remainder of this section, it is desired to extend the comparisons done above on the 1T1D model to 2 NLROMs with larger bases, i.e., 3T5D and 6L7D. One possible strategy is to compare, as discussed above, the coefficients that related to each by symmetry. Another, simpler strategy would be to compare the coefficients identified from Nastran with their counterparts obtained similarly from the Air Force code. The data of Table 2 would suggest that the comparison is meaningful: the coefficients that respect symmetry when identified with Nastran also match their Air Force code counterparts and the most significant terms such as $K_{111}^{(2)}$ and $K_{1111}^{(3)}$ also match each other.

To further support the appropriateness of this comparison, shown in Figure 11 are the deflections induced by a uniform load of 4.5lbs/in (i.e., well above the snap-through threshold of 2.4lbs/in) as predicted by Nastran and several NLROMs. Clearly, the full NLROM constructed from the AFRL finite element code gives predictions that match perfectly the corresponding Nastran results. On the contrary, the NLROM identified from Nastran clearly yield unacceptable results in the horizontal direction. These observations support the expectation that the NLROM stiffness coefficients identified from the Air Force code can serve as target for those obtained by Nastran.

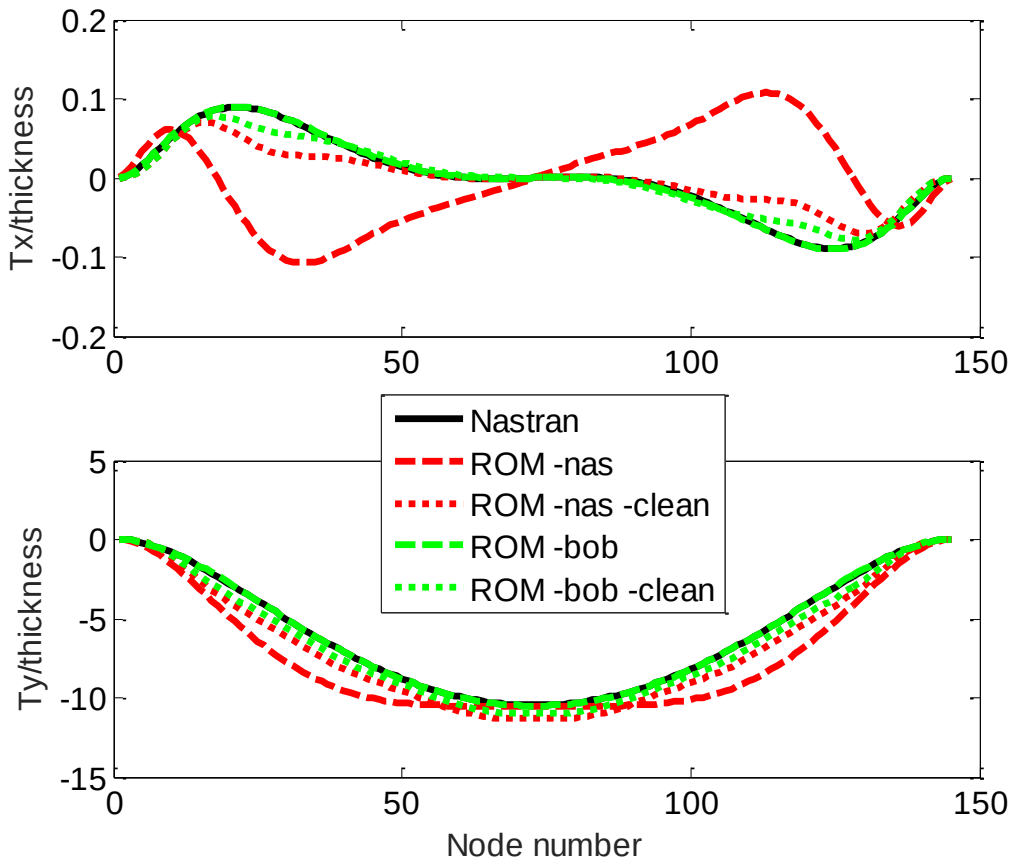

Figure 11. In-plane/Horizontal (Top) and Transverse/Vertical (Bottom) Displacements of the Clamped-Clamped Curved Beam under a Uniform Pressure of 4.5lbs/in. Nastran, Full and Cleaned 3T5D NLROMs Developed from Nastran ("nas") and Air Force Code ("bob") Finite Element Models.

It is further worthwhile to also assess the cleaned version of these models from Figure 11. The Air Force code identified NLROM is worsened somewhat by the cleaning process demonstrating that the cleaned coefficients have an effect on the predictions. On the contrary, the Nastran identified NLROM has noticeably improved by the cleaning suggesting that the cleaned coefficients cannot be considered reliable. Moreover, there is still a slight difference between this cleaned model and the one identified from the Air Force code indicating that differences in the coefficients retained after the cleaning, i.e., the most important ones, also occur.

Proceeding with the comparison for the 3T5D and 6L7D models, the relative error between the corresponding Nastran and the AFRL code identified values of each set of coefficients was evaluated as

$$error = \frac{K_{Nastran} - K_{Bobtran}}{K_{Bobtran}} \times 100\% \qquad (54)$$

These relative errors are shown in Figure 13-Figure 18 for the linear, quadratic, and cubic coefficients. Note that the errors are plotted by groups as to easily identify those for which a good matching takes place and the others.

The results shown in Figure 13-Figure 18 clearly substantiate the prior observations that justified the use of cleaned models: the cubic coefficients $K^{(3)}_{tttd}$, $K^{(3)}_{dttt}$, $K^{(3)}_{ttdd}$, $K^{(3)}_{dttd}$, $K^{(3)}_{tddd}$, $K^{(3)}_{dtdd}$, $K^{(3)}_{dddd}$ identified from the Nastran finite element model are effectively almost always vastly different from those determined from the AFRL code benchmark model. The situation is less dramatic for the quadratic terms but very significant errors still occur quite often for $K^{(2)}_{tdd}$, $K^{(2)}_{dtd}$, and $K^{(2)}_{ddd}$. These observations thus support the use of cleaned models in general.

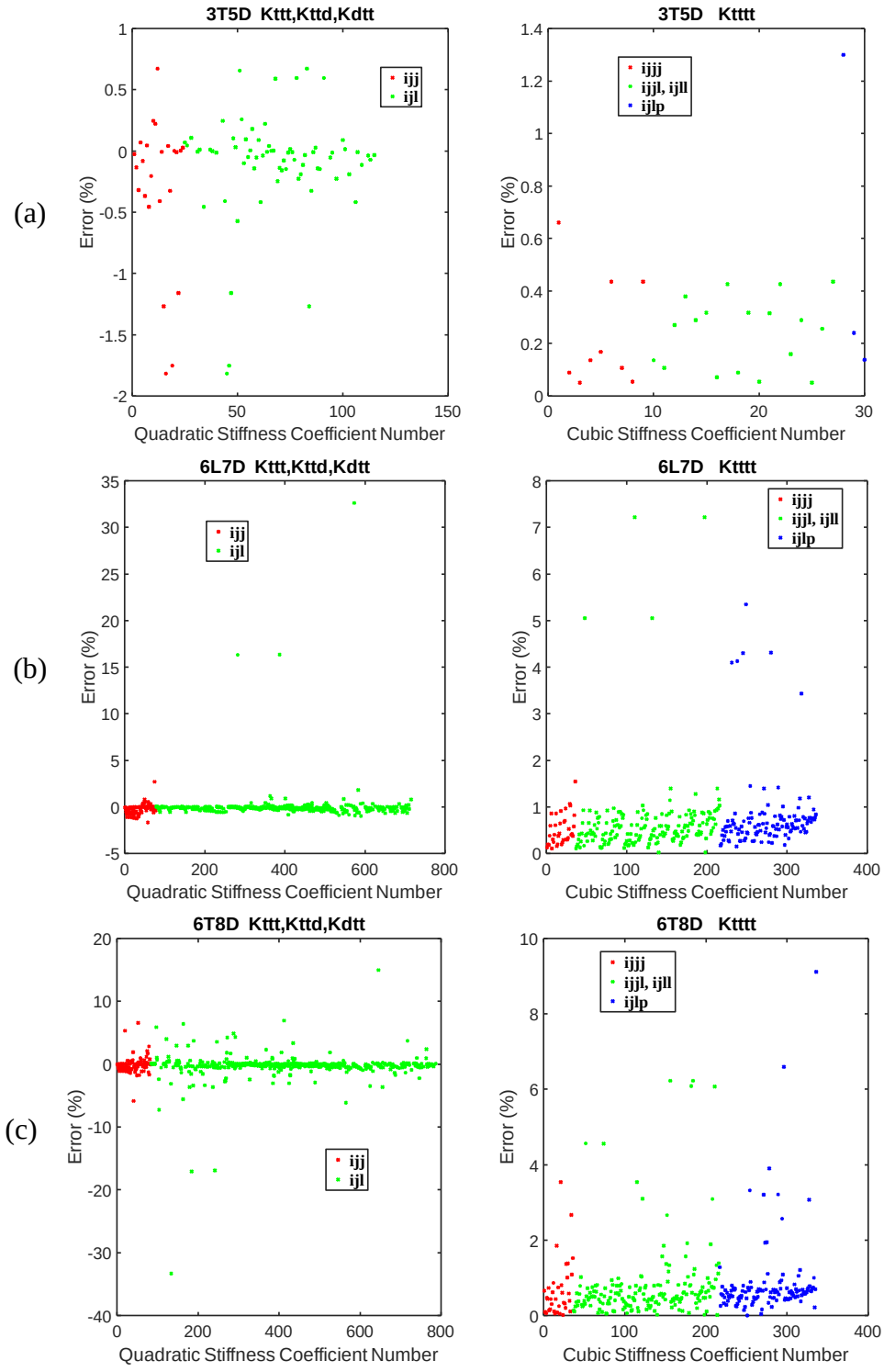

Figure 12 Relative Errors of the Nastran Identified Cleaned Stiffness Coefficients in Comparison to Their Counterparts from the AFRL Code. (a) 3T5D, (b) 6T7D, and (c) 6T8D NLROMs Discussed in Chapter 6.

The availability of stiffness coefficients identified from Nastran and from the AFRL code for the same basis allows to assess one more presumed property of the Nastran identified coefficients, i.e., that those involving 2 or more indices are less accurate than those that relate to 1 mode only. This was checked by comparing the differences of the cleaned stiffness coefficients (the other ones not being reliable) determined from Nastran and from the AFRL code, as done in Figure 13-Figure 18 and for three different bases. These comparisons are shown in Figure 12. Overall, the vast majority of these errors are small, a few percent or less, and thus it is difficult to draw definite conclusions. However, one pattern that is shown, and was not expected, is that the error appears to be growing as the mode number increasing when considering the coefficients $K_{ttt}^{(2)}$ and $K_{tttt}^{(3)}$.

It should be recognized that the above discussion does not imply that the AFRL code is a better or worse nonlinear finite element code than Nastran. Rather, it only demonstrates that the Nastran nonlinear geometric formulation is not consistent with the one underlying the NLROM construction. Moreover, the above comments technically only apply to beam elements as it is not clear whether the Nastran nonlinear formulations for plate/shell or block elements are similar/exhibit similar issues. For plates/shell, experience on many different models suggests that the issue is indeed similar to that of beams. Similarly, the findings only relate to Nastran models, not any other commercial finite element code.

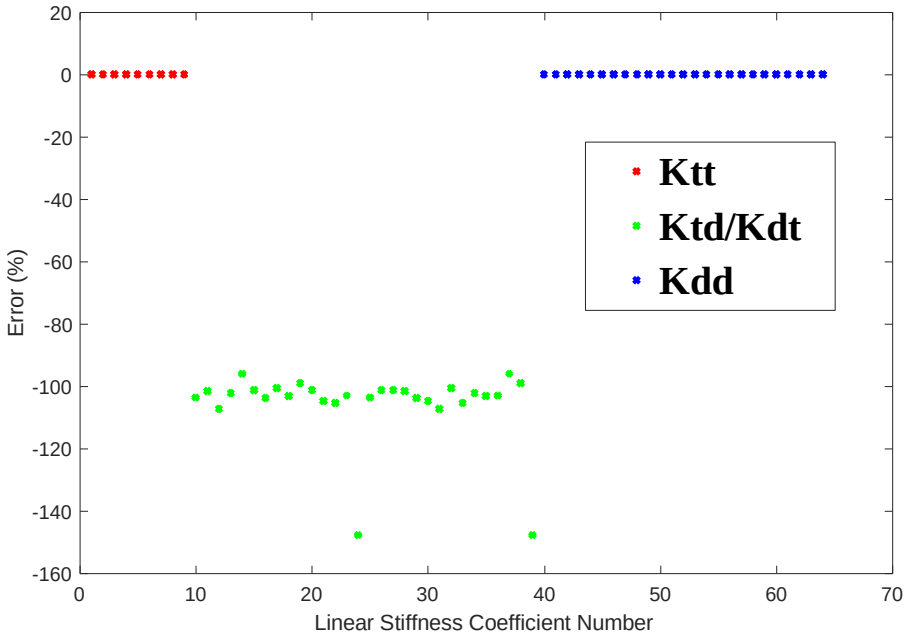

Figure 13. Relative Errors of the Nastran Identified Linear Stiffness Coefficients in Comparison to Their AFRL Code Counterparts, 3T5D Model, T = Transverse, Modes 1-3, D = Dual, Modes 4-8.

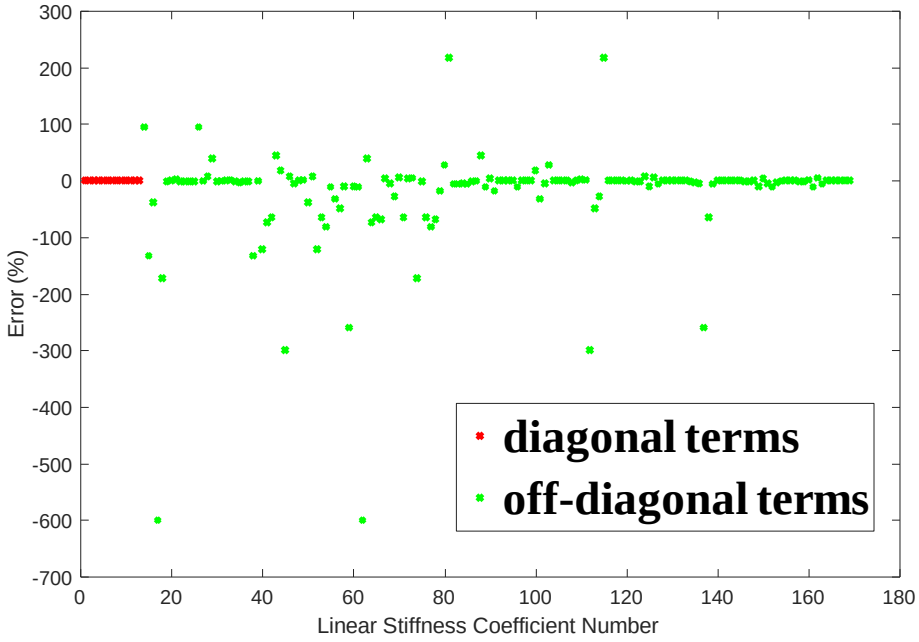

Figure 14. Relative Errors of the Nastran Identified Linear Stiffness Coefficients in Comparison to Their AFRL Code Counterparts, 6L7D Model, L = Transverse, Modes 1-6, D = Dual, Modes 7-13.

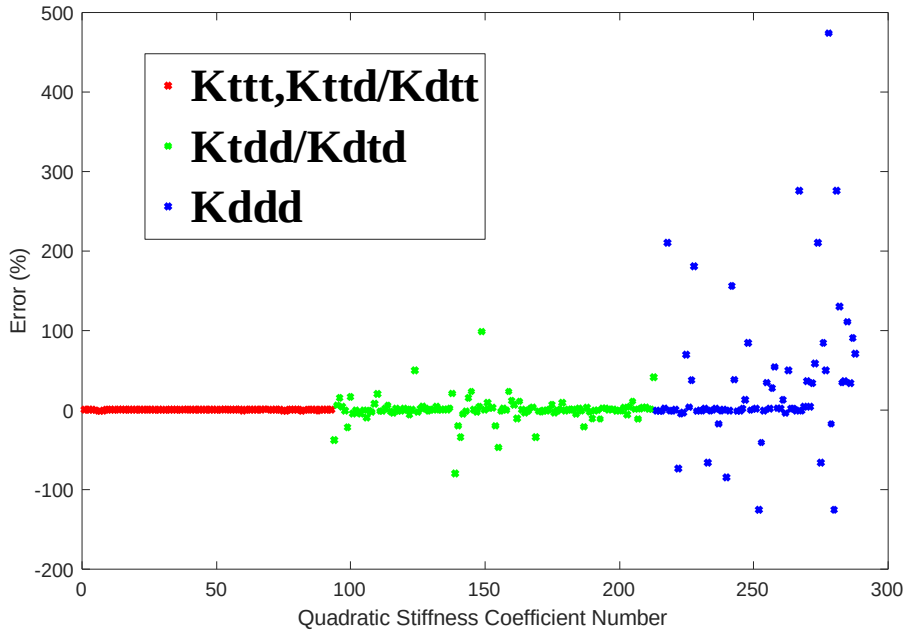

Figure 15. Relative Errors of the Nastran Identified Quadratic Stiffness Coefficients in Comparison to Their AFRL Code Counterparts, 3T5D Model, T = Transverse, Modes 1-3, D = Dual, Modes 4-8.

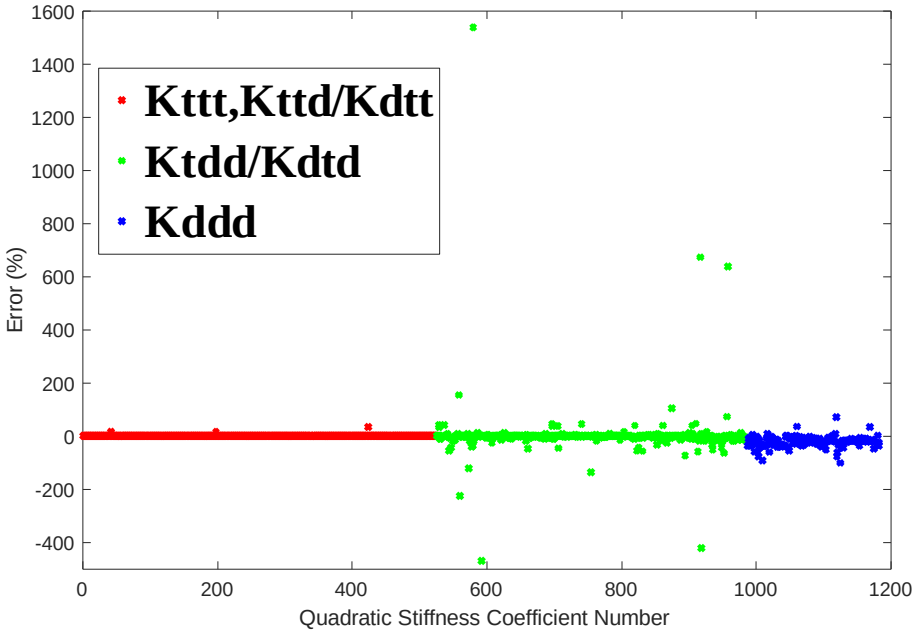

Figure 16. Relative Errors of the Nastran Identified Quadratic Stiffness Coefficients in Comparison to Their AFRL Code Counterparts, 6L7D Model, L = Transverse, Modes 1-6, D = Dual, Modes 7-13.

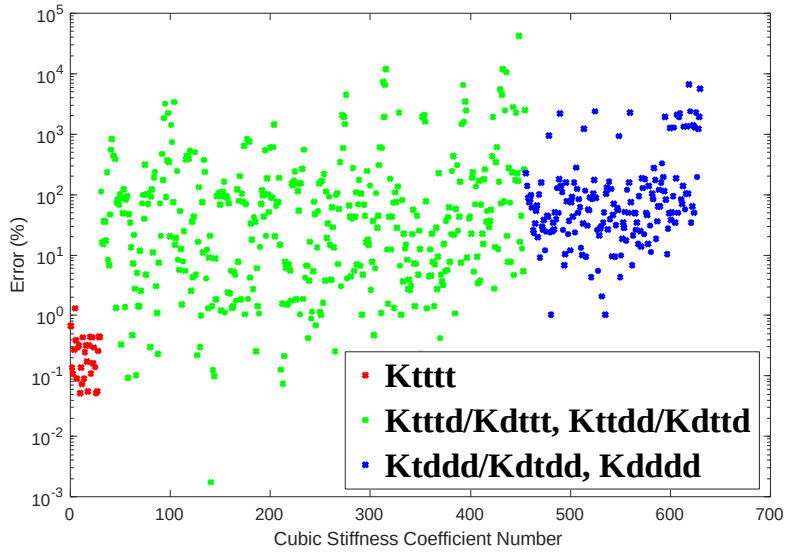

Figure 17. Relative Errors of The Nastran Identified Cubic Stiffness Coefficients in Comparison to Their AFRL Code Counterparts, 3T5D Model, T = Transverse, Modes 1-3, D = Dual, Modes 4-8.

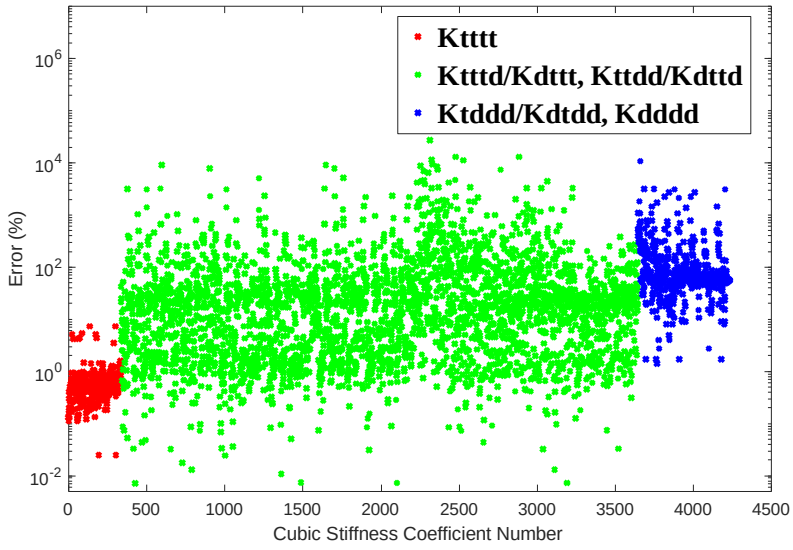

Figure 18. Relative Errors of the Nastran Identified Cubic Stiffness Coefficients in Comparison to Their AFRL Code Counterparts, 6L7D Model, L = Transverse, Modes 1-6, D = Dual, Modes 7-13.

From the above comments, it is expected that the cleaned model is an appropriate NLROM for most structures in which the dual modes are not, or not largely excited on their own. One counterexample is the present clamped-clamped curved beam the response

of which was shown to be very sensitive to small changes in the coefficients [49]. For this structure, it is surmised at this point that cleaning the coefficients will modify the response, see Chapter 6 for confirmation. It is thus desirable in such cases to be able to obtain meaningful values of some or all of the coefficients $K^{(2)}_{tdd}$, $K^{(2)}_{dtd}$, $K^{(2)}_{ddd}$, $K^{(3)}_{tttd}$, $K^{(3)}_{dttt}$, $K^{(3)}_{ttdd}$, $K^{(3)}_{dttd}$, $K^{(3)}_{tddd}$, $K^{(3)}_{dtdd}$, and $K^{(3)}_{dddd}$, from specifically selected Nastran runs. The NLROM including any of these coefficients identified as below will be referred to as "extended".

Then, the questions to address are (i) what run should be carried out and (ii) how the coefficients should be identified. Here we introduce two strategies performing tuning on stiffness coefficients, one based on modal forces, the other one based on generalized coordinates of NLROM.

5.2.1 Tuning Based on Modal Force

Assuming that the response is strongly dominated by the mode 1 (either the first transverse mode or the first POD mode, see section 4.1), the coefficients $K^{(2)}_{111}$ and especially $K^{(3)}_{1111}$ will play a key role in the capture of the events and thus may be tuned to capture it and/or provide an improved prediction of the response in the neighborhood of this event. As shown in Chapter 6, a large sensitivity of the response of the clamped-clamped curved beam to the coefficient $K^{(3)}_{1111}$ was observed and a very slight fine tuning of its value made a significant difference in predictions.

In general, it may be argued that the fine tuning should involve a series of critical parameters, not just one. A formal process to achieve this tuning was formulated based on the availability of finite element static data, displacements and modal forces. Specifically, these quantities would be related by the NLROM governing equations, i.e., Eq. (34), if the NLROM was an exact match of Nastran. In this equation, the values of the generalized coordinates q_j are the projections of the Nastran displacements on the NLROM basis and F_i are the modal forces, i.e., the projections of the loading on the NLROM basis. Since the NLROM is not an exact match of Nastran, the modal forces $\hat{F}_i$ predicted by Eq. (34) based on the projections q_j and the NLROM parameters $\hat{K}_{ij}^{(1)}$, $\hat{K}_{ijl}^{(2)}$ and $\hat{K}_{ijlp}^{(3)}$ are

$$\hat{K}_{ij}^{(1)}\, q_j + \hat{K}_{ijl}^{(2)}\, q_j\, q_l + \hat{K}_{ijlp}^{(3)}\, q_j\, q_l\, q_p = \hat{F}_i \qquad (55)$$

What is desired here then is to modify the NLROM parameters, from $\hat{K}_{ij}^{(1)}$, $\hat{K}_{ijl}^{(2)}$, and $\hat{K}_{ijlp}^{(3)}$ to $K_{ij}^{(1)}$, $K_{ijl}^{(2)}$, and $K_{ijlp}^{(3)}$ so that Eq. (34) holds. Subtracting Eq. (55)from Eq. (34) leads to

$$\Delta K_{ij}^{(1)}\, q_j + \Delta K_{ijl}^{(2)}\, q_j\, q_l + \Delta K_{ijlp}^{(3)}\, q_j\, q_l\, q_p = \Delta F_i = F_i - \hat{F}_i \qquad (56)$$

where

$$\Delta K_{ij}^{(1)} = K_{ij}^{(1)} - \hat{K}_{ij}^{(1)}, \Delta K_{ijl}^{(2)} = K_{ijl}^{(2)} - \hat{K}_{ijl}^{(2)}, \Delta K_{ijlp}^{(3)} = K_{ijlp}^{(3)} - \hat{K}_{ijlp}^{(3)} \qquad (57)$$

The system of Eq. (56) can be rewritten in the matrix-vector form

$$\boldsymbol{Q}\,\Delta\boldsymbol{K} = \Delta\boldsymbol{F} \tag{58}$$

Since the number of coefficients is typically very large, it is not reasonable to expect that there would be enough Nastran data to estimate all variations in the coefficients. To palliate this situation, it will be assumed here that the identification of the original set of coefficients has been done carefully so that the parameters $\hat{K}_{ij}^{(1)}$, $\hat{K}_{ijl}^{(2)}$, and $\hat{K}_{ijlp}^{(3)}$ are close to the desired ones $K_{ij}^{(1)}$, $K_{ijl}^{(2)}$, and $K_{ijlp}^{(3)}$. Then, Eq. (58) can be viewed as a constraint in the minimization of the overall magnitude of the change in NLROM parameters quantified by $\|\Delta\boldsymbol{K}\|$. Proceeding with an implementation of the constraints of Eq. (58) by Lagrange multipliers, denoted collectively by the vector $\boldsymbol{\lambda}$, leads to the linear system of equations

$$\Delta\boldsymbol{K} + \boldsymbol{Q}^T\,\boldsymbol{\lambda} = \boldsymbol{0} \tag{59}$$

Combining this condition with the constraints leads to the final equations

$$\begin{pmatrix} \boldsymbol{I} & \boldsymbol{Q}^T \\ \boldsymbol{Q} & \boldsymbol{0} \end{pmatrix} \begin{pmatrix} \Delta\boldsymbol{K} \\ \boldsymbol{\lambda} \end{pmatrix} = \begin{pmatrix} \boldsymbol{0} \\ \Delta\boldsymbol{F} \end{pmatrix} \tag{60}$$

To implement this strategy, it is necessary to know that the discrepancy between F_i and $\hat{F}_i$ originates from slight errors in the NLROM parameters, not from a truncation error in Eq. (34). That is, the representation error of the Nastran data must be very small. In practice, the truncation error may just be small but not very small in which the exact satisfaction of the modal force constraint may actually be inappropriate and potentially damage the prediction capabilities of the model.

5.2.2 Tuning Based on Generalized Coordinates

The second tuning approach proposed here is to rely on actual response, as opposed to made up imposed displacements, to a load that is at least somewhat similar to the one of which the response is desired. Regarding the identification, it is proposed here to rely on a least square strategy directly at the level of the generalized coordinates. That is, to select the coefficients to be identified so that the predicted generalized coordinates are as close as possible to those obtained by projecting the Nastran response on the basis for the specified loading cases. Specifically, it is proposed to minimize

$$E = \sum_{i=1}^{n_l} \sum_{j=1}^{M} w_j^{(1)} \left[q_{j,i}^{Nas} - q_{j,i}^{ROM} \right]^2 \qquad (61)$$

where n_l and M are the number of load cases considered for the identification and the number of modes in the NLROM basis, and $w_j^{(1)}$ denotes a set of positive weights. Moreover, $q_{j,i}^{Nas}$ and $q_{j,i}^{ROM}$ are the values of the generalized coordinate 'j' in load case 'i' obtained by projection of the Nastran finite element response and by integration of the NLROM governing equations, respectively. Note that the latter set of values is implicitly dependent on the coefficients to be identified.

Besides the deviation between generalized displacements from Nastran and NLROM, the magnitude of the stiffness coefficients could also be added into consideration which lead to

$$E = \sum_{i=1}^{n_l} \sum_{j=1}^{M} w_j^{(1)} \left[q_{j,i}^{Nas} - q_{j,i}^{ROM} \right]^2 + \underline{k}_s^T \, w^{(2)} \underline{k}_s \qquad (62)$$

where $\underline{k}_s$ denotes the vector of values of the cleaned coefficients to be identified and $w^{(2)}$ is a positive definite weight matrix.

For a given load, a commercial finite element software can be used to output the corresponding nonlinear displacement from which the generalized coordinates can be obtained by projection on the selected basis in NLROM. For the same load, the corresponding generalized coordinates can also be obtained from NLROM given the stiffness coefficients. In general, there would be some difference between the two sets of generalized coordinates which will depend on the identified stiffness coefficients. So, the basic idea is to minimize the difference by varying the stiffness coefficients.

The process of minimization was performed in MATLAB using its built-in function 'fminunc' and is summarized in the flowchart below,

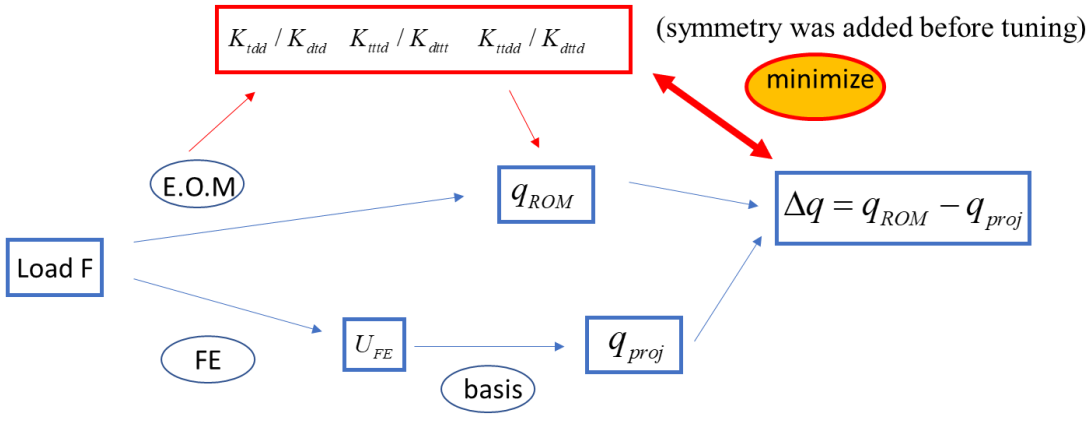

Figure 19. Flowchart of Generalized Coordinates-Based Stiffness Tuning

The minimization of E may be expensive as it requires iterative solutions of the NLROM governing equations which are nonlinear. There are four ways to reduce the computational cost:

(i) Tuning only on "super symmetric" stiffness, i.e. only change $K_{123}^{(2)}$ where $K_{213}^{(2)}$ and $K_{312}^{(2)}$ are imposed to equal $K_{123}^{(2)}$.

(ii) Tuning only the coefficients which are thought to be not well identified, i.e., $K_{tdd}^{(2)}$, $K_{dtd}^{(2)}$, $K_{ddd}^{(2)}$, $K_{tttd}^{(3)}$, $K_{dttt}^{(3)}$, $K_{ttdd}^{(3)}$, $K_{dttd}^{(3)}$, $K_{tddd}^{(3)}$, $K_{dtdd}^{(3)}$, and $K_{dddd}^{(3)}$.

(iii) Tuning only on stiffness coefficients with two or less indices corresponding to dual modes, i.e., $K_{tdd}^{(2)}$, $K_{dtd}^{(2)}$, $K_{tttd}^{(3)}$, $K_{dttt}^{(3)}$, $K_{ttdd}^{(3)}$, and $K_{dttd}^{(3)}$.

(iv) Tuning solely the stiffness coefficients that are likely to provide the largest impact to the response, i.e., related to the dominant transverse and dual modes.

From the validation results, the second tuning approach was more stable than the first one. This finding is rather expected since the second approach is based on the actual computational results of the NLROM while the first one focuses only on the modal force which may lead to some stiffness components deviating very significantly from the true value.

CHAPTER 6 VALIDATION RESULTS

6.1 Validation Plan

The focus of this chapter is on validating the concepts developed in previous sections, in particular the optimization of the linear modes, of the duals, as well as the stiffness coefficients tuning. The three structures discussed in section 2.3 will be considered for this validation effort. More specifically, the optimization of the linear modes of section 4.1 will be carried for all three structures, either as a strategy to reduce the number of linear modes and/or to improve the construction of the duals by creating more distinct dominant modes. The optimization of the duals, as discussed in section 4.2, will be applied solely to the clamped-clamped curved beam. This structure will also be the primary testbed for the stiffness coefficients tuning strategies of Chapter 5 because capturing its snap throughs in either static or dynamic conditions has been shown to require a particular good reduced order model which is difficult to achieve directly using the existing methods of section 3.3. The stiffness coefficients tuning approach will also be performed on the hypersonic panel in an unsuccessful attempt to better capture the occurrence of local buckling. The lack of success in this effort is not due to the tuning strategy but rather to the inadequacy of the basis which it cannot overcome. The validations of the NLROM will be performed on static loading, assessing displacements and eigenvalues of tangent stiffness matrix, as well as on dynamic conditions, and, for a small set of NLROMs, on the response due to a constant applied temperature.

6.2 Application to the Curved Beam

The strategies developed in the last two sections were first applied to the clamped-clamped curved beam shown in Figure 1 under symmetry constraints, i.e., the finite element model was forced to only exhibit symmetric deformations using multi point constraints. This constraint was imposed to reduce the complexity of the problem since the snap-through may occur under both symmetric and antisymmetric motions with the latter occurring at a slight lower load level than the former. The validation results presented below are split into 4 separate efforts/sections:

i) Optimization of the basis.

ii) Results with optimized basis before tuning.

iii) Results after tuning based on modal force.

iv) Results after tuning based on generalized displacements.

6.2.1 Optimization of the Basis

As mentioned in Chapter 4, see Figure 8, the mode shapes of the linear modes of the curved beam are not very similar to the actual deformation induced by a uniform load. Accordingly, the first task focused on the optimization of the linear basis. Specifically, the Nastran static nonlinear displacements induced by the uniform pressures of -0.1, -0.2, -0.3, ..., -4.5 lbs/in were used as reference data and were projected on the first 15 linear modes of the beam. The set of projection coefficients were then processed by a POD and the first eigenvector was retained to construct the first transverse mode. The linear (normal) modes 1, 2, 3, 5, 6 from Nastran SOL103 were added to this first transverse mode and made orthogonal to it. leading finally to 6 transverse modes (denoted as transverse 1 to 6).

Next, 8 dual modes were determined from these 6 transverse modes considering combinations (1-1), (1-2), (1-3), (1-4), (1-5), (1-6), and are shown in Figure 20-Figure 21. While the predictions of this 6T8D NLROM were very close to those of Nastran prior to the snap-through, the model is unstable post snap-through even though the truncation error is quite small. A possible reason for this behavior is an inaccurate identification of some of stiffness coefficients as discussed in Chapter 5. To circumvent this issue, it was desired here to proceed with an optimization of the dual modes to reduce the size of the basis and hopefully improved the predictive capabilities of the NLROM.

Before performing this optimization, it is useful to investigate the relative magnitudes of the transverse (*T*y) and in-plane (*Tx*) of the linear (see Figure 8) and dual (see Figure 20-Figure 21) modes, see Table 3. Note on this table that the ratio is inverted for the linear and dual modes. It is seen that the (original) linear modes are strongly transverse dominant while the reverse typically holds for the duals, although the ratio of magnitudes is smaller, i.e., there is a large contribution of transverse motions in the duals than in-plane in the linear modes. Moreover, the third dual is clearly transverse dominant.

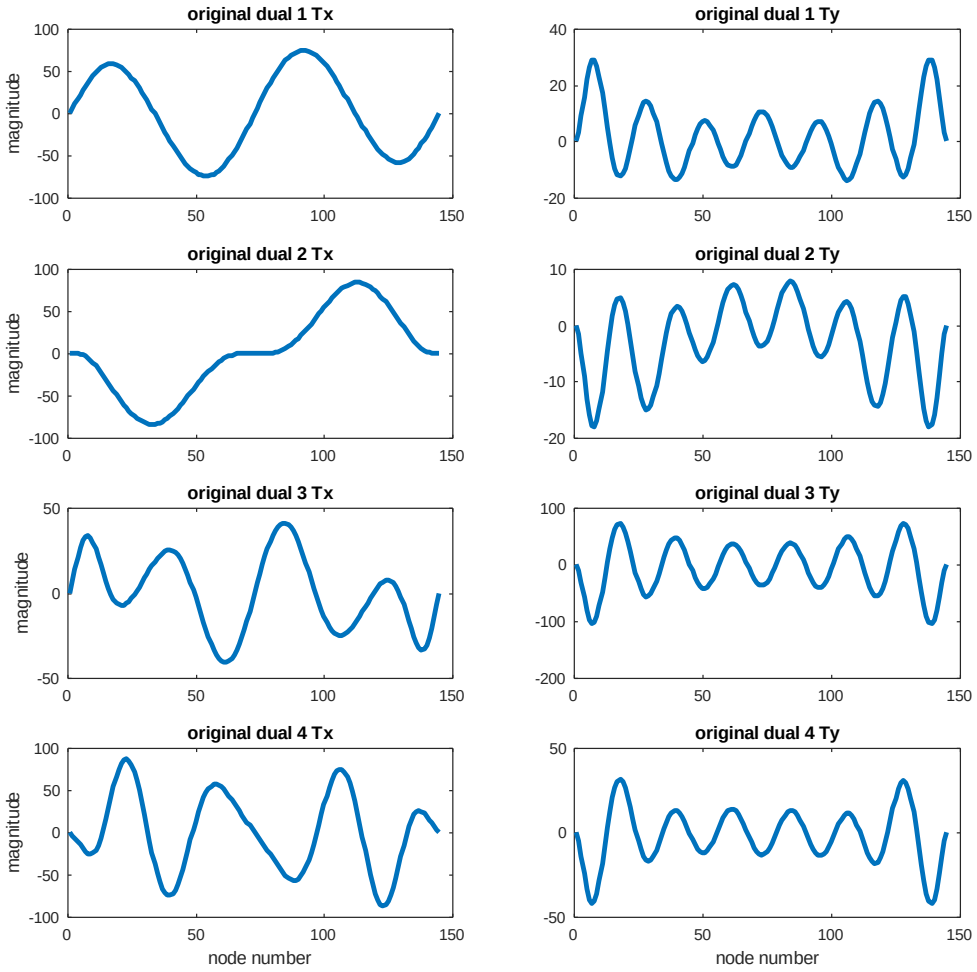

Figure 20. In-plane (Left Column) and Transverse (Right Column) Displacements of the Original Duals 1-4. Curved Beam.

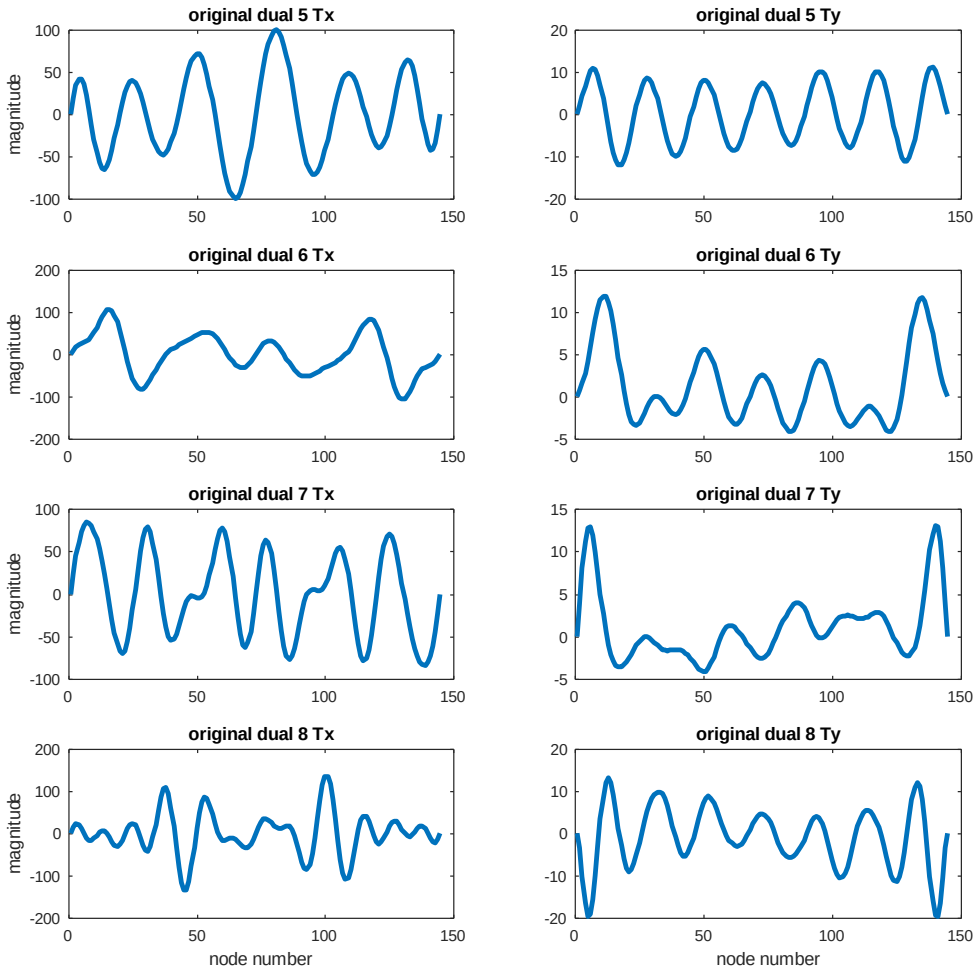

Figure 21. In-plane (Left Column) and Transverse (Right Column) Displacements of the Original Duals 5-8. Curved Beam.

Table 3. Ratios of Transverse and In-plane Displacements NORMs, Linear, Transverse and Dual Modes, Curved Beam.

Norm(*Ty*)/Norm(*Tx*)	Lin. 1	Lin. 2	Lin. 3	Lin. 4	Lin. 5	Lin. 6
	24.04	17.57	14.50	14.97	15.17	15.27
Norm(*Ty*)/Norm(*Tx*)	Tran. 1	Tran. 2	Tran. 3	Tran. 4	Tran. 5	Tran. 6
	61.26	13.97	13.51	14.08	18.96	15.58

Norm(*Tx*)/Norm(*Ty*)	Dual 1	Dual 2	Dual 3	Dual 4	Dual 5	Dual 6	Dual 7	Dual 8
	4.26	6.28	0.50	2.77	7.16	10.81	12.21	6.70

The first effort to optimize the duals proceeded as in Eq. (49) and (50) focusing on the quadratic stiffness term $K_{ttd}^{(2)}$. Since there is only one combination of transverse modes, only one optimum dual can be generated in this process and it is shown in Figure 22. This basis function is fairly similar to the first dual of Figure 20 but the first and last peaks have been reduced. Note that the ratio of the norms of the in-plane and transverse displacement is rather small, 2.57, confirming the visual expectation from Figure 22 that the transverse component is still rather large. Nevertheless, this mode seems very efficient in reducing the representation error of the uniform response post snap-through as shown in Figure 23 (curve "Opti 1") for the loadings of 2.5, 3, 3.5, 4, and 4.5 lbf/inch. More specifically, this error drops from 164% to 32% with that single dual. For comparison, the first original dual only reduces it to 95%. Enriching further the model would require the consideration of other combinations of the transverse modes beside the 1-1.

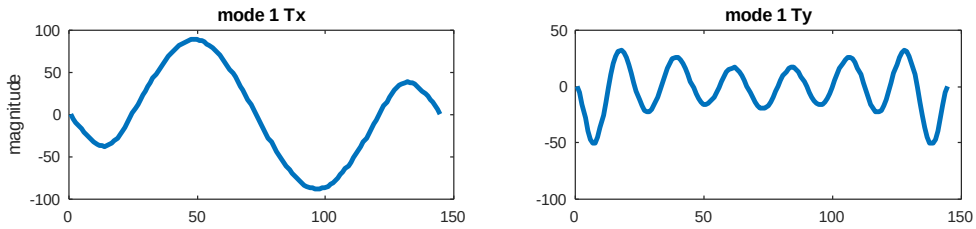

Figure 22. In-plane and Transverse Components of the Dual Mode Optimized According to Eqs (49) and (50). Curved Beam.

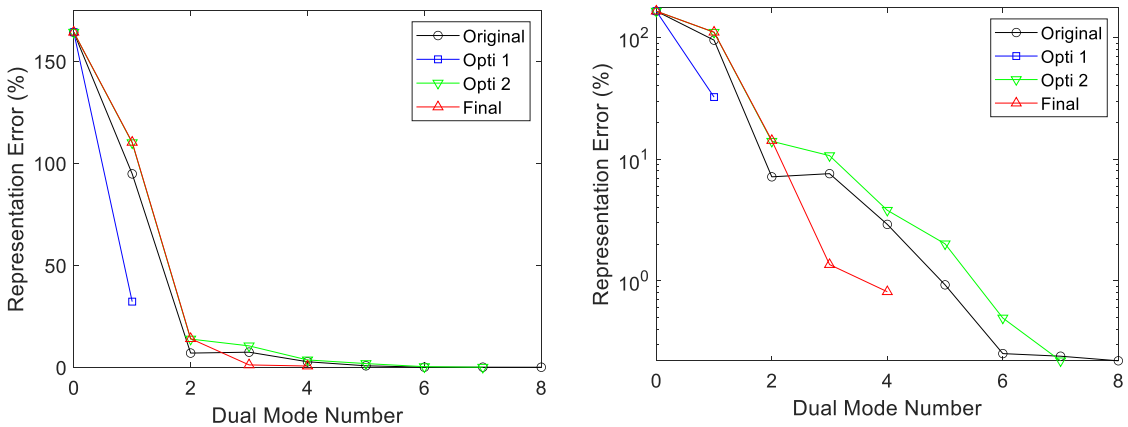

Figure 23. Average Representation Error, in %, of the In-plane Displacements corresponding to Loadings of 2.5, 3, 3.5, 4, and 4.5 lbf/inch (i.e., Post Snap Through) vs. Number of Various Types of Dual Modes. (a) Linear, (b) Log Scale.

It was next desired to assess the benefits of the second dual optimization, i.e., based on the modal analysis of the corresponding blocks of the mass and linear stiffness matrices, see Eq. (51). That computation was performed with the 8 original duals and given in Table 4 are the corresponding eigenvalues while the new duals associated with the corresponding eigenvectors are shown in Figure 24-Figure 25

Table 4. Eigenvalues Associated with the Original Dual Mass and Linear Stiffness Matrices.

1	2	3	4	5	6	7	8
$4.24\ 10^{11}$	$2.05\ 10^{11}$	$1.55\ 10^{11}$	$9.58\ 10^{10}$	$6.34\ 10^{10}$	$1.99\ 10^{10}$	$6.78\ 10^{9}$	$1.33\ 10^{9}$

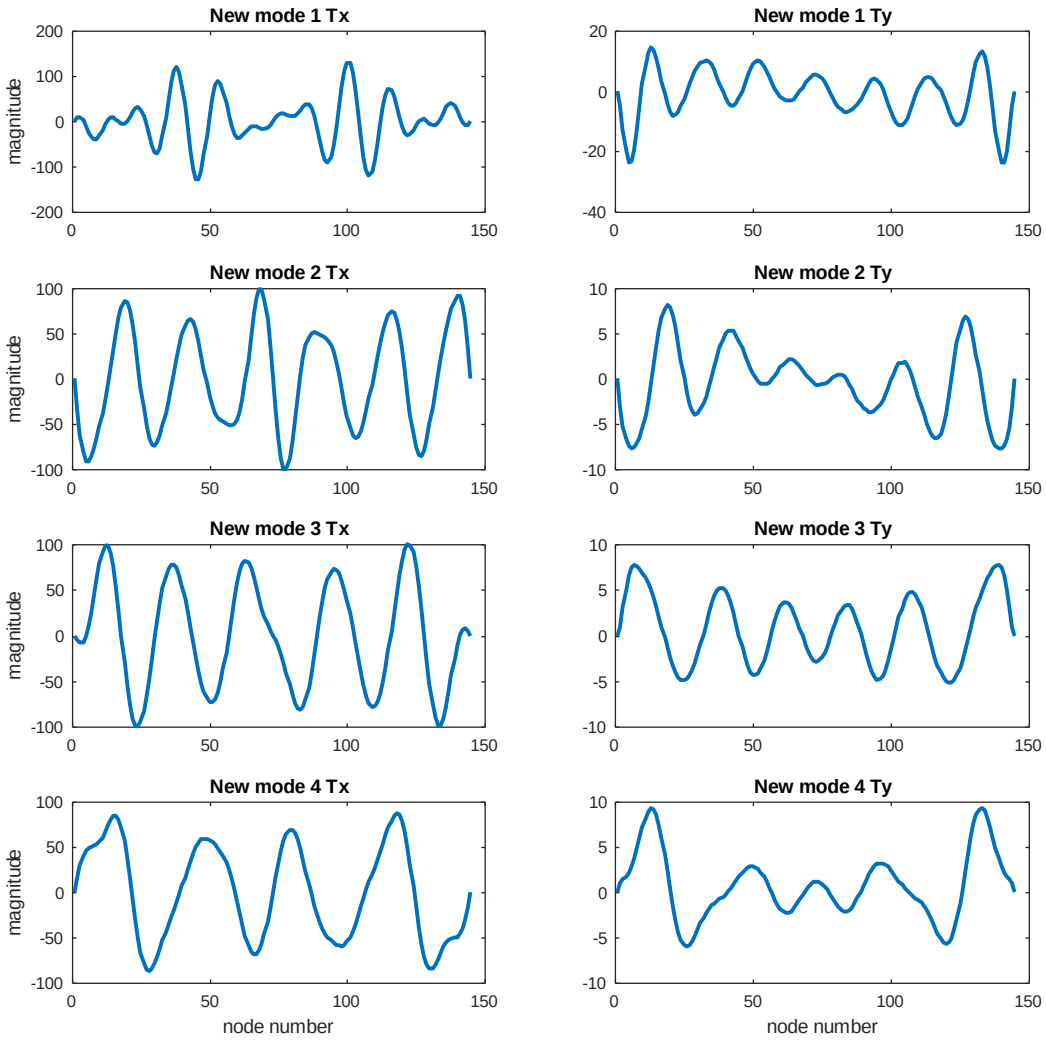

Figure 24. In-plane (Left Column) and Transverse (Right Column) Displacements of the New Duals 1-4 Following the Modal Analysis of Eq. (51). Curved Beam.

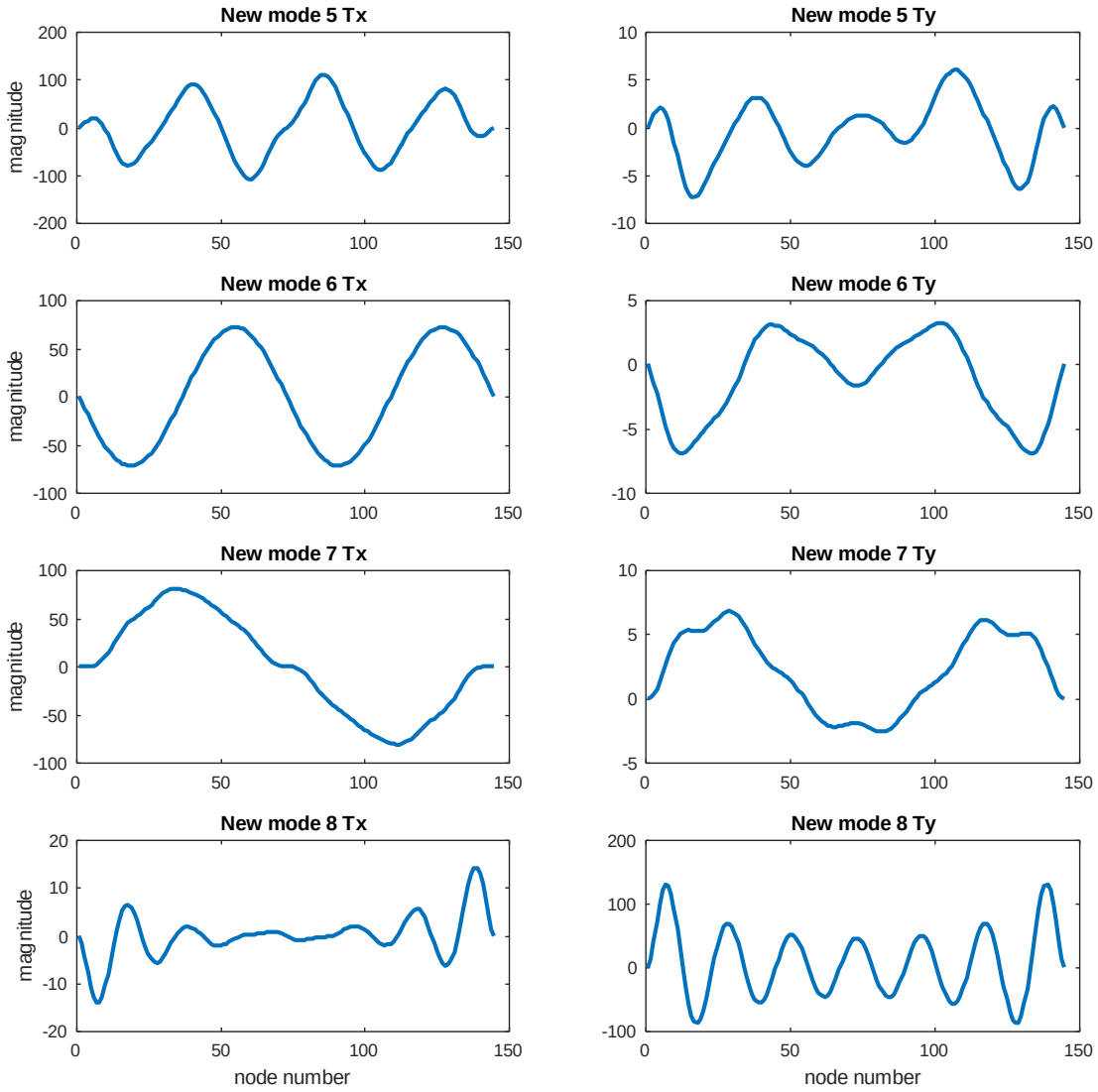

Figure 25. In-plane (Left Column) and Transverse (Right Column) Displacements of the New Duals 5-8 Following the Modal Analysis of Eq. (51). Curved Beam.

Two key observations can be drawn from Figure 24-Figure 25. First, it is seen that the new dual with the lowest eigenvalue (number 8) is primarily transverse while all others are primarily in-plane. In fact, comparing Figure 24-Figure 25 and Figure 20-Figure 21, it appears that the new duals are significantly more in-plane dominant than the original ones. This finding, which is confirmed by the norm ratios shown in Table 5, is actually expected

as the transverse motions are much softer than the in-plane ones and thus the eigenvalue problem splits these motions into separate eigenvectors/new duals.

Table 5. Ratio of Transverse and In-plane Displacements Norms, New Dual Modes, Curved Beam.

	Dual 1	Dual 2	Dual 3	Dual 4	Dual 5	Dual 6	Dual 7	Dual 8
Norm(*Tx*)/Norm(*Ty*)	6.23	14.18	15.21	14.01	18.01	14.72	13.40	0.08

The assessment of these new duals for the representation of the uniform displacement data was carried out as before by evaluating the average in-plane representation error corresponding to the loadings of 2.5, 3, 3.5, 4, and 4.5 lbf/inch, see Figure 23. Note in this figure that the new duals were considered in order of increasing eigenvalue and that the transverse dominant one was not included. That is, the error is presented for new duals in order 7, 6, 5, ..., 1. It is seen that the two in-plane duals with lowest eigenvalues (i.e., 6 and 7 in Figure 25) provide a significant drop in the representation error, yet, not quite as large as the original duals. However, the representation error drops consistently with these new duals at the contrary of the original ones. In this regard, note that the increase in representation error for the original duals associated with dual #3 results from this dual being primarily transverse. Thus, it leads to a decrease of the representation error in the transverse error but at the cost of an increase in the in-plane one. In this light, the continuous decrease of the representation error for the new duals is effectively associated with the decoupling induced by the eigenvalue problem.

It is concluded from the above discussion that the two dual optimization strategies of section 4.2 are both beneficial but in different ways. Then, it was questioned whether they could be combined to achieve an even better selection of duals. To this end, the two duals 7 and 6 were first retained and an optimization as in Eqs (49)-(50) was performed with transverse mode 1 (the POD mode) and the remaining 5 new duals (1 to 5) in Figure 24-Figure 25. Shown in Table 6 are the corresponding quadratic coefficients $K_{11d}^{(2)}$ for d =7 to 11 (new dual modes 1 to 5) after separate identification. Also shown on this table, on the left most column, is the optimum value corresponding to the optimum new dual shown as final dual 3 on Table 7.

The inclusion of this 3rd final dual led to a significant drop in the representation error which still was slightly larger than the 1% usually desired. Accordingly, other combinations of linear modes were considered in the quadratic stiffness coefficients-based optimization and it was found that the 1-3 transverse mode combination led to the largest drop in representation error. Shown in Table 7 and Figure 26 (final dual 4) are the result of this optimization which does lead to yet another notable drop in the representation error, see Figure 23, well below 1%. Note that this 4th new dual appears very similar to the new dual 5 (flipped sign) which is consistent with the very close values of the quadratic stiffness coefficient of mode 11 (new dual 5). Given the low representation error, no further duals were considered leading to a 4 dual mode basis, shown in Figure 26, vs. the original 8.

Table 6. Data and Result of Optimization of New Duals 1-5 Using Eqs (49)-(50) for the 1-1 Combination.

	Index and values of $K_{ijl}^{(2)}$ for the 5 new dual modes before optimization				
$\tilde{K}_{ijl}^{(2)}$	(1,1,7)	(1,1,8)	(1,1,9)	(1,1,10)	(1,1,11)
2.1679e+10	3.7415e+09	6.7323e+09	-5.6926e+09	-1.0910e+10	8.0979e+09

Table 7. Data and Result of Optimization of New Duals 1-5 Using Eqs (49)-(50) for the 1-3 Combination.

	Index and values of $K_{ijl}^{(2)}$ for the 5 new dual modes before optimization				
$\tilde{K}_{ijl}^{(2)}$	(1,3,7)	(1,3,8)	(1,3,9)	(1,3,10)	(1,3,11)
-3.7078e+11	-1.8903e+10	-1.2731e+11	5.0843e+10	4.6443e+10	3.4567e+11

In a final attempt to reduce the basis size, the role of each of the 6 transverse modes was analyzed and it was found that the last 3 transverse modes contributed only little to the reduction of the transverse representation error. Accordingly, they were removed yielding a 3 transverse – 4 dual (3T4D) basis which will be validated in the next section.

It was of interest to assess this basis in comparison to a 3T4D one which would be built following the standard dual construction process. Specifically, 2 duals were taken from each of the 1-1 and 1-2 combinations. Then, the in-plane representation error of the 2 3T4D bases are compared on Figure 27 on the same data as Figure 23. As would be expected, the 4 optimized duals decrease the representation error faster than the one constructed by the regular process. The gain is minimal for the first dual but is much larger for the next two. Eventually, on dual 4, the optimum approach cannot reduce the error

much more but the regular process still can and yields to a final representation error that is very similar to that of the optimized process. This comparison confirms that the benefit of the dual optimization process is primarily in potentially reducing the number of duals necessary.

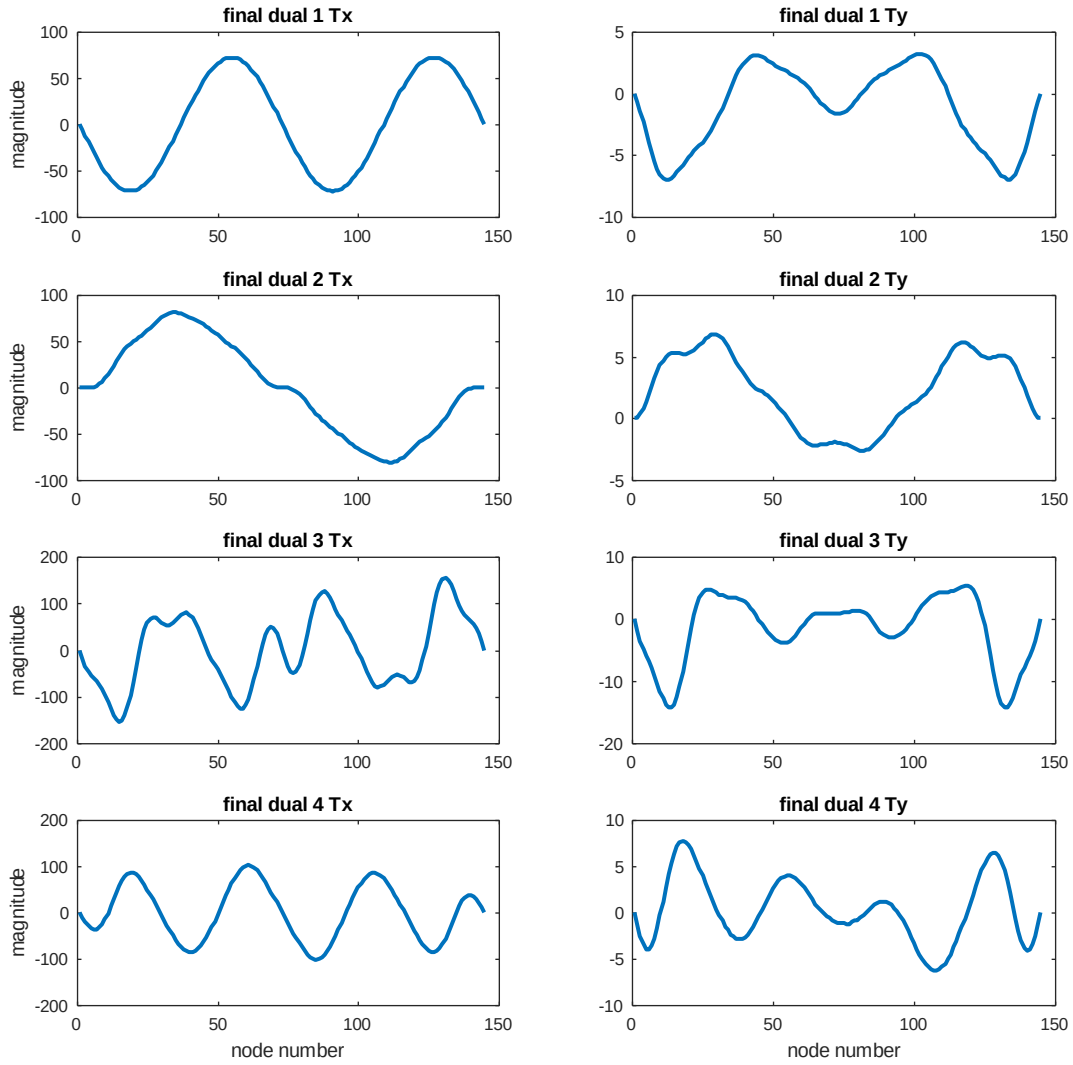

Figure 26. In-plane (Left Column) and Transverse (Right Column) Displacements of the 4 Final Duals Following from the Two Optimizations. Curved Beam.

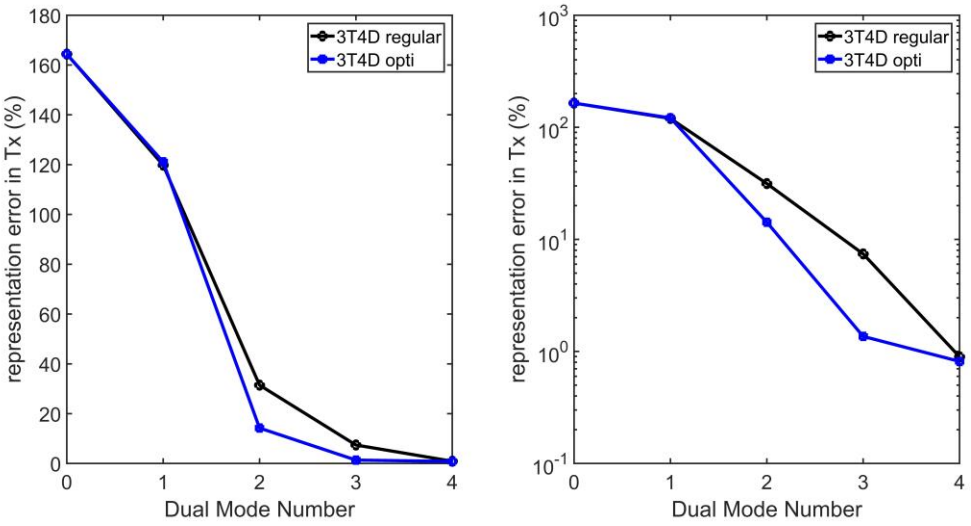

Figure 27. Average Representation Error for the Two 3T4D Models, in %, of the In-plane Displacements corresponding to Loadings of 2.5, 3, 3.5, 4, and 4.5 lbf/inch (i.e., Post Snap Through) vs. Number of Various Types of Dual Modes. (a) Linear, (b) Log Scale.

6.2.2 Results with Optimized Basis before Tuning

The identification of the stiffness coefficients of the 3T4D NLROM were determined using the single-level tangent stiffness approach and the model was cleaned. Then, the assessment of this NLROM started with the comparison of static predictions. The static displacements before snap-through and the location of that event are well captured by the ROM, see Figure 28 and Figure 29, but not as well after snap-through (which occurs for a load of 2.4 lbf/inch). Similar observations can be drawn from the prediction of the lowest eigenvalue of the tangent stiffness matrix, see Figure 30. Note on this figure that the lowest eigenvalues obtained by projecting the Nastran tangent stiffness matrix on the NLROM basis ("Nastran proj.") are also shown and are much closer to those of the full Nastran model than its NLROM counterpart. This observation suggests that the largest

source of the discrepancy between NLROM and Nastran above the snap-through load originates from the coefficients of the model, not from the basis selection.

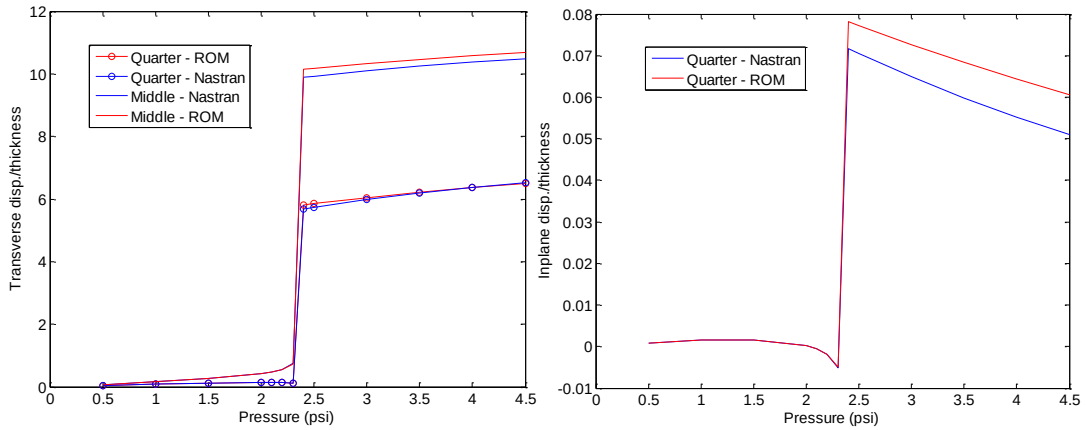

(a) (b)

Figure 28. Displacements vs. Uniform Load, Clamped-Clamped Cantilevered Beam. (a) Transverse Displacement at Beam Middle and Quarter Point, (b) In-Plane Displacement at Quarter Point.

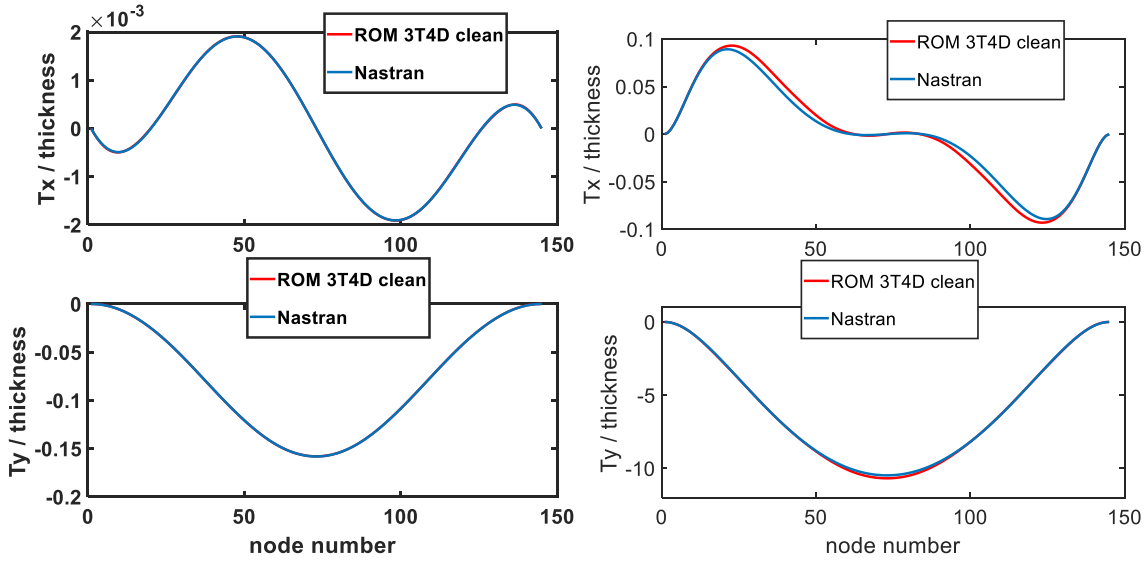

(a) (b)

Figure 29. In-Plane (Top) and Transverse (Bottom) Deformations of the Clamped-Clamped Curved Beam under a Uniform Load of (a) 1 lbs/in, (b) 4.5 lbs/in.

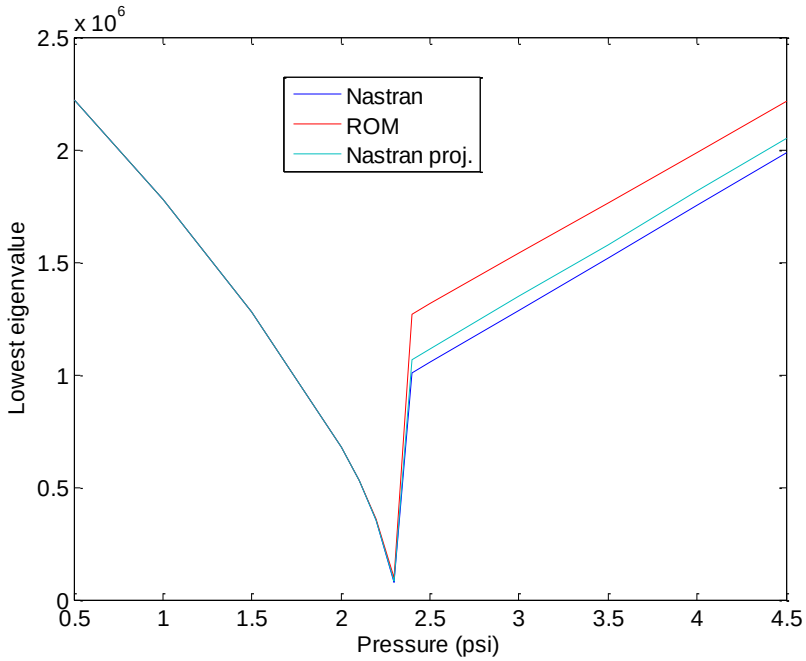

Figure 30. Lowest Eigenvalue of the Tangent Stiffness Matrix Corresponding to a Symmetric Eigenvector vs. Uniform Load Magnitude. Clamped-Clamped Curved Beam

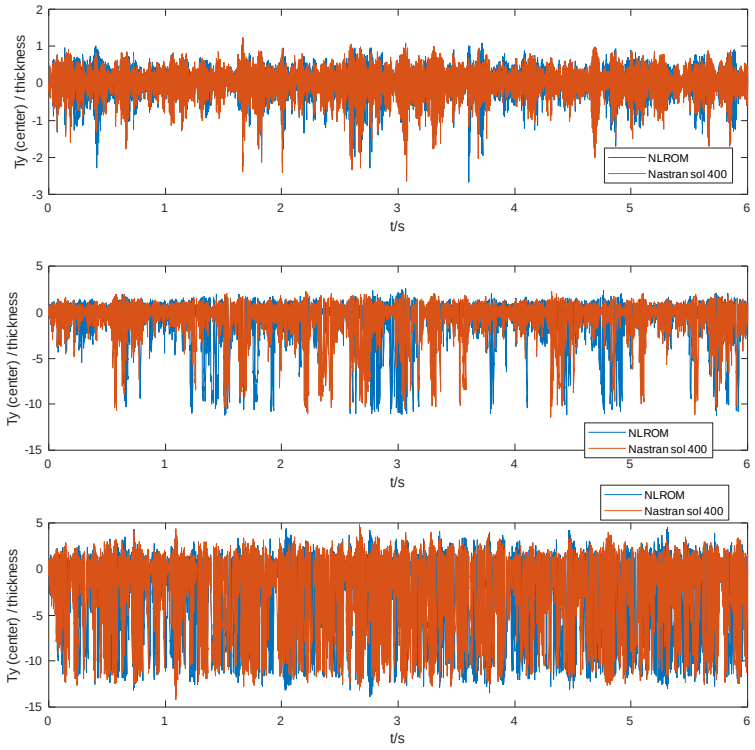

Figure 31. Time Histories of the Transverse Displacement of the Center of the Clamped-Clamped Beam under Low (Top), Medium (Middle), and High (Bottom) Acoustic Loadings.

A dynamic validation of this NLROM was also carried out, see Figure 31 and Figure 32 for time histories and power spectra density, under acoustic loads bandlimited in the [0,500]Hz frequency and of level ranging from low to medium to high for which the beam vibrates around the undeformed position, exhibits occasional snap-throughs, and regularly snap-through, respectively, see Figure 31. As shown in Figure 32, a good to very good match of the Nastran and NLROM power spectra was observed.

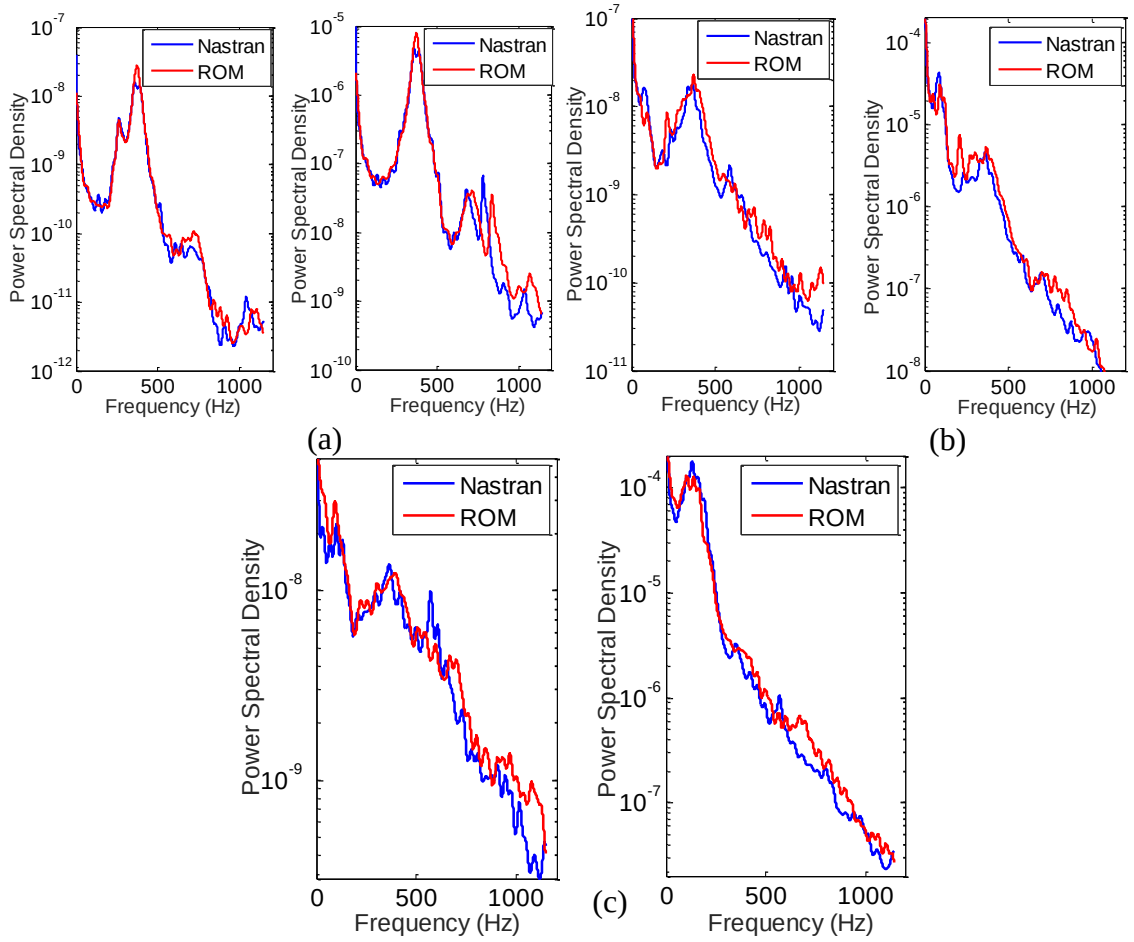

Figure 32. Power Spectral Densities of the In-Plane (Left) and Transverse (Right) Displacements at the Quarter Point of the Clamped-Clamped Beam under (a) Low, (b) Medium, and (c) High Loading.

6.2.3 Results after Tuning Based on Modal Force

One aspect which has not been touched in the above section and earlier efforts was the static snap-back of the model and more specifically whether the NLROM could also capture it well. To this end, static displacements under a set of uniform pressures in loading and unloading were determined from both Nastran and the NLROM. The loading phase went from loads of 0.1 lb/in to 4.5 lbs/in followed by unloading at the same pressures with an interval of 0.1 lb/in in both cases. Note that all NLROM results were obtained as the long-term response of dynamic computations performed using Newmark's algorithm with initial conditions corresponding to the converged solution at the prior load condition. The NLROM solutions obtained are thus all stable.

(a)

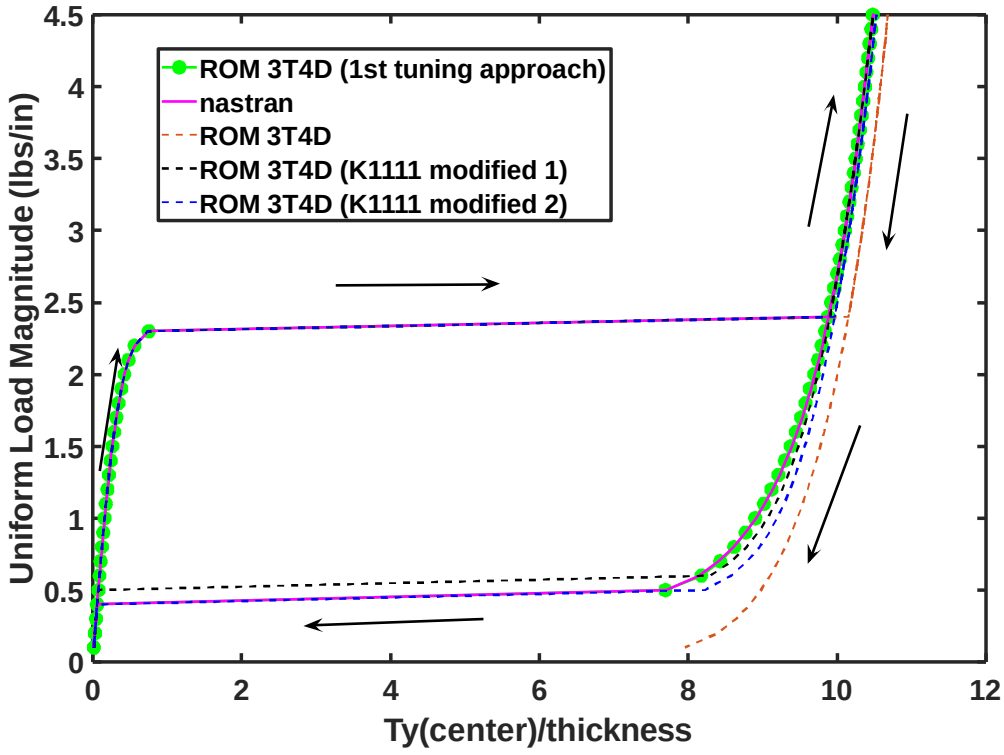

(b)

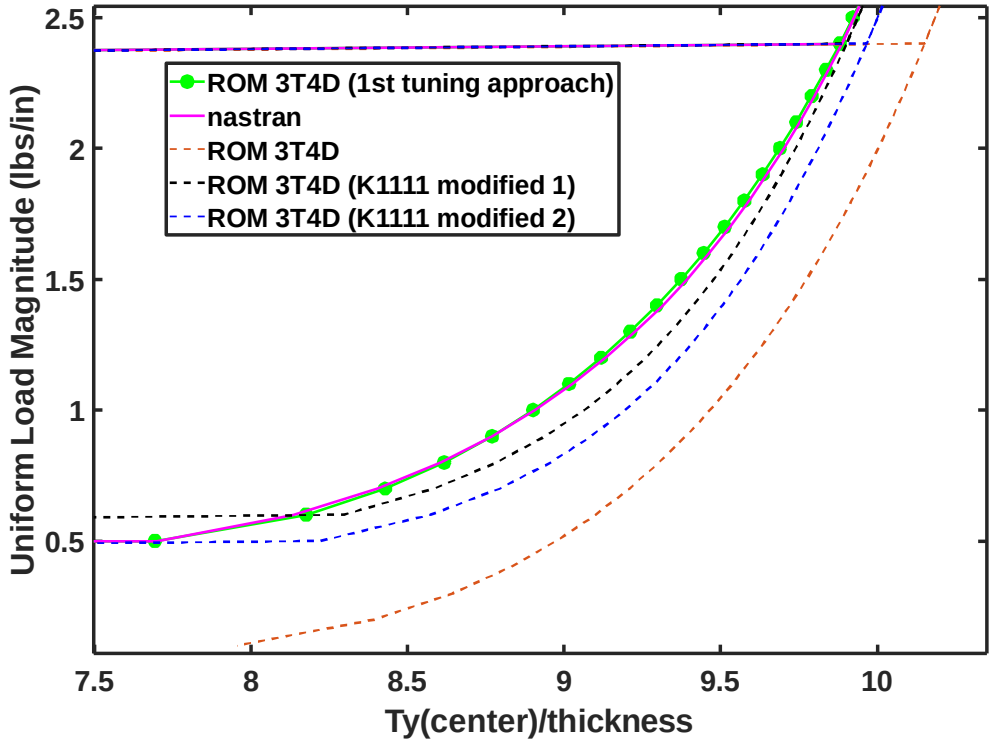

Figure 33. (a) Transverse Center Displacement vs. Uniform Load of the Clamped-Clamped Curved Beam Center Including Snap-Back. (b) Same as (a) Zoomed. Nastran and Various Versions of the 3T4D NLROM.

The results from these computations, shown in Figure 33, extend those shown in Figure 28(a). In particular, it is seen that the difference in predictions between Nastran and NLROM post snap-through remains as the beam is unloaded leading eventually to a snap-back load that is very small, much smaller than its Nastran counterpart, see Figure 33. Accordingly, some improvement of the model was sought.

The prediction error after snap-through is much larger than the representation error of the Nastran data by the basis. It was thus wondered whether the relatively poor matching of Figure 33(b) after snap-through could be attributed to just small inaccuracies of the identified coefficients. To this end, a sensitivity analysis was carried out in which each NLROM coefficient was varied by 5% one at a time and the prediction of the model at a post snap-through level recomputed. This effort demonstrated that:

i) the cubic stiffness coefficient of the first basis function $K_{1111}^{(3)}$ has by far the strongest effect on the response, especially on its in-plane component, and

ii) that there are many coefficients which have no significant effect on the response.

Point ii) suggested that some coefficients having no effect on the response could be eliminated which also support the form of the 'cleaned model'. Moreover, point i) suggested that very small changes in the leading cubic stiffness parameter $K_{1111}^{(3)}$ associated with the first transverse mode of the NLROM could have significant effects on the load vs. displacement curve. This is confirmed on Figure 33 where two additional NLROM predictions are also shown with values of $K_{1111}^{(3)}$ decreased by 0.2% ("K_{1111} modified 1")

and 0.3% ("K_{1111} modified 2"). An improvement of the unloading curve prediction and of the post snap-through behavior is clearly observed without any adverse effect on the loading branch.

The improvements obtained in Figure 33 by varying the parameter $K_{1111}^{(3)}$ demonstrate that a fine tuning of the NLROM parameters is indeed promising and thus the application of the approach of section 5 was undertaken. Note for the 3T4D basis and before snap-through that the prediction is very good and the representation errors (transverse and in-plane) are very small. After snap-through, the representation error is between 0.07%-0.09% in the transverse direction and 0.4%-1.2% in the in-plane direction. These errors were deemed small enough to apply the formal fine-tuning approach using Nastran data from the uniform loadings of 2.3 lbs/in, 2.4 lbs/in, 4.5 lbs/in all three in the loading branch and 0.5 lb/in in the unloading branch. Moreover, since the prediction of the response before snap-through is excellent, it was decided to only tune the cubic stiffness coefficients which play a small role then but a much bigger one after snap-through. Note that all cubic coefficients were tuned here even those that relate to the duals and which were zeroed out in the cleaned model the results of which were presented in the previous section.

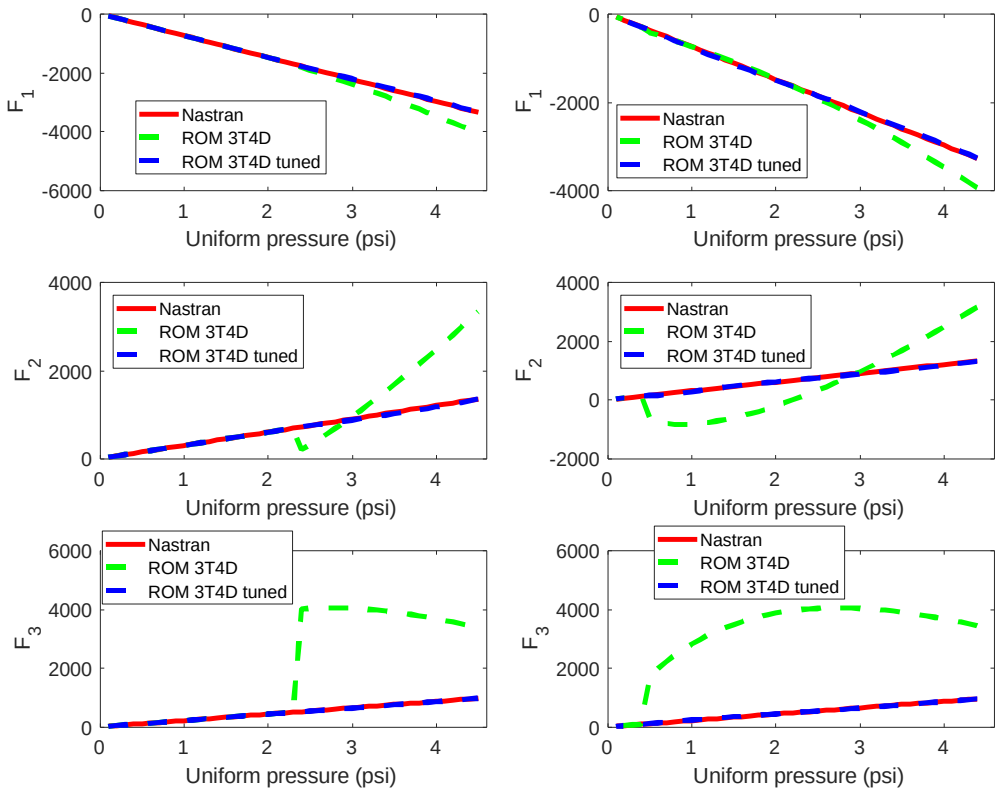

Figure 34 Nastran and ROM Predicted Modal Forces, before and after Tuning, Modal Forces Along Modes 1 (Top), 2 (Middle), and 3 (Bottom). Loading (Left) and Unloading (Right) Branches.

As shown in Figure 34 the original model did not, surprisingly, capture very well the modal forces along the transverse modes 1, 2, and 3. However, after applying the tuning of Eq. (60) a sharp improvement is observed, and the Nastran and NLROM modal forces are indistinguishable from each other. More importantly, the improvement in the modal force matching is reflected in the load vs. center displacement curve, see Figure 33 which now agrees with the Nastran one nearly exactly through the entire cycle of loading. The improvement is also visible at other points of the beam as seen in Figure 35 where the tuned NLROM response now perfectly matches the Nastran predictions.

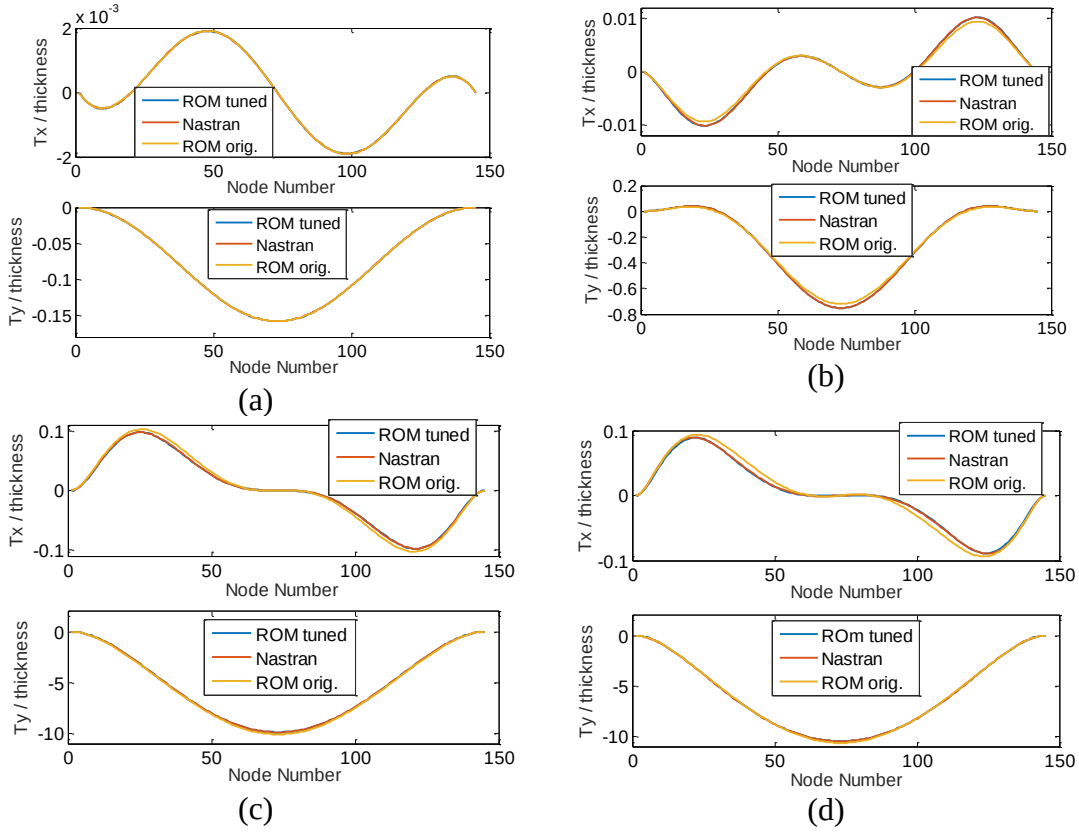

Figure 35. In-Plane (Top) and Transverse (Bottom) Deformations of the Clamped-Clamped Beam at 0F under a Uniform Load of (a) 1 lb/in (b) 2.3 lb/in, (c) 2.4 lb/in, and (d) 4.5 lb/in. Nastran, 3T4D NLROM before Tuning ("ROM orig.") and after Turning ("ROM Tuned").

In view of the results obtained in Figure 33-Figure 35, the tuned NLROM was adopted at 0F and its accuracy at 50F and 150F was assessed next. Unfortunately, it was found that the model is unstable at these temperatures. To better understand the issue, the accuracy of the basis to represent the Nastran data at these temperatures was assessed. Shown in Figure 36 are the average representation errors of the 3T4D basis for displacements post snap-through at 0F, 50F, and 150F. It is seen that these errors are larger at 50F and 150F than at 0F, although not dramatically.

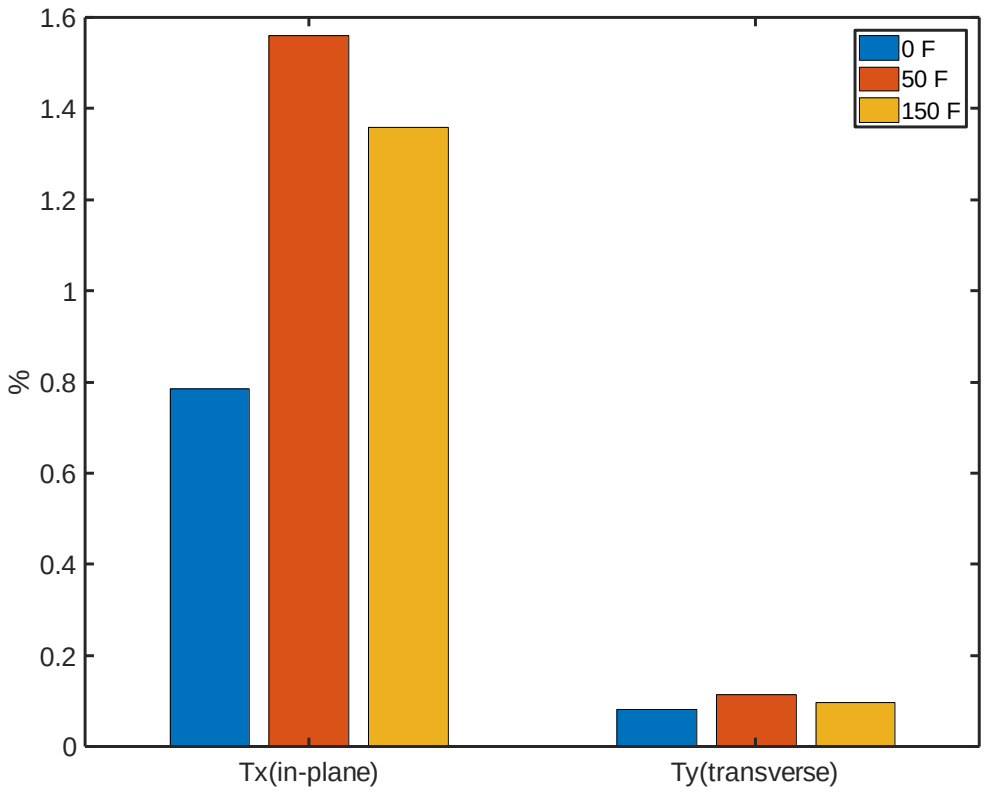

Figure 36. Average Representation Errors, In-Plane and Transverse, of the 3T4D Basis for Post Snap-Through Displacements at 0F, 50F, and 150F.

Another metric of the appropriateness of the basis is the matching of the eigenvalues of the tangent stiffness matrix from Nastran and from the projection of that matrix on the basis. This comparison is achieved on Figure 37 for the three temperatures and the first two eigenvalues, expanding the results of Figure 30. These results confirm those of Figure 30 and more clearly demonstrate that the 3T4D basis is not sufficient to provide a good match of the Nastran results at 50F and 150F.

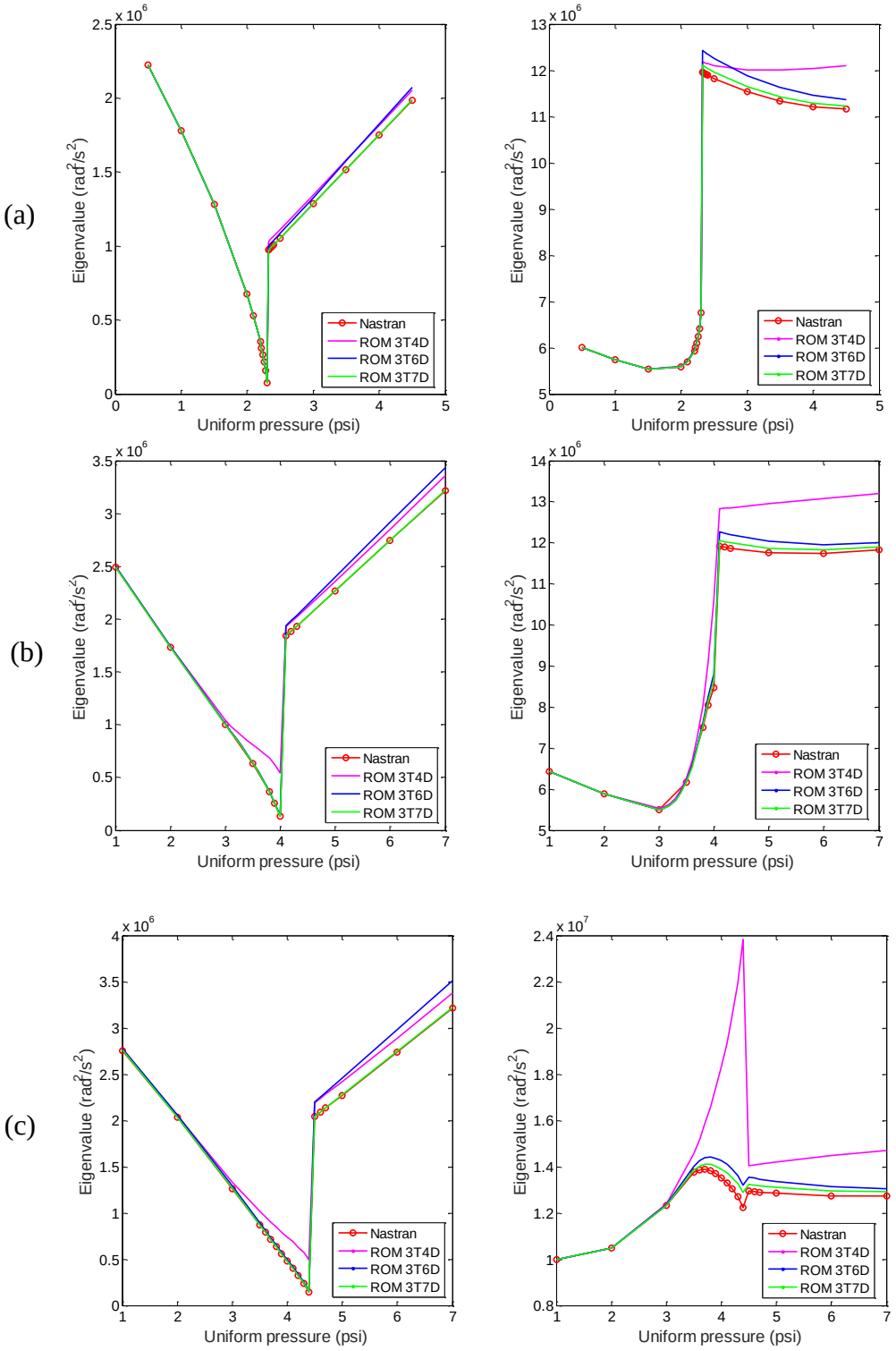

Figure 37. First (Left) and Second (Right) Lowest Eigenvalues of the Tangent Stiffness Matrix from Nastran and Projected on the 3T4D, 3T6D, and 3T7D Bases for (a) 0F, (b) 50F, (c) 150F.

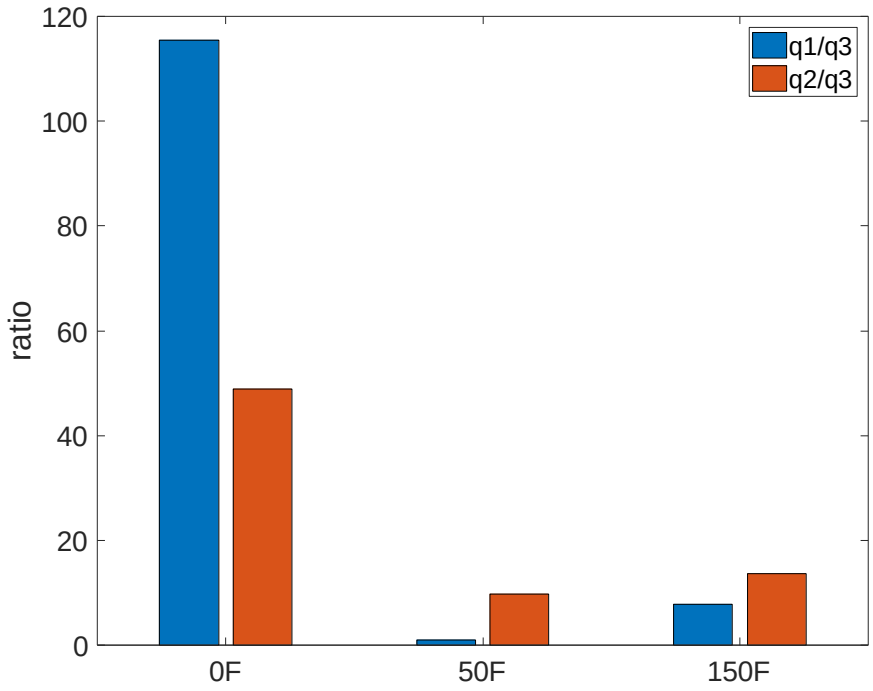

Figure 38. Ratio of Projection Coefficients of the Nastran Deflection Right before Snap-Through at Different Temperatures on the 3 Transverse Modes (Absolute Value).

Table 8. Projection Coefficients of the Nastran Deflection Right before Snap-Through at Different Temperatures on the 3 Transverse Modes.

	0F	50F	150F
q_1	-6.5 10-4	-1.3 10-4	1.1 10-3
q_2	-2.7 10-4	1.3 10-3	1.9 10-3
q_3	5.6 10-6	-1.3 10-4	-1.4 10-4

In fact, these results suggest that a change in the response near/post snap-through occurs at 50F or 150F. To understand better this change, the deflections of the beam right before snap-through at these three temperatures were analyzed. As shown in Figure 38 and Table 8, that deflection changes very significantly with temperature: while it is dominated at 0F by the first mode, then the second with little contribution from the third, this last

mode is much more important at 50F and the second mode dominates. At 150F, the situation has somewhat reverted and the second mode is dominant.

The above findings suggest that dual modes with modes 2 and 3 dominant should be present to properly capture the in-plane component of the deformations. A revisit of the dual modes selection was accordingly performed with modes 1, 2, and 3 potentially dominant. There were 6 dual modes taken, three from the combination 1-1, and one each from the combinations 1-2, 2-3, and 3-3, leading to a 3T6D model.

The projection of the Nastran tangent stiffness matrices on this new basis was carried out and the computation of the corresponding eigenvalues confirm the benefit of the additional 2 dual modes. As seen in Figure 37, the matching with Nastran just before and at snap-through at 50F and 150F is significantly improved. Yet, it may also be observed that the eigenvalues post snap-through do not match very well their Nastran counterparts. To resolve this last issue, the eigenvectors associated with the lowest eigenvalue of the Nastran tangent stiffness matrix at 0F under the entire set of uniform pressure considered (from 1 lb/in to 7 lbs/in) were extracted, then projected on the 3T6D basis. Finally, the residuals of projection were assembled in a proper orthogonal decomposition format and the leading eigenvector of this analysis was retained to complement the basis, transforming it into a 3T7D model. Note that the above process has created at 0F a NLROM basis representing well the response of the curved beam under various temperatures. Such an effort is in contrast with the strategy developed in connection with other temperature loading scenarios, e.g. see [29,31,41], in which the “cold” basis, i.e., the 3T4D here, is

enriched by additional basis functions to capture well the deflections induced by a non zero temperature.

As seen in Figure 37, the addition of this 10th mode to the basis leads to a significant improvement of the matching of the lowest 2 eigenvalues of the tangent stiffness matrix at all 3 temperatures. The average representation error of the Nastran data post snap-through was also found to be very low, see Figure 39, strongly suggesting that the basis is now appropriate for the prediction of the response at the 3 temperature levels.

The NLROM parameters of this new model were identified by the multiple level method of [17] and the tuning process described in connection with the 3T4D model was repeated with data from the uniform pressures of 2.4 lbs/in, 4.5 lbs/in and 0.5lb/in at 0F, which are right after snap-through, maximum loading and right before snap-back, as well as uniform pressures of 4 psi, 4.1 lbs/in and 0.3 lbs/in at 50F, which are right before, right after snap-through, right before snap-back. Then, shown in Figure 40, are the load vs. center displacement of the beam predicted by this NLROM as compared to Nastran for 0F, 50F, and 150F. While the predictions match nearly exactly Nastran at 0F, there is a slight difference in the snap-through load at 50F and both snap-through and snap-back at 150F This situation likely results from tuning having been carried out on data at 0F. Note finally that the 3T7D model did not converge after snap-through before tuning, even cleaned.

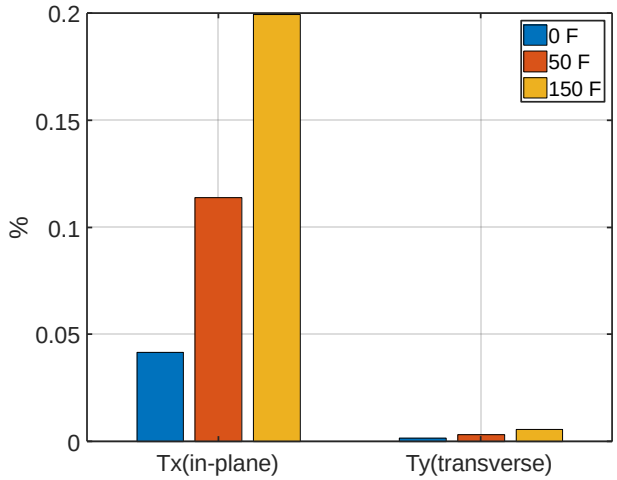

Figure 39. Average Representation Errors, In-Plane and Transverse, of the 3T7D Basis for Post Snap-Through Displacements at 0F, 50F, and 150F.

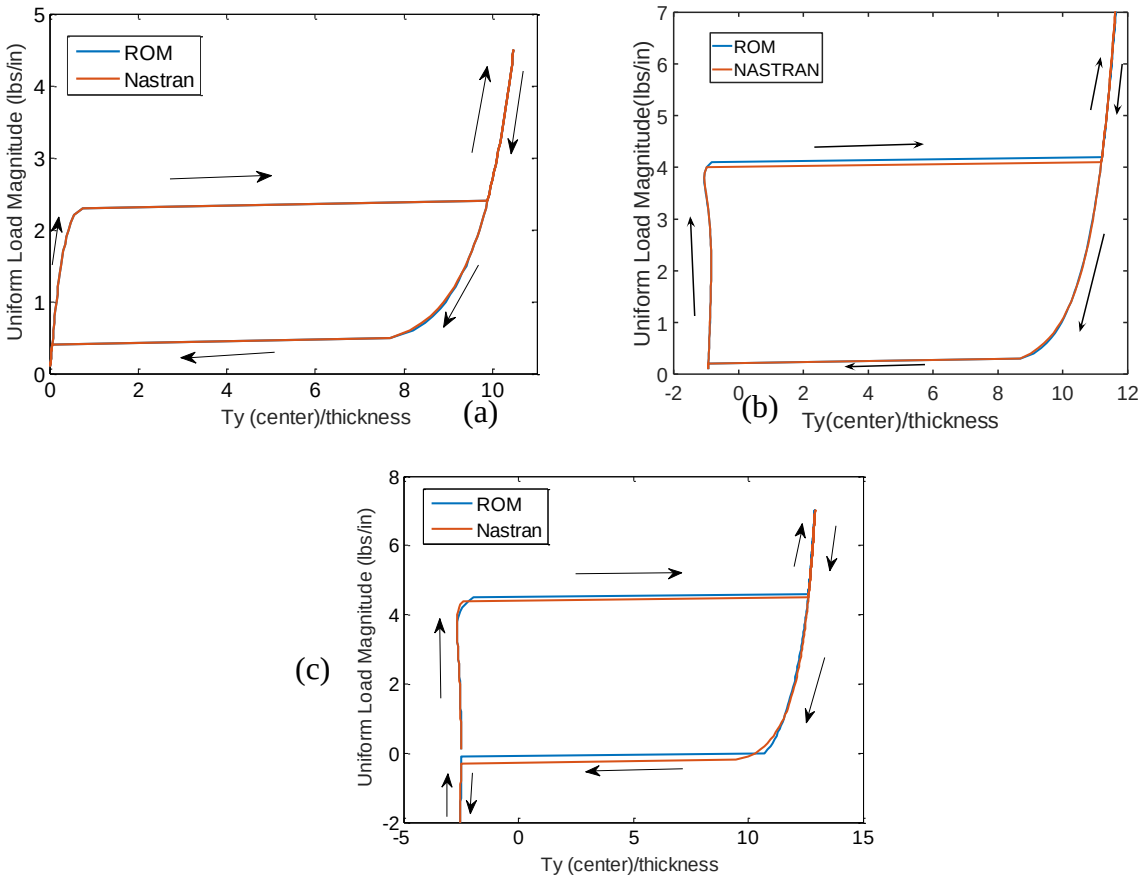

Figure 40. Transverse Displacement of the Beam Center vs. Uniform Load of the Clamped-Clamped Curved Beam Center including Snap-Back. (a) 0F, (b) 50F, (c) 150F. Nastran and 3T7D NLROM after Tuning.

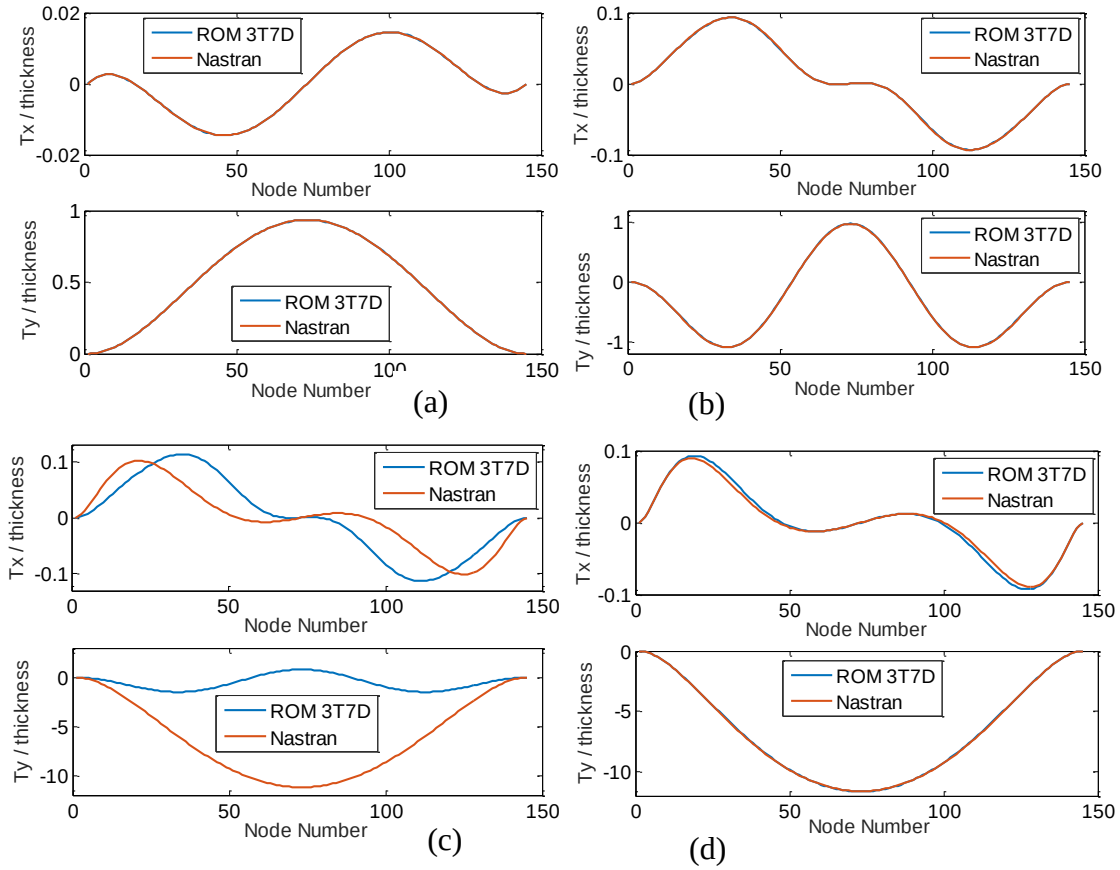

Figure 41. In-Plane (Top) and Transverse (Bottom) Deformations of the Clamped-Clamped Curved Beam at 50F under a Uniform Load of (a) 0.1 lb/in, (b) 4 lbs/in, (c) 4.1 lbs/in, And (d) 7 lbs/in. Nastran and 3T7D NLROM after Tuning.

Moreover, shown in Figure 41 and Figure 42 are the deflections predicted by the model under different loads under the temperatures of 50F and 150F. At 50F, an excellent matching between Nastran and the NLROM is again observed before snap-through. Post snap-through, see Fig. 31(d), the agreement is very good. However, just after the Nastran predicted snap-through, see Fig 31(c), there is a significant difference between Nastran and the NLROM predictions, but this is due to the small difference in the snap-through load. For that load condition, Nastran predicts that beam has snapped-through while the NLROM still predicts it on the main branch. At 150F, the predictions are slightly in error at 4.2 lbs/in,

as can also be seen on Figure 42(c), but also at the highest load level of 7 lbs/in but the accuracy is nevertheless very good.

An assessment of the 3T7D NLROM under dynamic loading was also undertaken. At 0F, when the excitation is low or medium, there is some improvements in the predictions as compared with the 3T4D model, see Figure 43. Unfortunately, the 3T7D NLROM is unstable at the high excitation level. When the temperature is increased to 50F or 150F, the NLROM is unstable under all dynamic loadings.

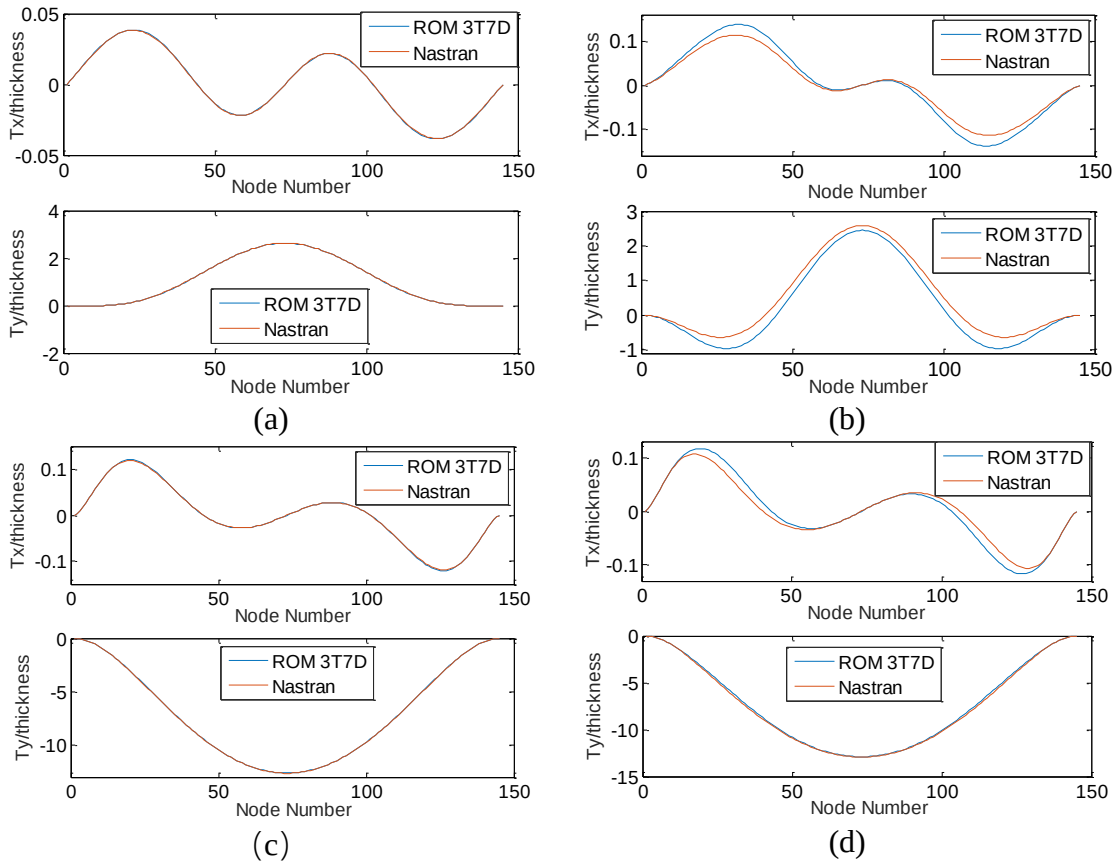

Figure 42. In-Plane (Top) and Transverse (Bottom) Deformations of the Clamped-Clamped Curved Beam at 150F under a Uniform Load of (a) 3 lbs/in, (b) 4.2 lbs/in, (c) 4.6 lbs/in, and (d) 7 lbs/in. Nastran and 3T7D NLROM after Tuning.

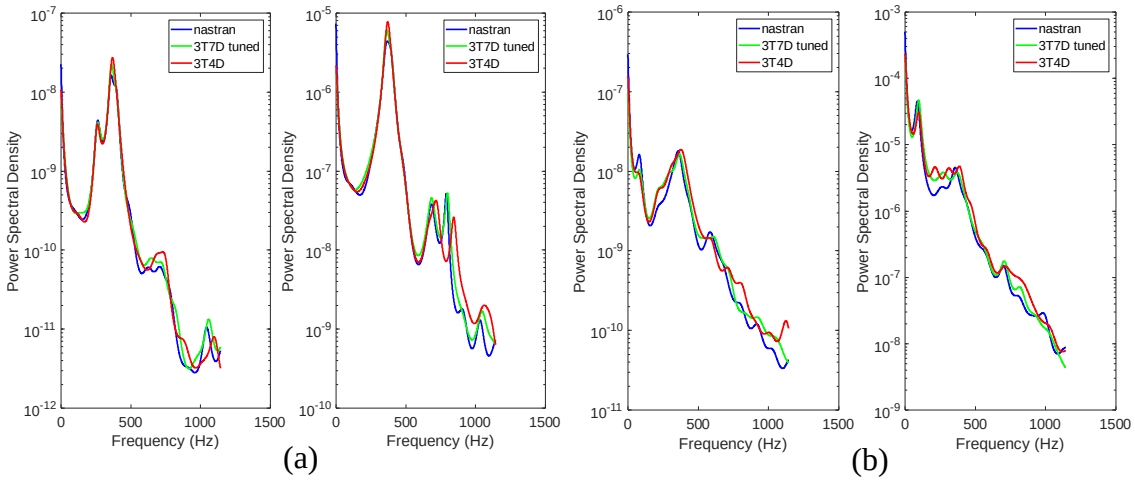

Figure 43. Power Spectral Densities of the In-Plane (Left) and Transverse (Right) Displacements at the Quarter Point of the Clamped-Clamped Beam under (a) Low, (b) Medium Loading. Nastran and 3T7D NLROM before and after ("tuned") Tuning.

The modal force based tuning process was also performed on another NLROM of basis 3T5D obtained by keeping the first 3 transverse modes and the first 5 duals of the 6T8D basis, see Figure 11and Figure 44 for some results obtained before tuning with the cleaned model identified at a single level. This model exhibits optimized transverse modes but regular duals. The modal force tuning was performed as for the other two models by starting from the cleaned model and tuning all cubic stiffness terms. This process led to the loading-unloading curve shown in Figure 44 which provides a very close match of its Nastran counterpart except in the direct neighborhood of the snap-back position.

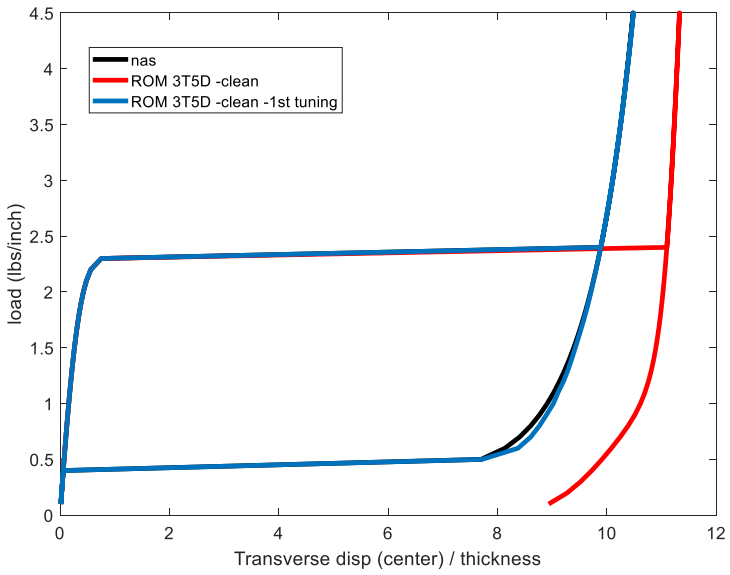

Figure 44. Transverse Displacement of the Beam Center under Uniform Load Predicted by Nastran, the Cleaned 3T5D NLROM Before Tuning ("clean"), and the 3T5D NLROM after Tuning ("clean-tuning").

6.2.4 Results after Tuning Based on Generalized Coordinates

The tuning based on the generalized coordinates was performed a bit differently from the modal force one carried out in the previous section. Specifically, it also started from the cleaned model but to it were added stiffness coefficients that involve the grouping *td* such ass $K^{(2)}_{ttd}$ (already included, kept as it), $K^{(2)}_{dtd}$, $K^{(3)}_{tttd}$, $K^{(3)}_{ttdd}$ and their companions (those related by the super symmetry relations) $K^{(2)}_{dtt}$ (already included, kept as it), $K^{(2)}_{tdd}$, $K^{(3)}_{dttt}$, and $K^{(3)}_{dttd}$ for a series of transverse and dual modes

Before performing the optimization, the cleaned model was rendered super symmetric by averaging the coefficients which should be equal. Moreover, the optimization of E was performed under the constraints that the cleaned coefficients to

identify also satisfied the super symmetry relations. This constraint first reduces the number of coefficients to be identified but it also guarantees that the elastic forces are associated with a potential thereby reducing the potential for spurious energy input/dissipation. This tuning was accomplished without weight on the coefficients, $w^{(2)}$, and the loading cases were selected as static uniform pressures of 2.4lbs/in and 4.5lbs/in in the loading direction and 0.7lbs/in in unloading. This effort was carried out for the 3T5D, 3T7D, and 6T8D models discussed in the previous sections but also for a 6L7D model formed by the first 6 symmetric linear modes of the curved beam and 7 duals from the 21 combinations of the 6 modes that reduce the most the in-plane error. This latter model is interesting to consider here because it is constructed without any prior knowledge of the beam response, i.e., without any basis optimization. Its stiffness coefficients were identified from the multiple level approach. The set of coefficients which were tuned involved all transverse and dual modes for the 3T5D model but only the first 4 transverse and 4 duals for the 6T8D one. For the 3T7D model, the process involved all transverse modes but only the first 3 duals while all linear modes and the first 5 duals only were considered for the 6L7D model. Validations under different types of loads were performed and are discussed next.

6.2.4.1 Under Uniform Static Load

Shown in Figure 45(a) are the loading-unloading curve corresponding to the transverse displacement of the middle of the beam under uniform load, as predicted from Nastran, the two cleaned NLROMs (3T5D and 6L7D), as well as their corresponding extended models (including the clean coefficients and those identified, referred to as

"clean-tuned" in the figures). The matching of the Nastran curve by the latter models is clearly excellent in both loading and unloading at the contrary of the cleaned models before tuning which capture it well before snap-through but poorly predict the post snap-through behavior. A similar comparison is shown in Figure 45(b) for the 3T7D and 6T8D models which shows again very good to excellent matching with the Nastran data. Note that neither of these two models converged post snap-through before tuning.

To complement the above analysis of the center displacement, shown in Figure 46 and Figure 47 are the deformations, transverse (vertical) and in-plane (horizontal) of the beam at the two loadings of 1lb/in and 4.5lbs/in. The first one is well below the snap-through threshold and good predictions are obtained with all 4 models and in both directions. The tuning did not worsen the matching. At the higher loading however, the cleaned models are clearly significantly in error but the extended ones match the Nastran predictions nearly perfectly.

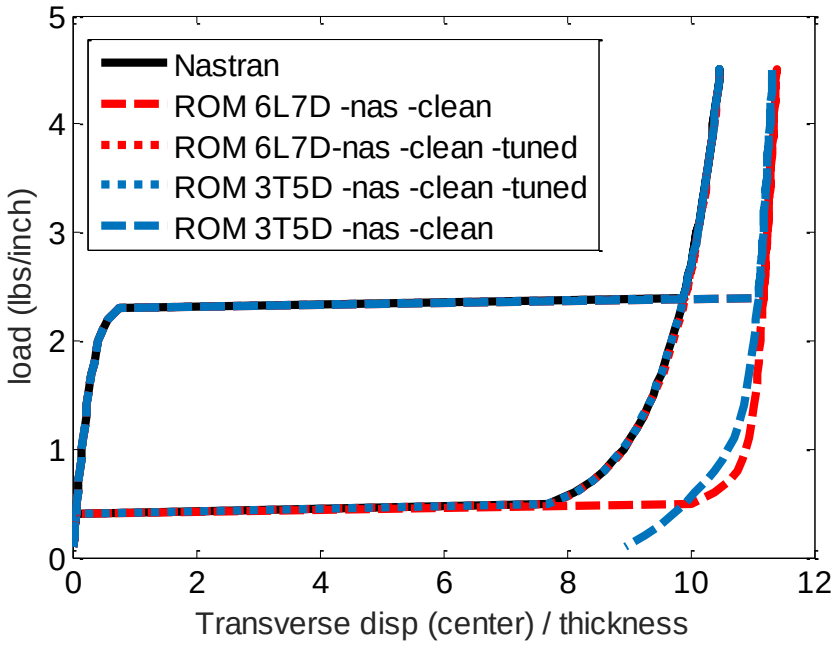

(a)

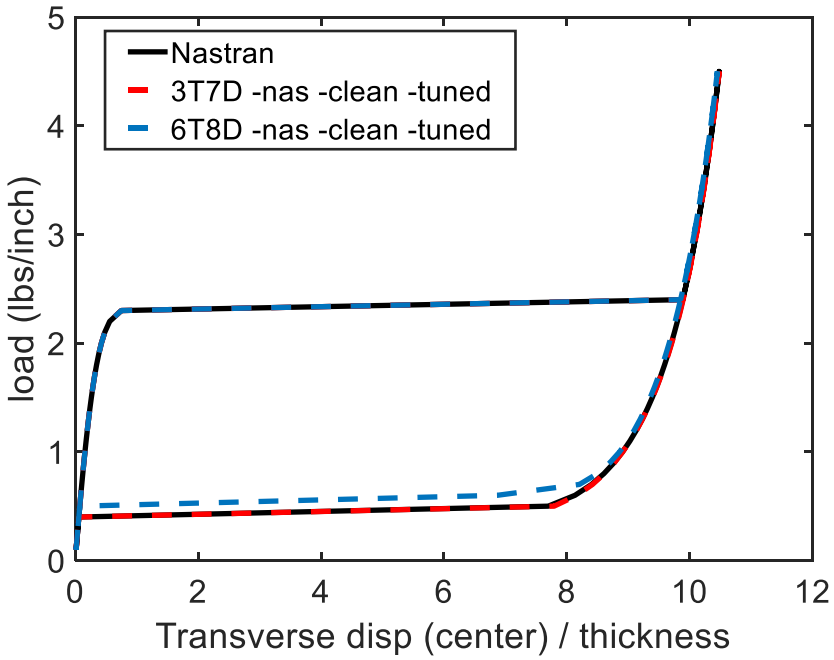

(b)

Figure 45. Transverse Displacement of the Beam Center under Uniform Load Predicted by (a) Nastran, the Cleaned 3T5D and 6L7D NlROMs, and the Corresponding Extended ("clean-tuned") Models with the Identified Coefficients. (b)Same as (a) but Tuned 3T7D and 6T8D NLROMs

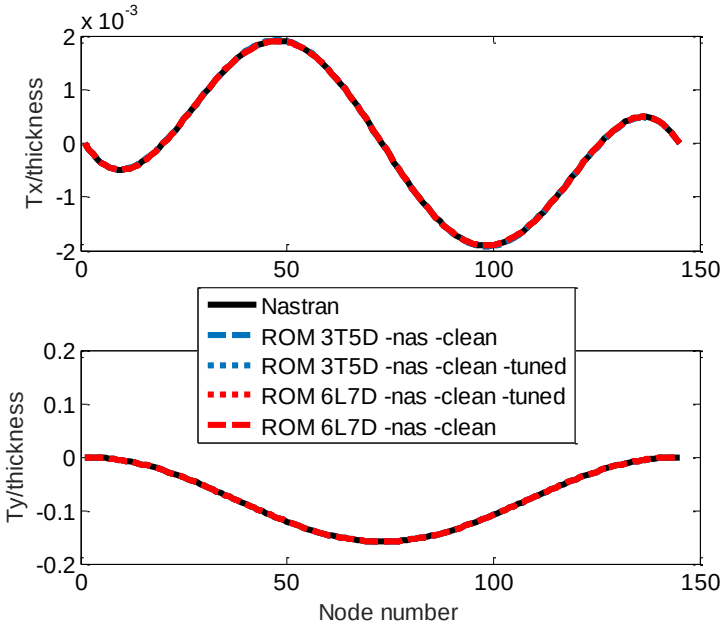

Figure 46. In-plane/Horizontal (Top) and Transverse/Vertical (Bottom) Displacements of the Clamped-Clamped Curved Beam under a Uniform Pressure of 1lbs/in. Nastran, Cleaned and Extended ("clean-tuned") 3T5D and 6L7D NLROMS.

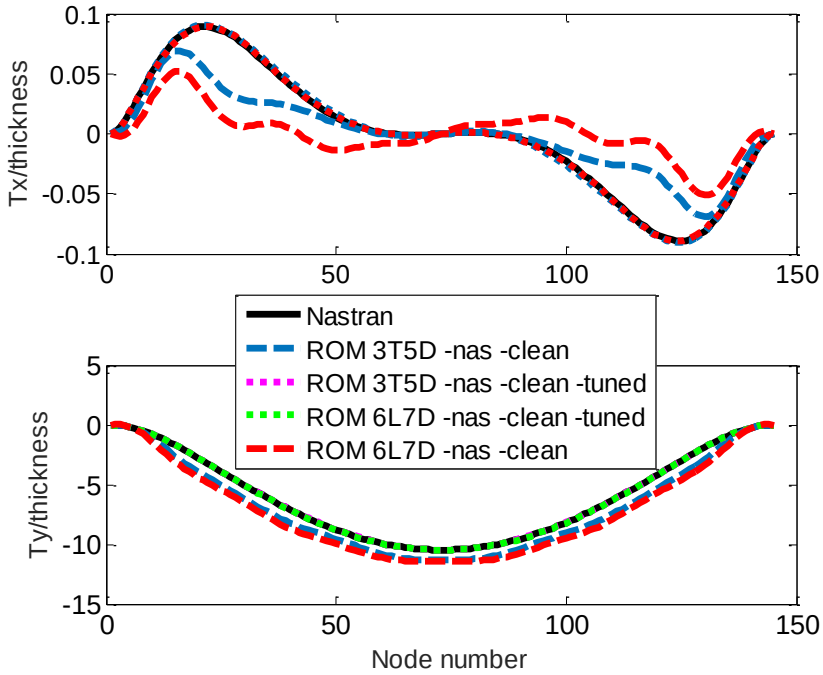

Figure 47. In-plane/Horizontal (Top) and Transverse/Vertical (Bottom) Displacements of the Clamped-Clamped Curved Beam under a Uniform Pressure of 4.5lbs/in. Nastran, Cleaned and Extended ("clean-tuned") 3T5D and 6L7D NLROMs.

It was also of interest to assess the static response of the above tuned 3T5D NLROM with temperature and shown in Figure 48 are the loading-unloading predictions at 50F and 150F. Even though the 3T5D basis does not have a low representation error of these static responses, especially at 150F, the predictions are quite good at 50F and reasonable at 150F, and all stable at both temperatures.

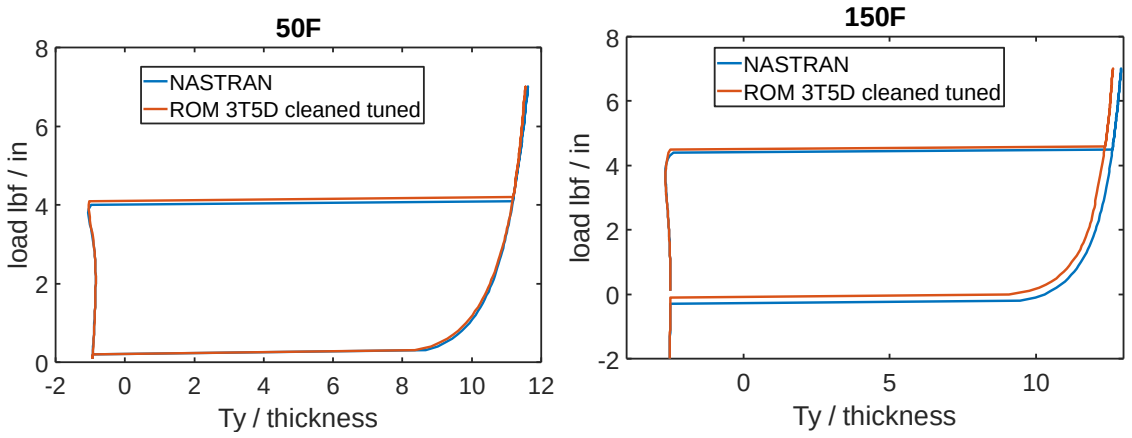

(a) (b)

Figure 48. Transverse Displacement of Beam Center vs. Uniform Load including Snap-Back at (a) 50F, (b) 150F. Nastran and Extended ("cleaned-tuned") 3T5D NLROM.

6.2.4.2 Under Absolute Sinusoidal Load

The previous results focused on loading cases that are similar to those used for identification, i.e., a uniform load. It could thus be questioned whether the extended NLROMs are applicable only to this loading or are genuinely models of the curved beam and thus applicable to other loadings as well. To assess this applicability, pressure loadings in the form of the absolute value of a sine function with period matching the length of the beam were applied to the beam. The shape of loading is shown in Figure 49. Maximum

value occurs at the two quarter points of the beam and the load at the center of the beam is zero.

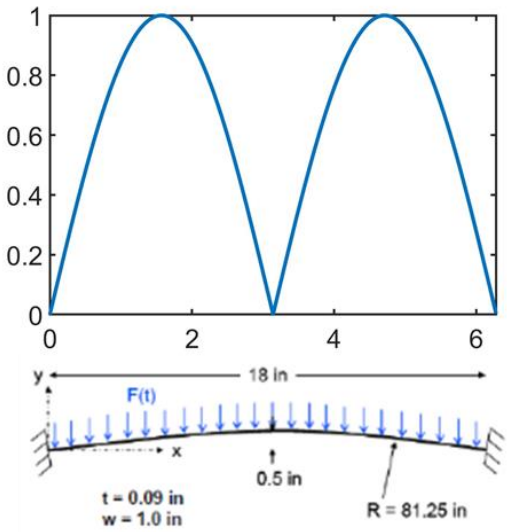

Figure 49. Shape of Absolute Sine Load.

Then, shown in Figure 50 - Figure 54 are the loading curve corresponding to the transverse displacement of the middle of the beam and the deformations, transverse (vertical) and in-plane (horizontal) of the beam at two loadings, one below the snap-through threshold and the other above it. These results are consistent with those from the uniform loading: the predictions from the extended models constructed from uniform loading (i.e., as above) almost perfectly match the Nastran full finite element results while those from the cleaned models are only good below snap-through, even for the modal force tuned model, see Figure 54.

These results demonstrate that the loadings used for the identification do not need to be similar to those used in the ensuing prediction and thus genuine NLROMs are obtained as part of the identification.

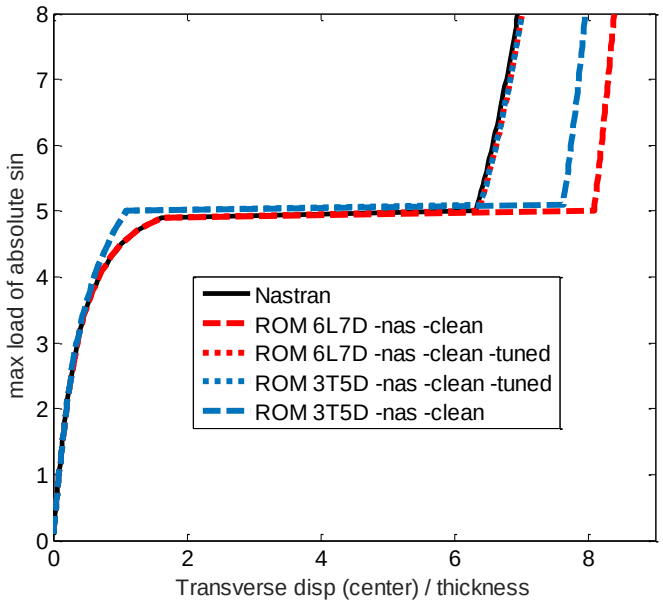

Figure 50. Transverse Displacement of the Beam Center under an Absolute Value of Sine Loading Predicted by Nastran, the Cleaned 3T5D and 6L7D NLROMs, and the Corresponding Extended ("clean-tuned") Models with the Identified Coefficients.

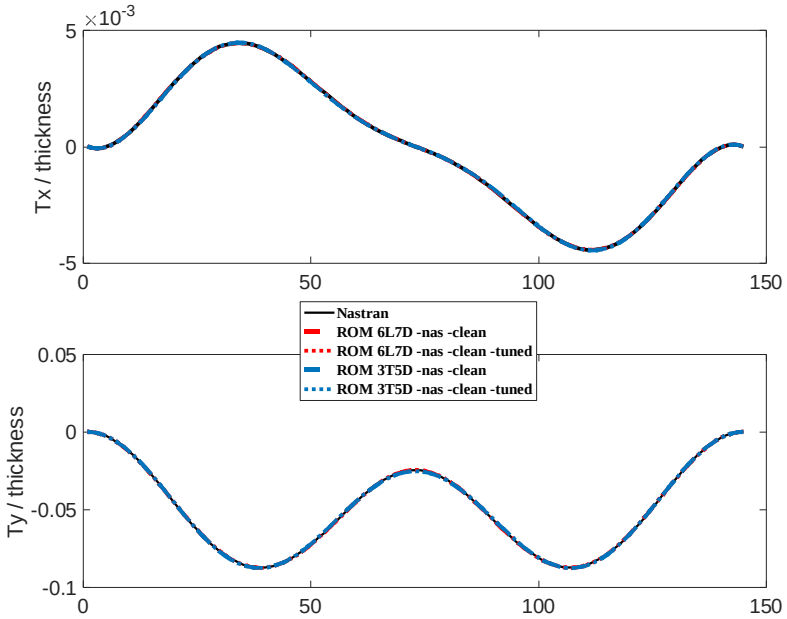

Figure 51. In-plane/Horizontal (Top) and Transverse/Vertical (Bottom) Displacements of the Clamped-Clamped Curved Beam under an Absolute Value of Sine Loading with Peak Pressure of 1lb/in. Nastran, Cleaned and Extended ("clean-tuned") 3T5D and 6L7D NLROMs.

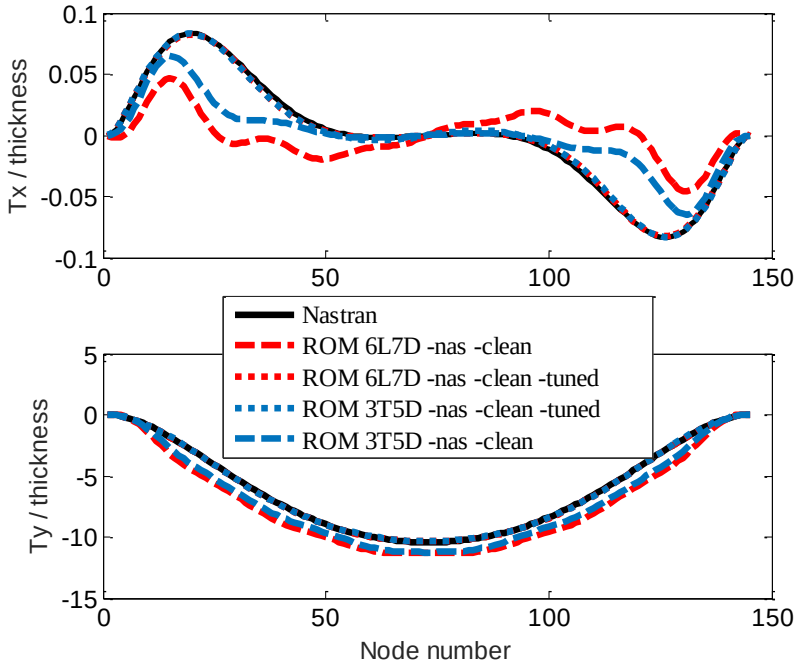

Figure 52. In-plane/Horizontal (Top) and Transverse/Vertical (Bottom) Displacements of the Clamped-Clamped Curved Beam under an Absolute Value of Sine Loading with Peak Pressure of 7lbs/in. Nastran, Cleaned and Extended ("clean-tuned") 3T5D and 6L7D NLROMs.

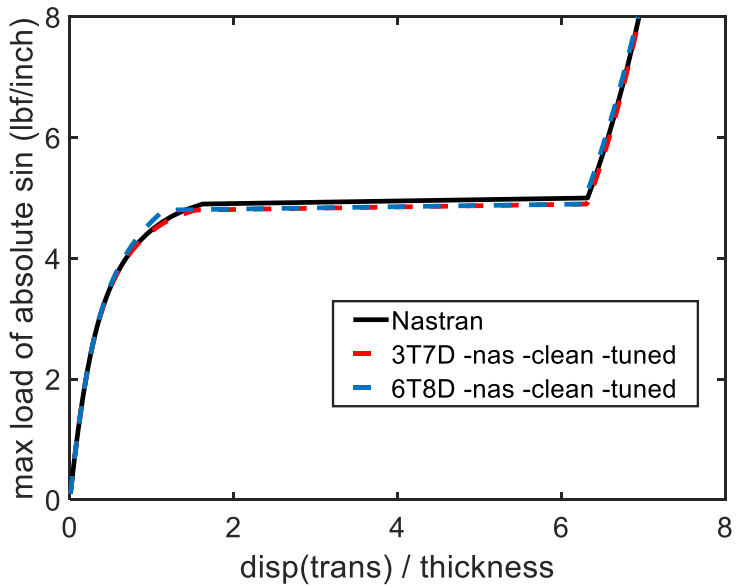

Figure 53. Transverse Displacement of the Beam Center under an Absolute Value of Sine Loading Predicted by Nastran, the Extended (”clean-tuned”) 3T7D and 6T78D NLROMs.

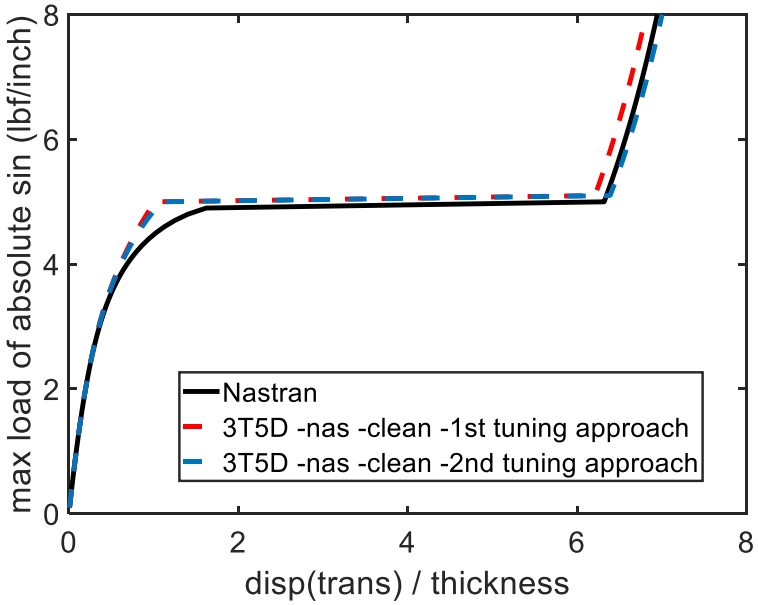

Figure 54. Transverse Displacement of the Beam Center under an Absolute Value of Sine Loading Predicted by Nastran, Extended (Cleaned and Tuned from the Modal Force (“1st”) and Generalized Coordinates (“2nd”) Tuning) 3T5D NLROM.

6.2.4.3 Under Dynamic Load

The extended NLROMs were also tested in a dynamic setting under acoustic loads bandlimited in the [0,500] Hz frequency and of levels ranging from low to medium to high for which the beam vibrates around the undeformed position, exhibits occasional snap-throughs, and regularly snap-through, respectively. Then, shown in Figure 55-Figure 56 are the power spectral densities of the transverse and in-plane displacement of the node located at the quarter point of the beam for the full finite element model and the 3T5D and 6L7D cleaned and extended NLROMs. While the predictions of the cleaned models are fairly good, it is seen that the extended models capture better the Nastran features, e.g., the low frequency peak in Figure 55(b) and Figure 56.

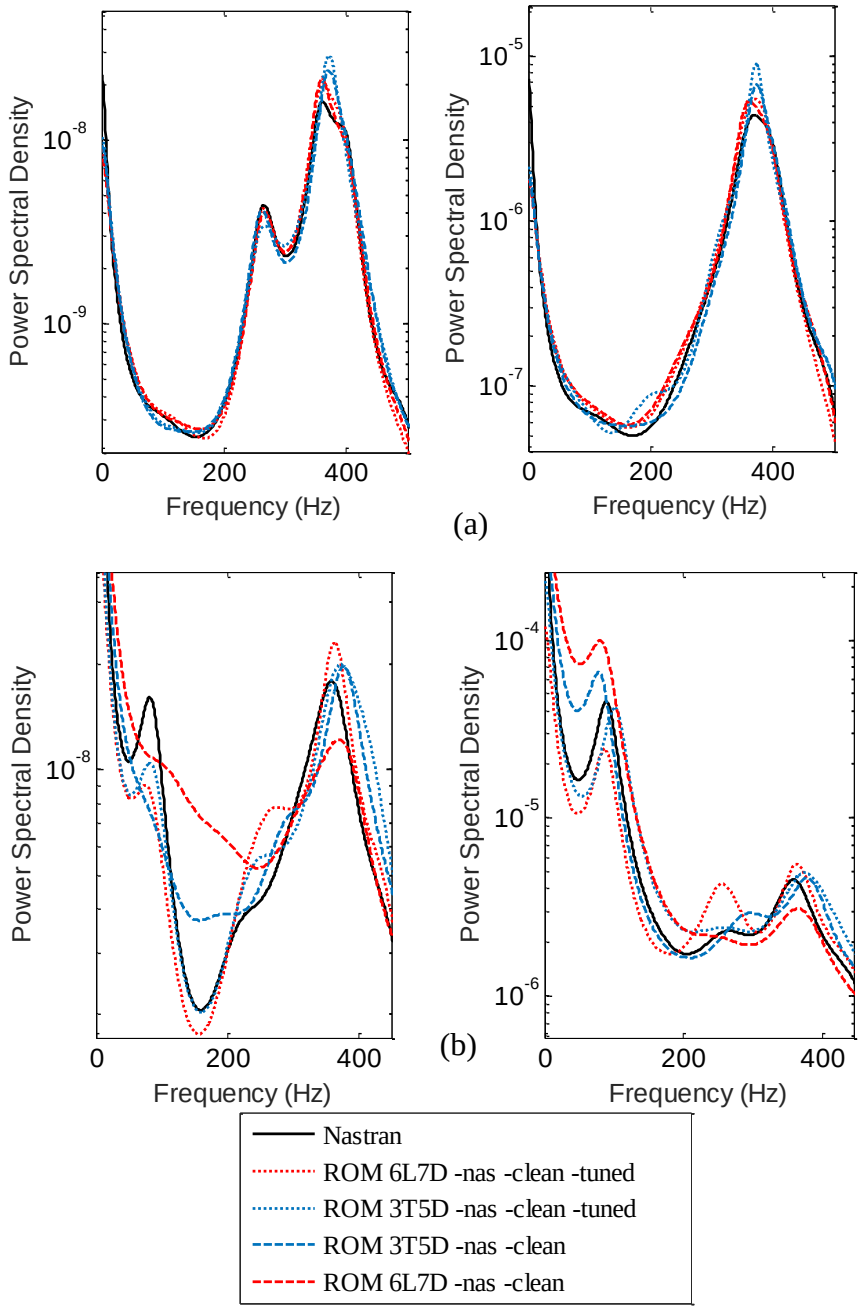

Figure 55. Power Spectral Densities of the In-plane (Left) and Transverse (Right) Displacements at the Quarter Point of the Clamped-Clamped Beam under (a) Low and (b) Medium Acoustic Loading. Predictions from Nastran Finite Element, and Cleaned and Extended ("clean-tuned") 3T5D and 6L7D NlLROMs.

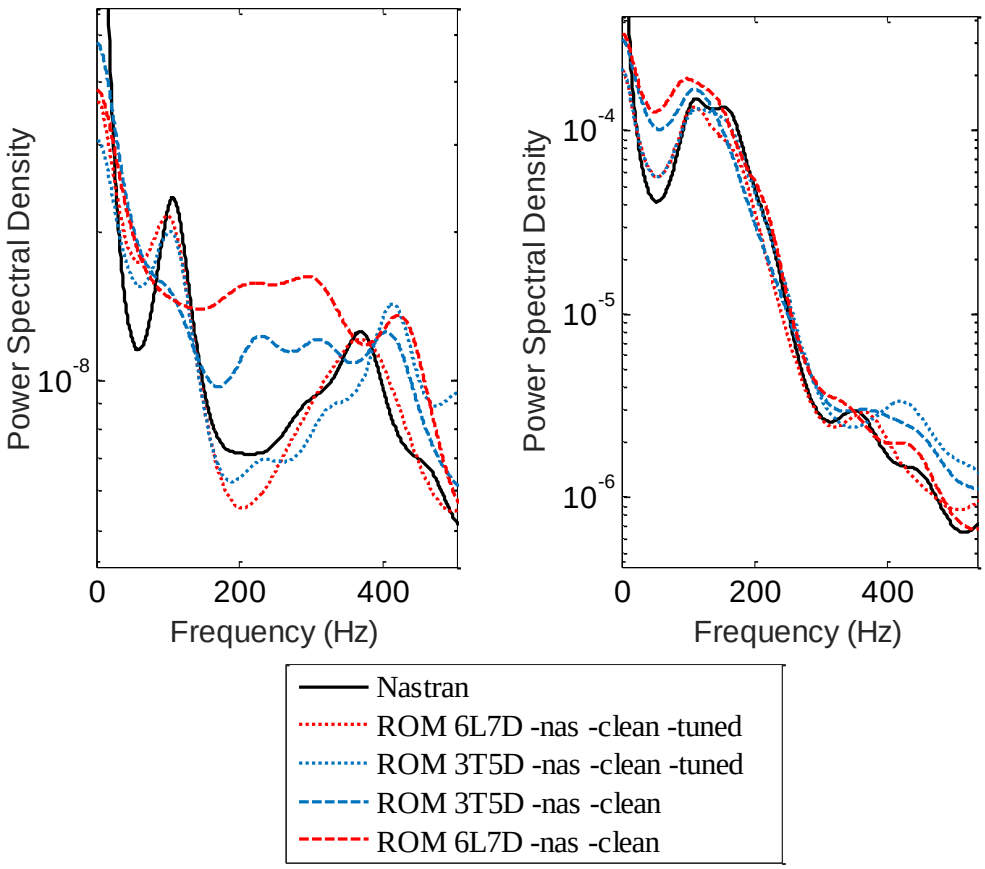

Figure 56. Power Spectral Densities of the In-plane (Left) and Transverse (Right) Displacements at the Quarter Point of the Clamped-Clamped Beam under High Acoustic Loading. Predictions from Nastran Finite Element, and Cleaned and Extended ("clean-tuned") 3T5D and 6L7D NLROMs.

6.3 Application to the Shallow Cylindrical Shell

The shallow cylindrical shell shown in Figure 4 has been found in this investigation to exhibit two strong nonlinear features, i.e., of mode switching and symmetry breaking. A first challenge of this model construction was the determination of a set of dual modes leading to a good representation of the response in the x and z directions. Following the work on the clamped-clamped curved beam, the first part of the basis was constructed by a proper orthogonal decomposition of the projection of a series (11) of nonlinear Nastran static solutions (SOL 106) corresponding to uniform pressures of different magnitudes with peak transverse displacement extending up to 3.1 thicknesses on the first 8 symmetric linear modes of the undeformed panel. The 6 POD modes with the largest eigenvalues, see Figure 57, were retained as the transverse modes in this computation. Duals were then constructed with the first 2 POD modes as dominant leading to 7 dual modes orthogonal to the first 27 symmetric linear modes. This extended orthogonalization was carried out to eliminate more significantly the transverse components present in the data and thereby generate dual modes with stronger in-plane components that rapidly reduce the in-plane representation error. The identification of the stiffness coefficients was initially done with the single level approach.

6.3.1 Validation Results under Static Load

This 13-mode 6T7D model performed very well in predicting the static response vs. load over a broad range of pressures including the occurrence of a mode switching event. see Figure 58 and Figure 59. A deviation between the maximum displacement and displacement at the center of the panel in transverse direction arises as the load increases.

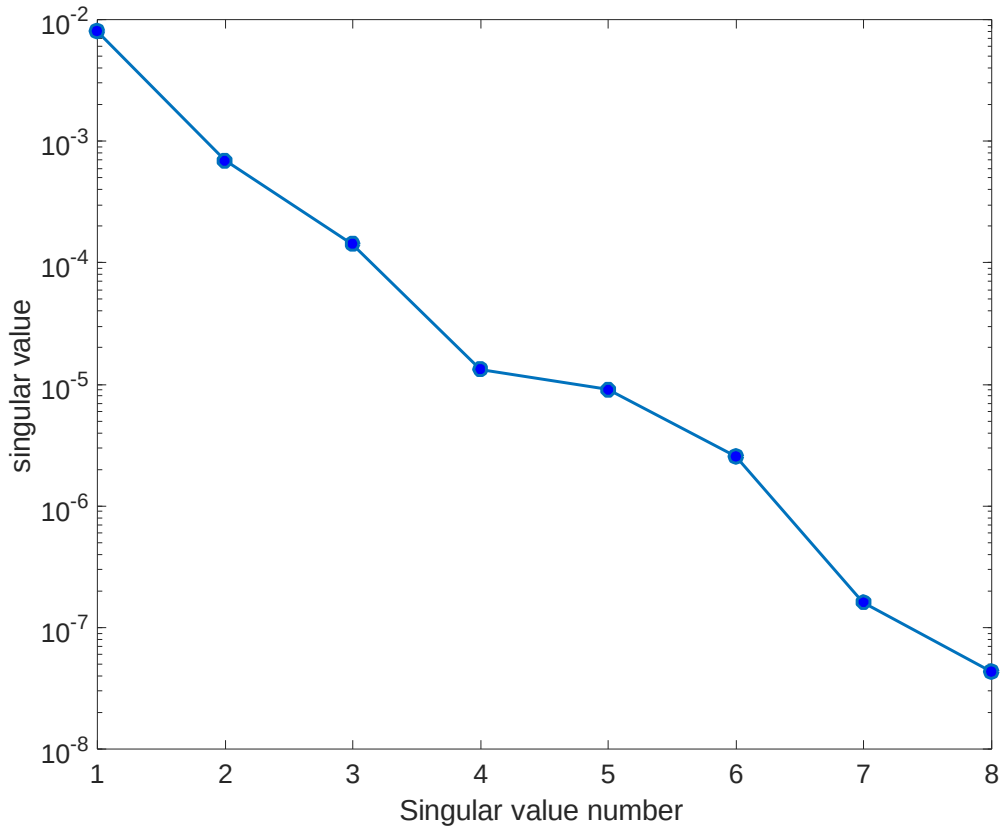

Figure 57. Singular Values of the POD of the Projections on the First 8 Symmetric Linear Modes

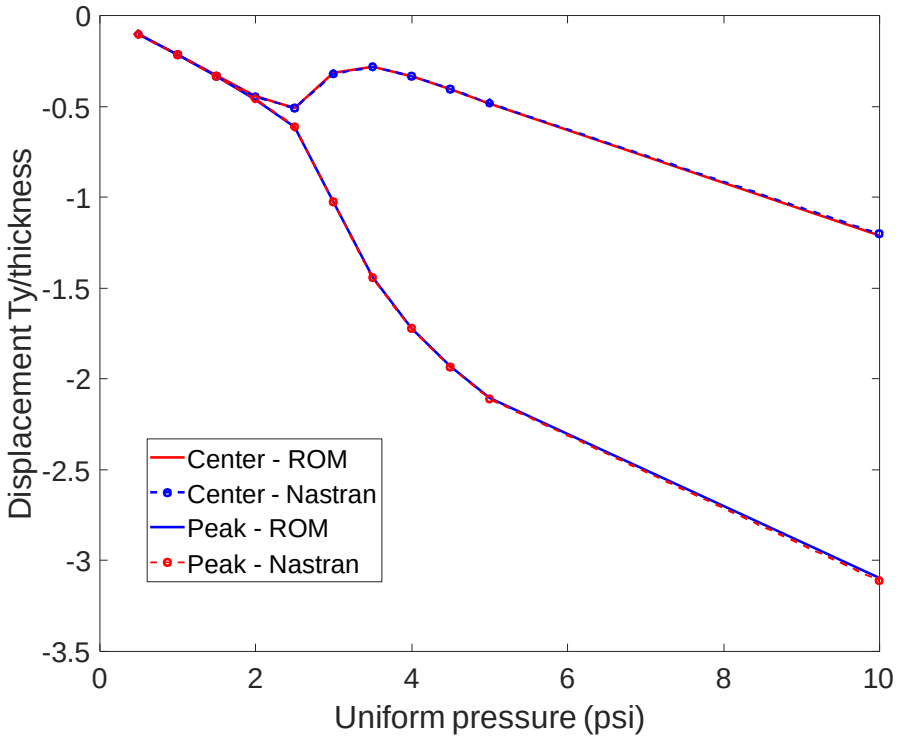

Figure 58. Center and Peak Displacements along the Y (Transverse) Direction vs. Applied Uniform Pressure. Nastran and NLROM Predictions.

Also investigated, see Figure 60, are the first two eigenvalues of the tangent stiffness matrix as a function of the applied pressure. Shown on this figure are the first two Nastran eigenvalues corresponding to symmetric eigenvectors, those of the Nastran tangent stiffness projected on the basis, and those predicted from the NLROM generalized coordinates obtained for the various loading conditions. Note that the Nastran eigenvalues clearly show the veering that is the origin of the mode switching. Moreover, the eigenvalues of the projected tangent stiffness matrix match very well those predicted from the NLROM suggesting that the identified model is accurate but the difference between these two curves and the Nastran one for the second eigenvalue suggests that the basis is not quite appropriate for large enough load levels.

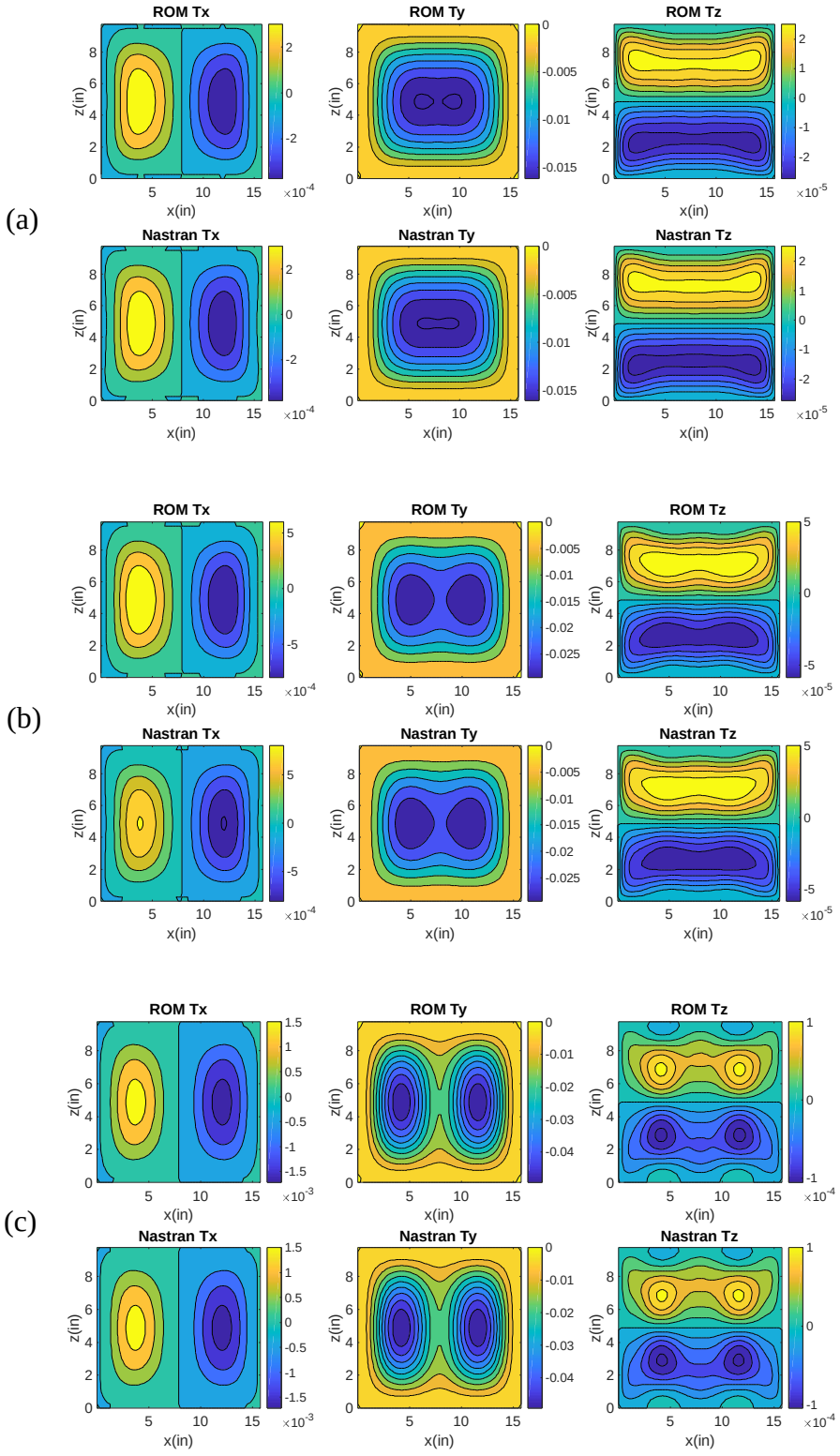

Figure 59. Contour Plots of Displacements along X, Y, Z as Predicted by Nastran and the NLROM for Uniform Pressures of (a) 1.5 psi, (b) 2.5 psi, and (c) 3.0 psi.

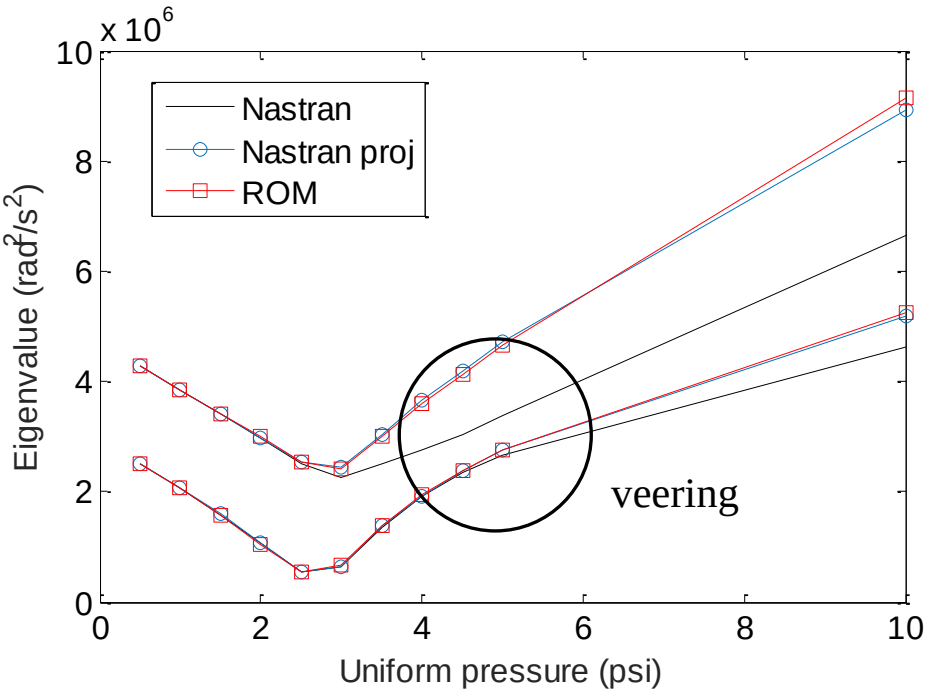

Figure 60. Eigenvalues of the Tangent Stiffness Matrix from Nastran (Corresponding to Symmetric Eigenvectors), Projected Nastran Tangent Stiffness Matrix on the Basis, and from the ROM.

6.3.2 Validation Results under Dynamic Load

6.3.2.1 140dB, 150dB, 160dB

Having successfully predicted the static response of the shell, the NLROM construction focused next on dynamic comparisons under a uniform pressure varying in time as a white noise in the frequency range of [0,500] Hz with variable overall sound pressure levels. It was first recognized that the dynamic response is dominated in the linear case by the first two symmetric modes (of frequencies 272Hz and 346Hz) which are not exactly represented by the 6 POD modes. This issue was resolved by appending to the 6 POD modes, the first 11 linear modes from which they were extracted, then proceeding with a Gram-Schmidt orthogonalization (with respect to the mass matrix) limited to the first 11 modes. These modes are not the linear modes but a rotation of them. They span a

much larger frequency band than necessary, dynamic computations have shown that there is significant out-of-band response, especially at the higher load levels, which warrant the use of that number of modes.

The NLROM considered for dynamic loadings was then obtained by appending the 7 dual modes derived from the 6 POD modes only and this 18-mode model provided an excellent prediction of the Nastran results at the 140dB and 150dB levels, see Figure 61 and Figure 62. However, it did not capture well the high frequency component of the power spectral density at the 160dB. The issue was eventually found to be rooted in a poor identification of some of the nonlinear stiffness coefficients using the single level tangent stiffness approach of [11], even though it has been very successful in many prior applications.

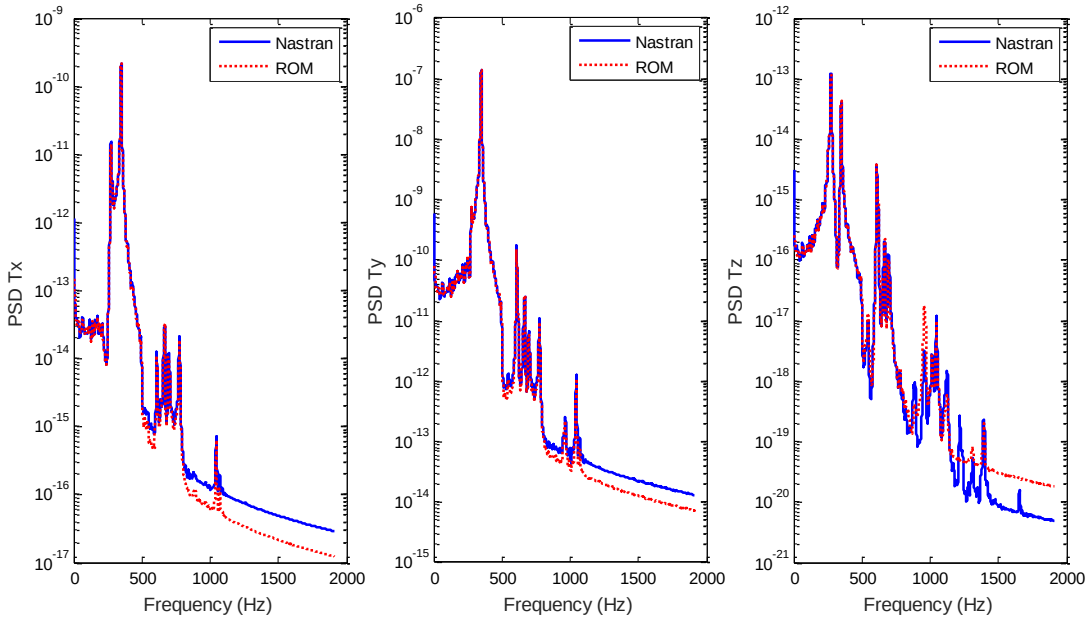

Figure 61. Power Spectral Densities of the Displacements in the X, Y, and Z Directions at the Node 657 Located at Quarter Length of the Panel in both X and Z Directions, OASPL of 140dB.

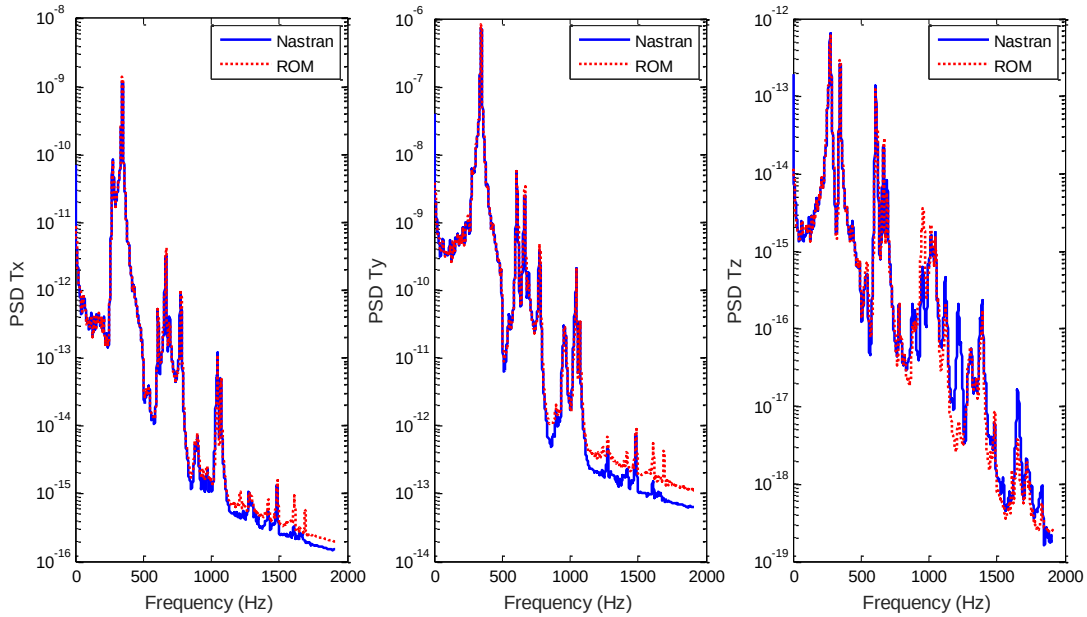

Figure 62. Power Spectral Densities of the Displacements in the X, Y, and Z Directions at the Node 657 Located at Quarter Length of the Panel in both X and Z Directions, OASPL of 150dB.

To resolve this issue, the multilevel identification method developed recently, see [17], was used. In this process, it was found that the difficulties encountered at the 160dB level were resolved and that the 18-mode NLROM does indeed provide a very good match of the Nastran predictions at that level, see Figure 63.

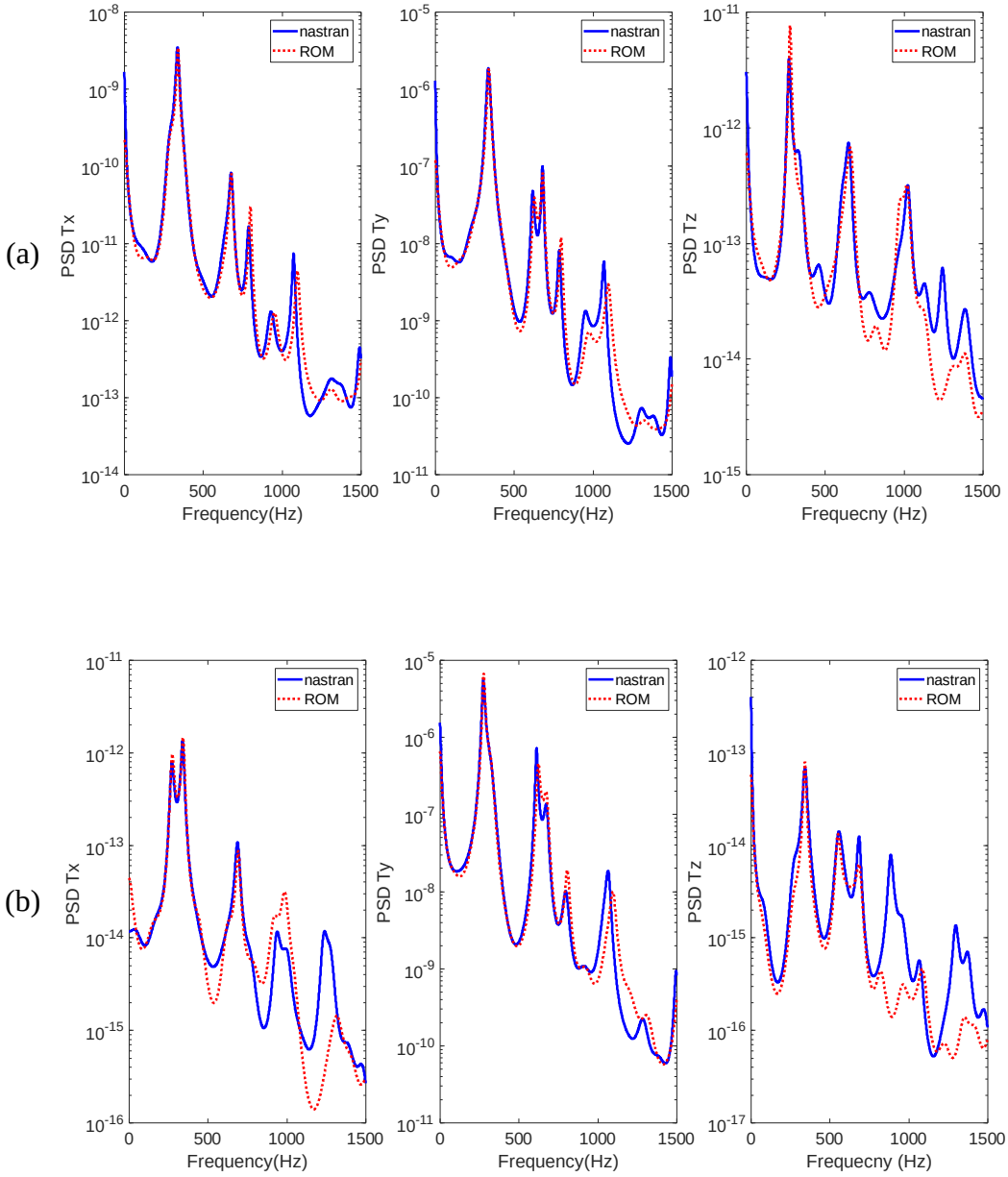

Figure 63. Power Spectral Densities of the Response Corresponding to 160dB Excitation, Nastran and NLROM. (a) Node 657 of Coordinates (0.25,0.25), (b) Node 1248 near Middle. Displacements along the X, Y, and Z Directions.

6.3.2.2 170dB-Symmetry Breaking

Based on the very good results obtained in Figure 63, the analysis proceeded to the higher level of 170dB excitation, see Figure 64. While the NLROM predictions are still very good in the band, there is a clear worsening of the matching with Nastran in the domain [500,1000] Hz. To understand the source of this degradation, a short time history of the full Nastran displacement field was computed and outputted. The representation error of this data with the existing basis and the remaining 18 symmetric linear modes in the range of 1-100 is shown in Figure 65(a). It is seen on this figure that with the 11T7D basis, the representation error is 16% which is certainly too large to have a good match as observed in Figure 64. Moreover, the addition of a series of symmetric linear modes does not lead to a significant reduction of the error, only by about 2.5%!

This observation suggests that the response of the panel may be exhibiting an antisymmetric component. To confirm this assumption, the 18-mode basis was complemented with the 71 antisymmetric modes in the range 1-100 and shown in Figure 65(b) is the corresponding representation error vs. mode number. It is clearly seen that the addition of antisymmetric modes reduces the error significantly, by approximately 13% from 16% to 2.5%. Moreover, much of this drop is generated by the antisymmetric modes 1, 3, and 9 (i.e., linear modes 1, 5, and 14). The inclusion of these 3 modes would lead to a representation error of approximately 6% which is still reasonably large and with no obvious strong contributor, either symmetric or antisymmetric, see Figure 65 (a) and (b).

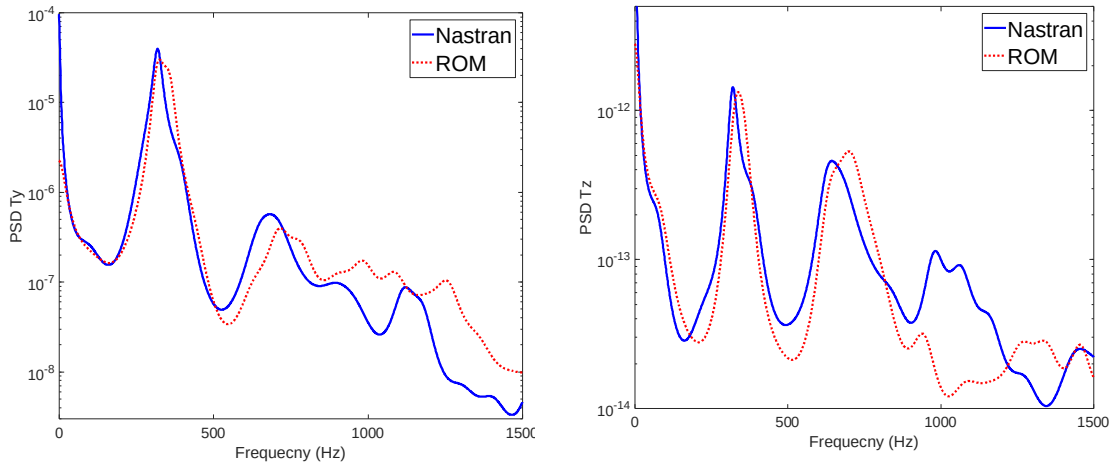

(a) (b)

Figure 64. Power Spectral Densities of the Response Corresponding to 170db Excitation, Nastran and NLROM at Node 1248 near Panel Middle. Displacements along the (a) Y, and (b) Z Directions.

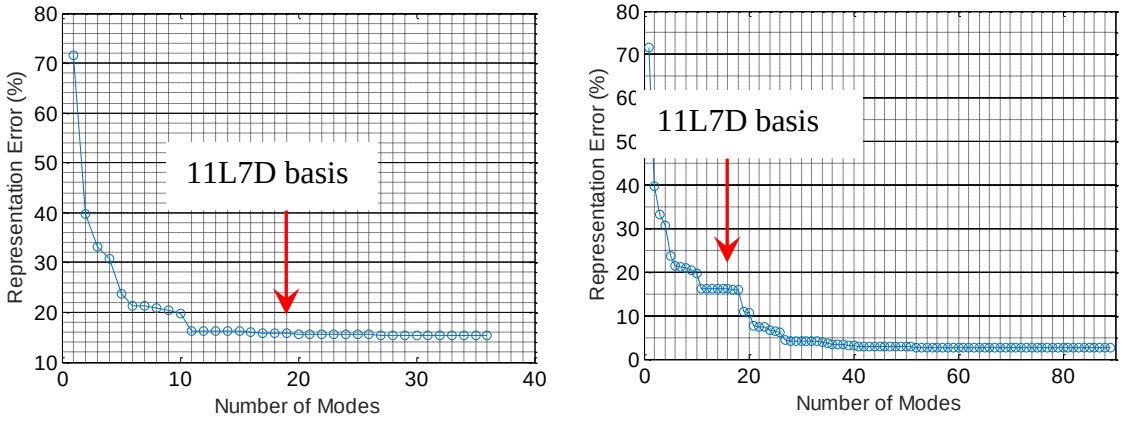

(a) (b)

Figure 65. Representation Errors of a Short Time Nastran Displacement Field Corresponding to a 170db Excitation with the 11T7D Mode Basis and Additional (a) Symmetric, (b) Antisymmetric Modes.

To confirm the presence of antisymmetric components in the Nastran response, segments of the transverse (in the y direction) displacements of the nodes 657, 688, 1873, and 1904 are shown on Figure 67 and Figure 68(a)-(d). These nodes are located

symmetrically with respect to the panel center at (x, z) coordinates (0.25,0.25), (0.25,0.75), (0.75,0.25), and (0.75,0.75) showed in Figure 66. In Figure 67, there is an obvious difference among displacements of the 4 nodes. Zooming in allows to better analyze the symmetry of displacements, see Figure 68. In Figure 68(a), it is seen that the displacements of the 4 nodes overlap with each other and the deformation of the curved panel is symmetric about the two axes. In Figure 68(b), it is seen that the displacements are separated into two groups: nodes 657 and 1873 have the same displacements and nodes 688 and 1904 also have the same displacements but different from the other two. Next, Figure 68(c), the displacements of the 4 nodes are not close to each other. Finally, in Figure 68(d), the situation is different, displacements of nodes 657 and 1904 are the same and nodes 688 and 1873 have the same displacements but different from the other two. These figures confirm the existence of antisymmetry but also demonstrate the type of antisymmetry is not always the same in the same time history so that multiple symmetry breaking modes exist.

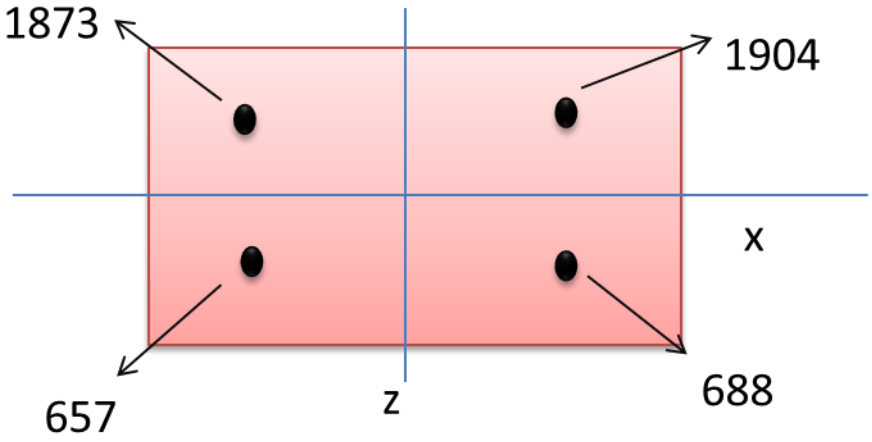

Figure 66 Locations of Four Symmetric Nodes on the Curved Panel

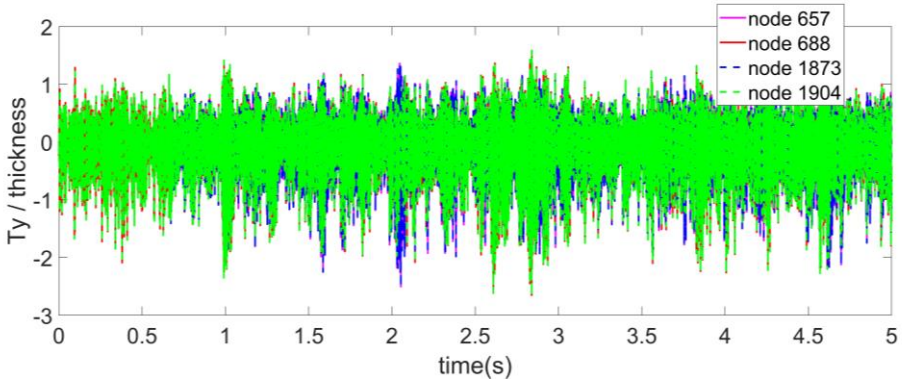

Figure 67. Time History of the Nastran Displacements along the Y Direction at the Nodes 657, 688, 1873, and 1904. 170dB Excitation

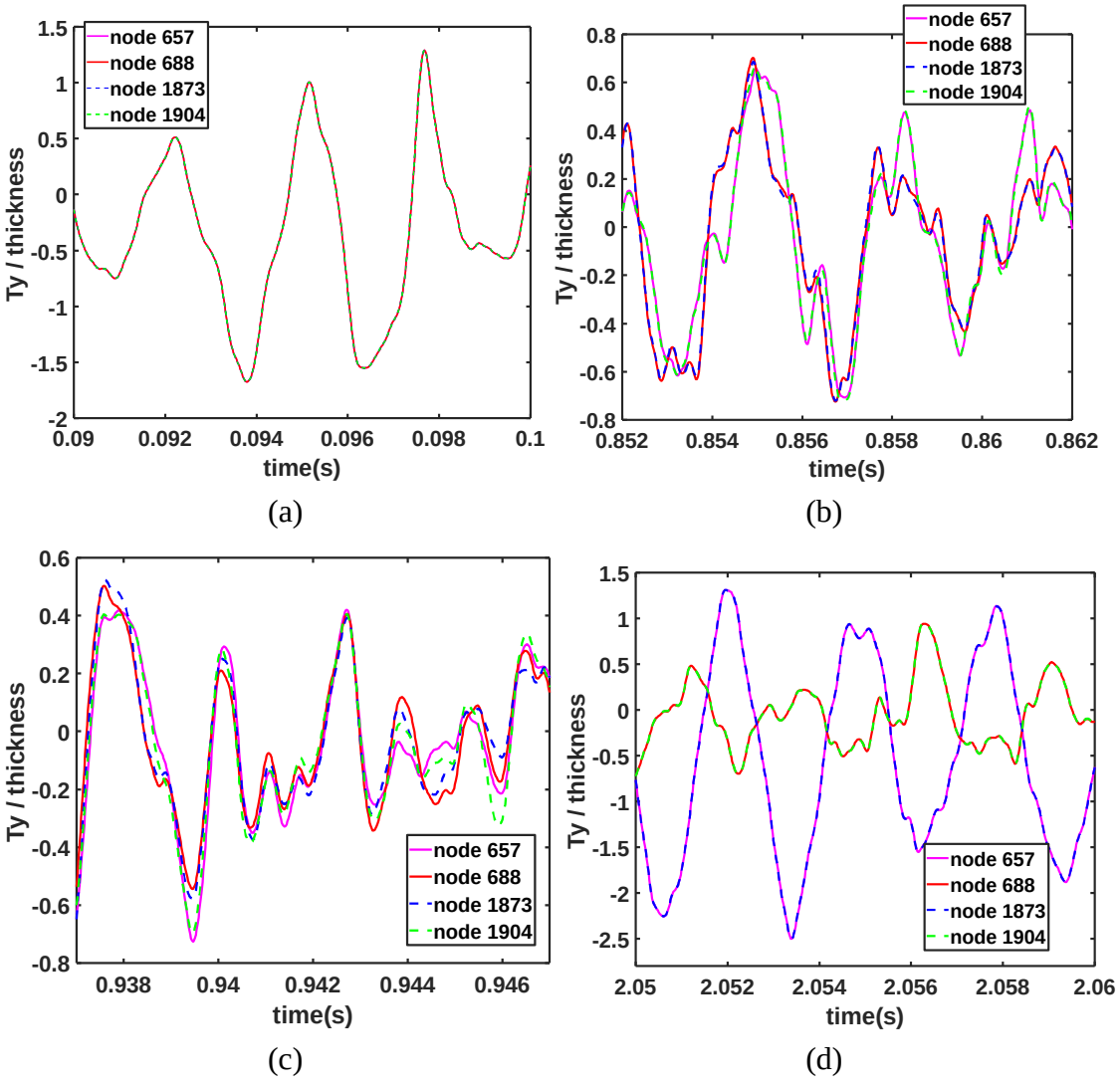

Figure 68 Segment of Time History of the Nastran Displacements along the Y Direction at the Nodes 657, 688, 1873, and 1904. 170dB Excitation

6.4 Application to the Hypersonic Panel

This section focuses on the NLROM validation to the hypersonic panel of Figure 6 introduced in [1] and of which a structural NLROM was originally constructed in [2]. The focus of this effort was on revisiting the NLROM of [2], especially seeking a reduced number of basis functions by relying on the proper orthogonal decomposition (POD) based optimization of transverse modes already successfully demonstrated in earlier reports on the curved clamped-clamped beam and the cylindrical panel. The issue of identification of the stiffness coefficients of this novel NLROM will also be addressed.

Consistently with the arguments of [27], the frequency band of interest for the panel of Figure 6 was selected to be [0, 2000] Hz which contains 30 linear modes, 16 of which have the appropriate symmetry (left-right of the flow) to be included in the NLROM basis.

The first effort focused on the selection of the basis functions that are primarily transverse on the skin and are related to the 16 linear modes. To this end, a set of static loadings with a uniform pressure ranging from -4 to 4 psi were imposed on the finite element model and the corresponding displacement fields determined. These static solutions were then projected on the 16 linear modes and a POD analysis of the resulting 16 generalized coordinates was carried out. Shown in Figure 69 are the resulting eigenvalues showing that there is 1 dominant eigenvector and 2 that are smaller but significant. A different but related perspective is shown in Figure 70 which shows the average representation error of the displacements along z of all degrees of freedom (skin and stiffeners) as functions of either the POD eigenvectors or the linear modes. Note that the error is averaged over the set of the data corresponding to loads from -7 to +7 psi.

Clearly, 3 POD eigenvectors are dominant while the number of significant linear modes is larger, at least 4, possibly 7.

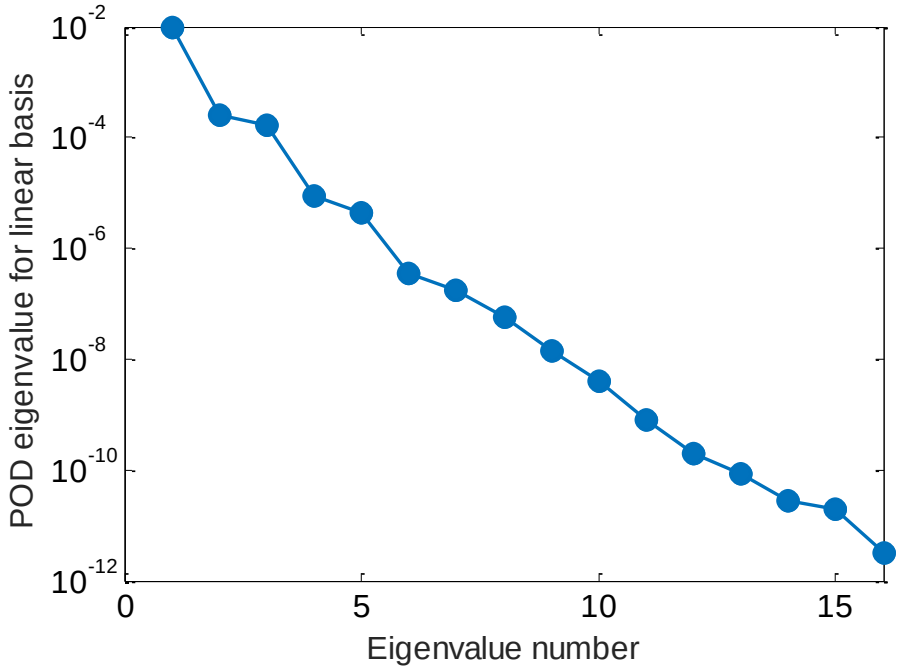

Figure 69. Eigenvalues of the POD of the Projection of the Panel Response to the 11 Uniform Presssures on the 16 Linear Modes.

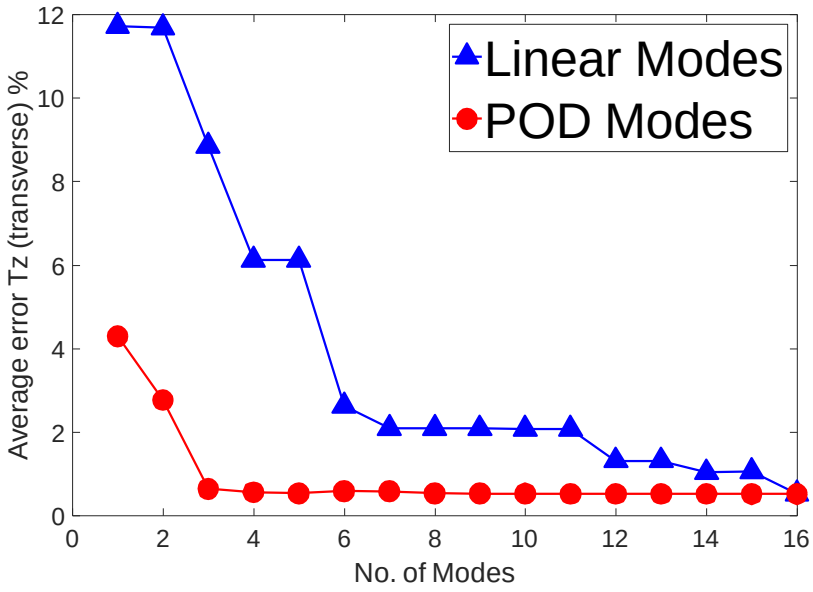

Figure 70. Average Representation Errors of the Set Of 11 Static Displacements under Uniform Pressure. Displacements along Z, Entire Panel. Linear Modes and POD Eigenvectors.

Proceeding as with the curved clamped-clamped beam and the cylindrical shell, the POD eigenvectors were used to define the duals to be added to the basis. Combinations of the first 3 POD eigenvectors were considered, i.e., 1-1,1-2,1-3,2-2,2-3,3-3, resulting in 10 dual modes.

The combination of the 16 POD or linear modes and the 10 dual modes led to a very good representation of the static displacements also in the x and y displacements, see Figure 71.

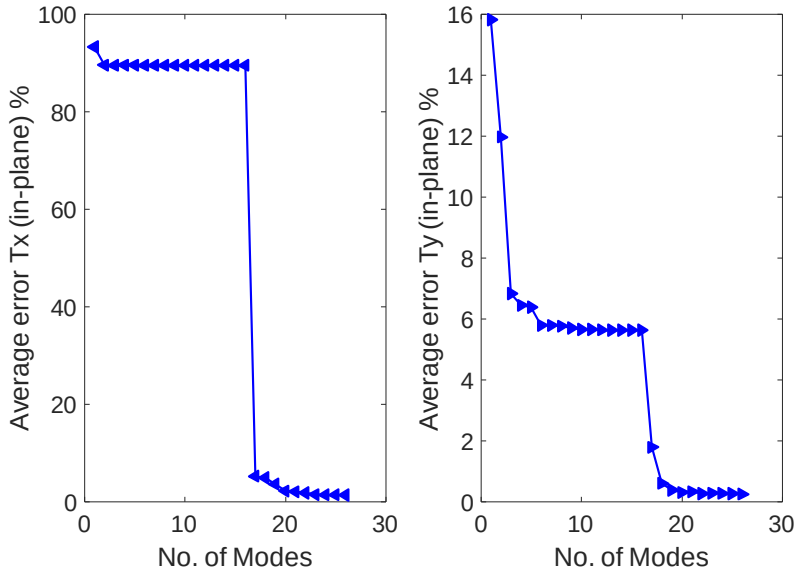

Figure 71. Average Representation Errors of the Set of 11 Static Displacements under Uniform Pressure. Displacements along X (Left) and Y (Right), Entire Panel. 16 POD Eigenvectors and the 10 Dual Modes.

It is seen from Figure 71 that the 1st dual mode (mode 17) has a huge contribution, dramatically reducing the error, especially in the x direction (left plot), from 90% to 5%. It also reduces the error on the larger y displacements from 6% to 0.2%. From Figure 70 and Figure 71, it is concluded that the first 3POD modes (modes 1,2, and 3) and the first 2 dual modes (mode 17 and 18) have the largest impact on the modeling of the data.

Based on the above excellent results, the coefficients of the 16POD10D NLROM were identified using the tangent stiffness matrix approach and either a single level or the multiple level approach [17]. Unfortunately, it was found that neither of these NLROMs was stable even after cleaning. Since the 16POD and 16 linear modes span the same space, being linear combinations of each other, a second NLROM was constructed with the 16L10D basis. This NLROM was found to be slightly more stable, converging - when cleaned and identified from either single of multiple level.

A similar behavior was observed with the curved clamped-clamped beam and the issue was resolved by reducing the basis. Accordingly, a similar effort was initiated here with a decrease of the number of POD modes which was reduced to 3. Moreover, the dual selection process was redone with the combinations 1-1,1-2,1-3 since the contribution of the first POD mode is much larger than the ones of the 2nd and 3rd eigenvectors. This led to 8 duals and thus a 3POD8D basis. Another selection of duals, all based on the 1-1 combination let to a 3POD5D basis and both of them were considered further.

The average representation errors of the uniform pressure data with these bases are good, see Figure 72, the errors in the z direction are less than 0.5% while the errors along the x directions are 1.3% for 3POD8D and 2.3% for 3POD5D. The errors on the larger y displacements are both less than 1%.

6.4.1 Validation Results before Tuning

These two models were identified using the single level tangent stiffness matrix approach and were found to be stable with or without cleaning (3POD5D NLROM) and

with cleaning only (3POD8D). The static predictions of these models are summarized in Figure 73 for the maximum z displacement of the skin while the entire displacement fields are shown in Figure 75-Figure 76 for 3 specific loads.

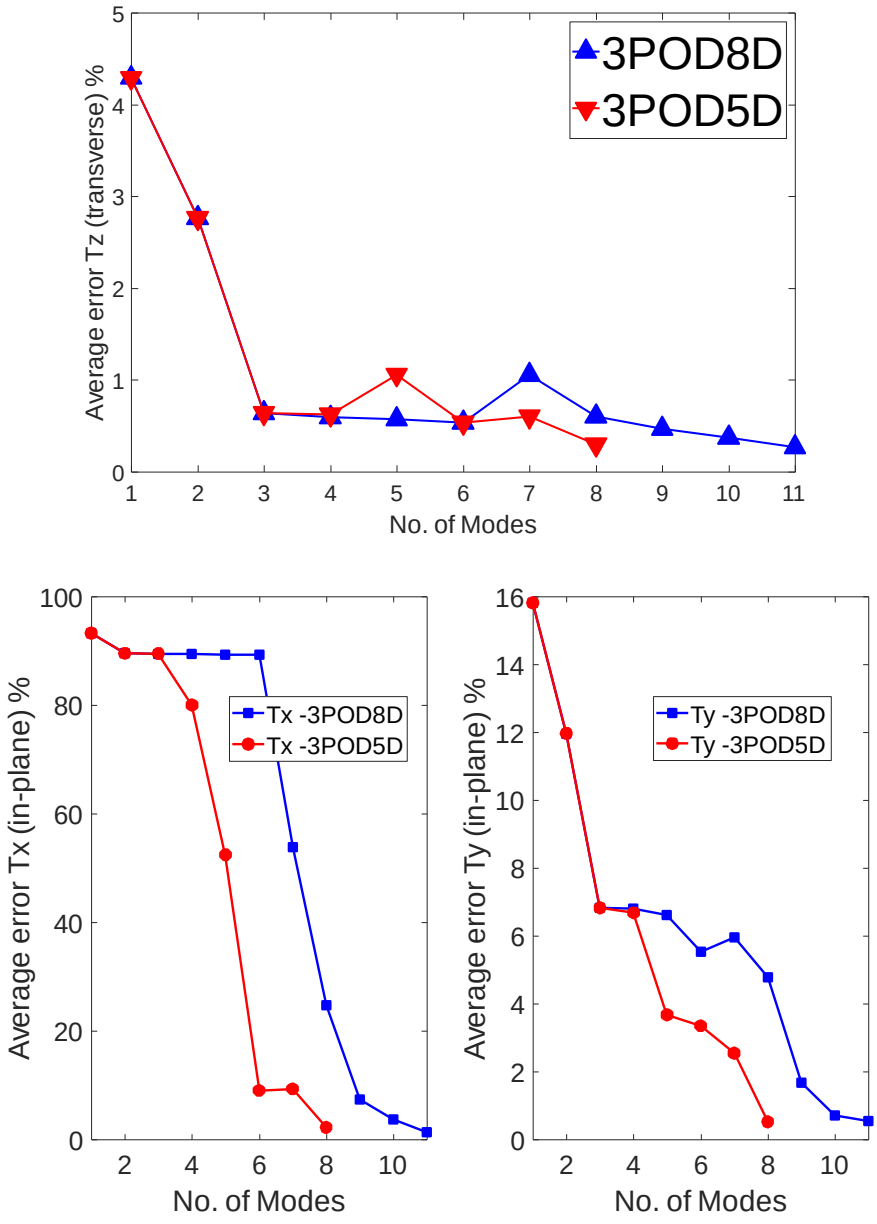

Figure 72. Average Representation Errors of the Set of 11 Static Displacements under Uniform Pressure. Displacements along Z (Top), X (Bottom Left), and Y (Bottom Right). as a Function of the Mode Number (Transverse Then Dual), 3POD8D and 3POD5D Bases.

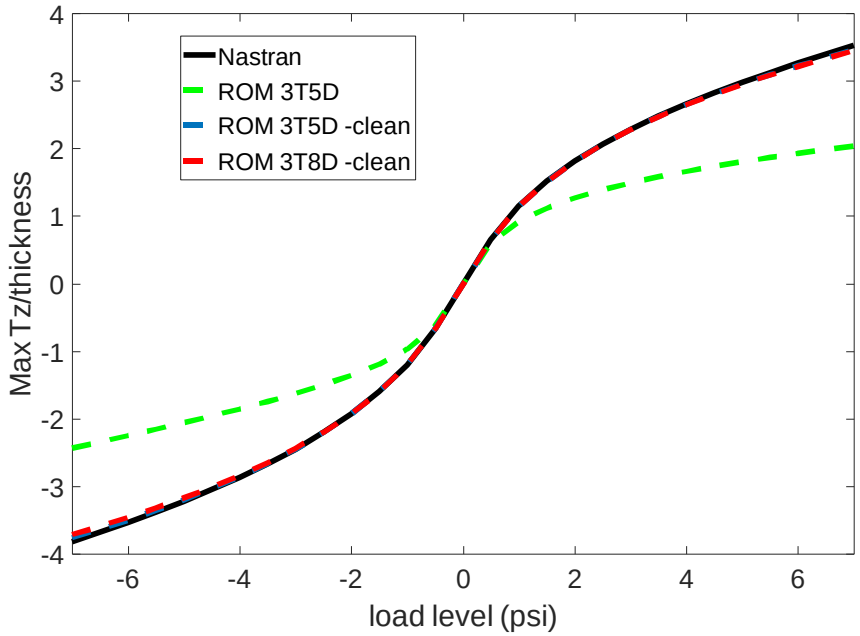

Figure 73. Maximum Displacement along the Z Direction.Nastran and the 3 NLROMs.

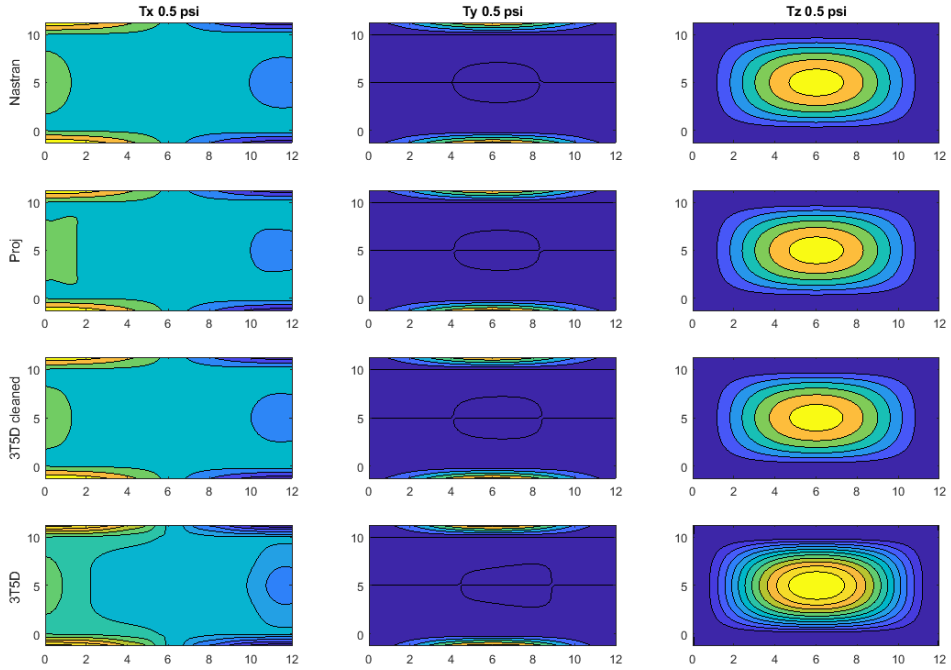

Figure 74. Displacements Fields along the X, Y and Z Directions on the Skin and Stiffeners (Flattened) Predicted by Nastran, Projection of Nastran on the Basis, and the 3POD5D ROM both Cleaned and Not. Uniform Pressure of 0.5 psi (Upward).

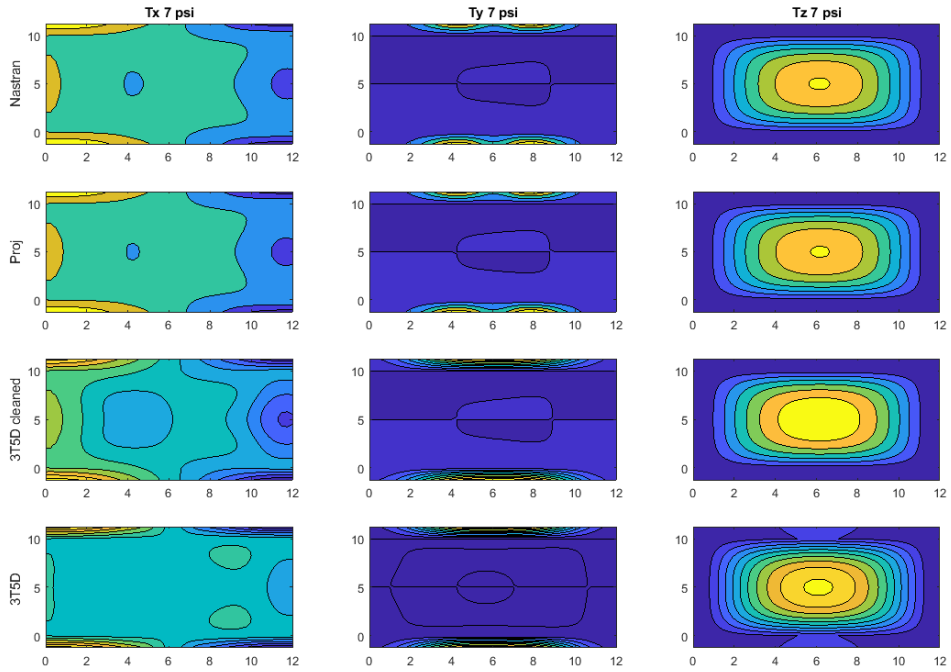

Figure 75. Displacements Fields along the X, Y, and Z Directions on the Skin and Stiffeners (Flattened) Predicted by Nastran, Projection of Nastran on the Basis, and the 3POD5D ROM both Cleaned and Not. Uniform Pressure of 7 psi (Upward).

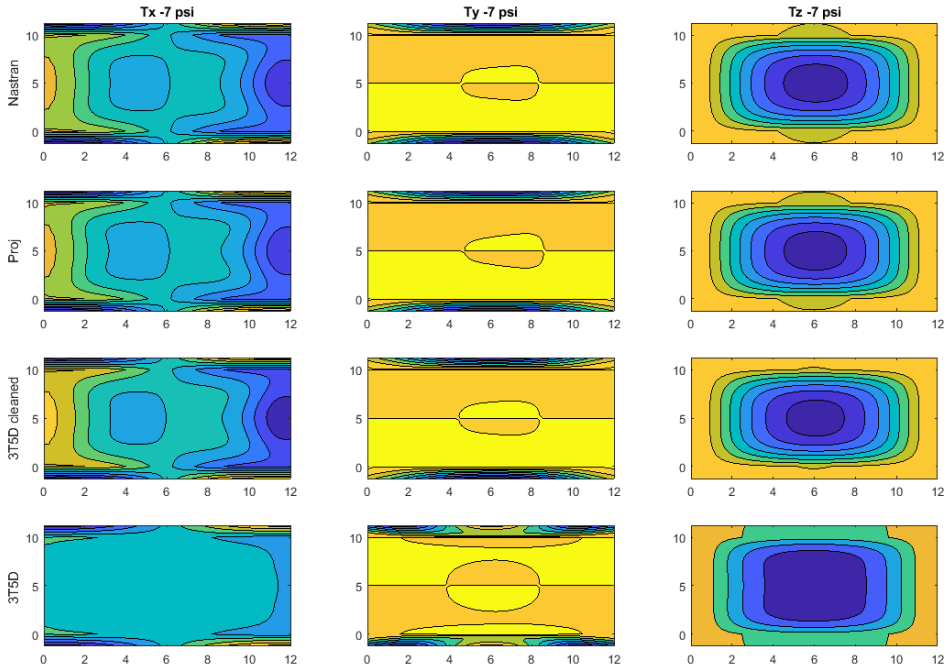

Figure 76. Displacements Fields along the X, Y, and Z Directions on the Skin and Stiffeners (Flattened) Predicted by Nastran, Projection of Nastran on the Basis, and The 3POD5D ROM Both Cleaned and Not. Uniform Pressure of -7 psi (Downward).

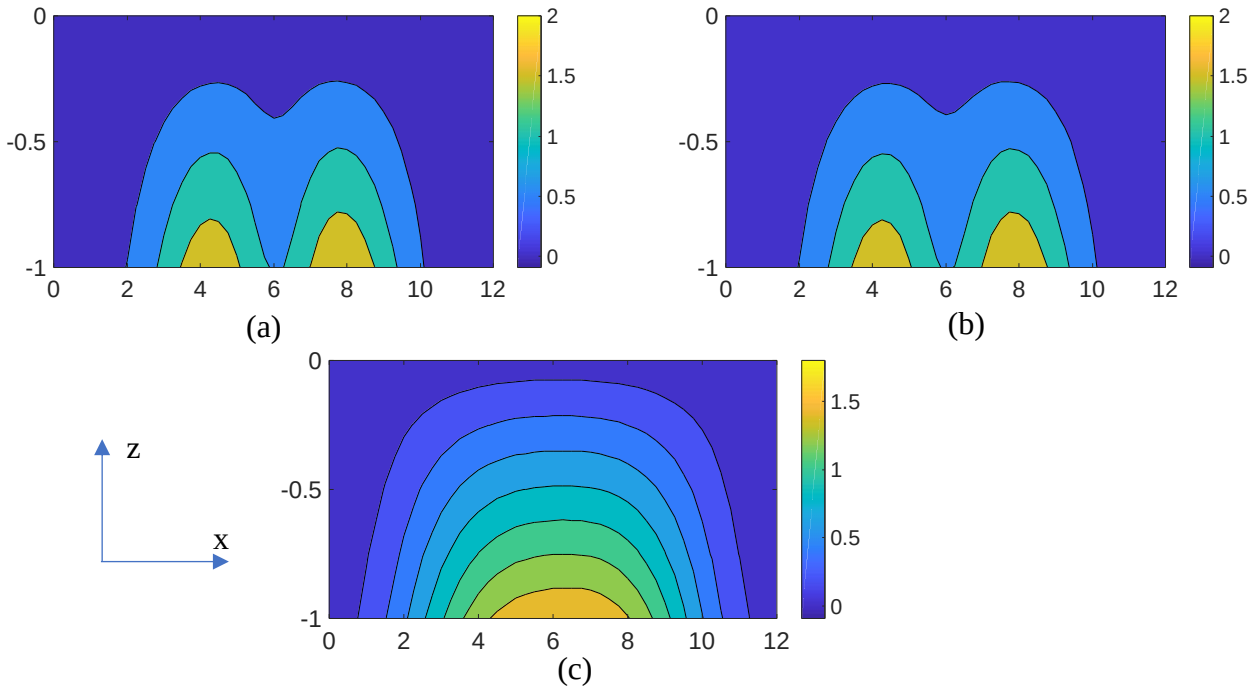

Figure 77. Displacements along the Y Direction on the Right Stiffener Predicted by (a) Nastran, (b) Projection of Nastran on the Basis, and (c) the Cleaned 3POD5D ROM Uniform Pressure of 7 psi (Upward).

It is seen from Figure 74-Figure 76 that the cleaning of the 3POD5D NLROM is very beneficial, enabling a good to excellent match of the Nastran results through most of the loading domain at the contrary of the uncleaned model which is only good for small pressures.

Figure 75 is particularly interesting as it corresponds to a loading for which there exists a local buckling of the stiffeners most visible by the “two waves” in the y displacement of this component, see Figure 77 for zoom. Interestingly, the basis appears to capture that effect since the Nastran projected results also display the same feature. The predictions from the cleaned NLROM (the prediction of the original one is quite far) are

not good however and thus suggest that the identification of the coefficients may be at fault.

After the success obtained with the fine tuning of the NLROM coefficients for the clamped-clamped curved beam, a similar effort was undertaken for the above 3POD8D (3T8D) NLROM.

The validation of this NLROM has been partially successful. The transverse (T_z) displacement predicted by the NLROM was quite close to the Nastran SOL 106 results but the local buckling on stiffeners was not correctly captured as seen in Figure 78: the finite element results exhibit 2 peaks while those from the NLROM exhibit only one. Since this local buckling is the strong nonlinearity of interest for this panel, it is desired to extend the current methodology to capture the two peaks.

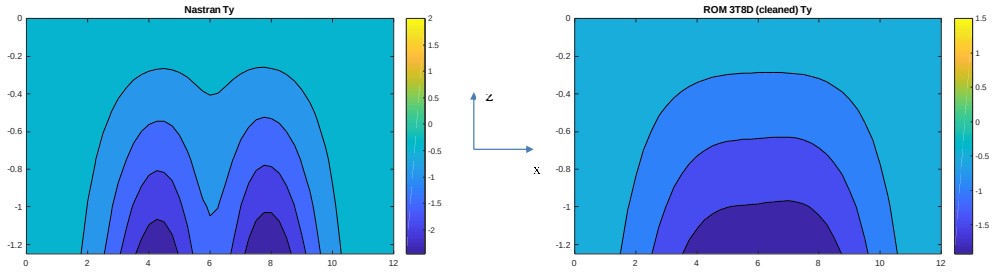

(a) (b)

Figure 78. Displacements along the Y Direction on the Right Stiffener Predicted by (a) Nastran, (b) the Cleaned 3POD8D ROM Uniform Pressure of 7 psi (Upward).Validation Results after Tuning

The methodology used for the clamped-clamped curved beam was repeated here. That is, the stiffness coefficients $K^{(2)}_{tdd}$, $K^{(2)}_{dtd}$, $K^{(2)}_{ddd}$, $K^{(3)}_{tttd}$, $K^{(3)}_{dttt}$, $K^{(3)}_{ttdd}$, and $K^{(3)}_{dttd}$ ($K^{(3)}_{tddd}$, $K^{(3)}_{dtdd}$, and $K^{(3)}_{ddddd}$ were not included here) were tuned to make the predicted

results from the NLROM match their Nastran counterparts. Before tuning, a projection was performed of Nastran displacements on the 11 modes (3T8D). For this effort, 40 load levels were selected as [-10:0.5:-0.5, 0.5:0.5:10] psi. To evaluate the importance of each mode, the absolute values of the projection of the 40 displacements were averaged for each mode and are shown in Figure 79. It is seen from this figure that the projection coefficients of the last 3 modes are relatively small compared to the others. Accordingly, and to minimize the number of stiffness coefficients to be tuned, only the stiffness related to the first 8 modes are taken into consideration of tuning.

The load levels selected for the tuning were [-10 -8 -3 2.5 5] psi, see Figure 73 for the loading curve. It is seen that the predictions from the NLROM already match well with the Nastran results before tuning when the pressure is within [-5, 5] psi. The discrepancy between these two predictions occurs for higher pressures. After tuning, the discrepancy under large negative load has disappeared but a zigzag pattern is observed in the response for load levels between 5.5 psi and 10 psi. This odd behavior is in fact due to a lack of stability of the tuned NLROM in that loading zone with the results of Figure 80 obtained with the arclength method. Note that this region of instability of the model reasonably matches the region in which the local buckling develops.

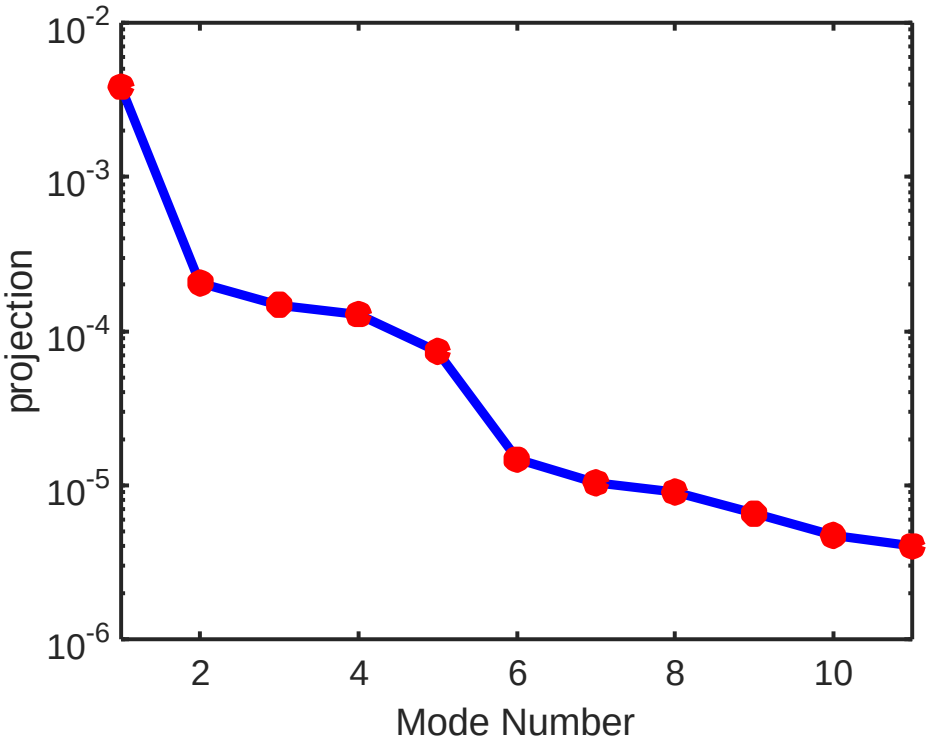

Figure 79. Average of Absolute Value of Projection Coefficients of the 40 Nonlinear Nastran Responses on Each NLROM Mode.

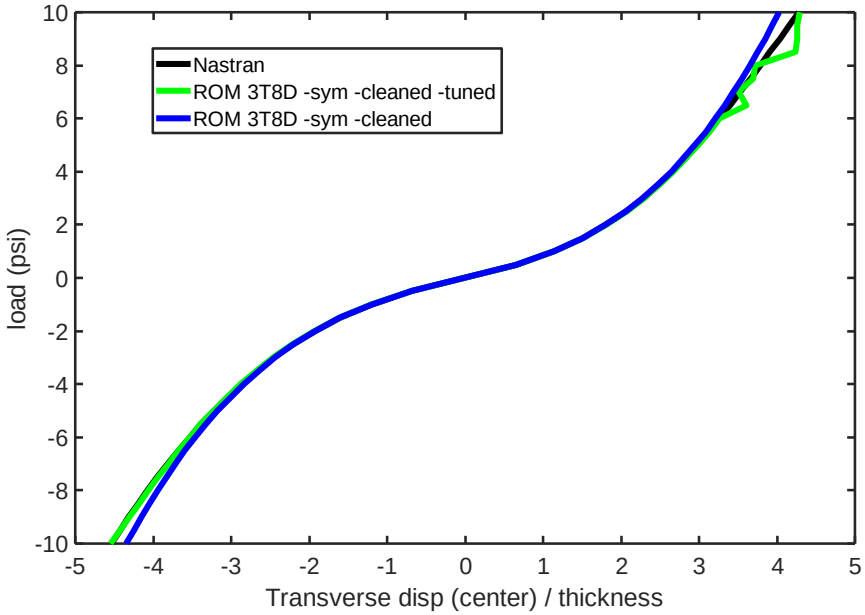

Figure 80. Transverse Deflection of the Center of the Panel vs. Uniform Applied Pressure on Skin. Nastran, and Predictions from the 3T8D NLROM before ("sym-cleaned") and after Turning ("sym-cleaned-tuned").

Shown in Figure 81 is the lowest eigenvalue of the tangent stiffness matrix plotted as a function of the applied pressure obtained from Nastran (SOL 106) directly, its projection on the NLROM basis, and the predictions from the original and tuned NLROMs. This figure is very instructive. It shows first that the basis is not appropriate to predict the local buckling, notwithstanding the observation of Figure 77. Indeed, the behavior of the panel for pressures larger than 5 psi, as the projection of the Nastran tangent stiffness matrix on the basis does not follow the large drop seen by the Nastran curve, it only shows a very slight dip. The predictions from the original NLROM do not show any dip at all while the tuned NLROM is clearly seen to exhibit instability as the local buckling starts.

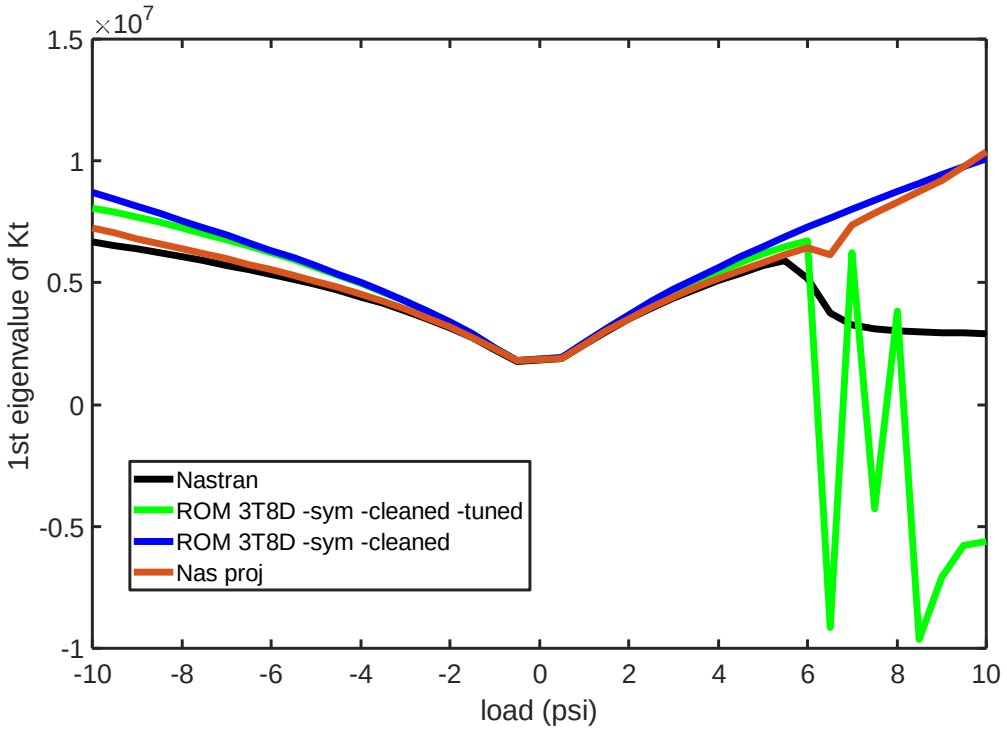

Figure 81. Lowest Eigenvalue of the Tangent Stiffness Matrix vs. Uniform Applied Pressure on Skin. Nastran, its Projection on the 3T8D Basis, and Predictions from the 3T8D NLROM before ('sym-cleaned") and after Turning ("sym-cleaned-tuned").

It is also seen on Figure 81 that there exists a discrepancy between the NLROM predicted eigenvalues and those obtained by projecting the Nastran tangent stiffness on the basis. That discrepancy is slightly reduced in the tuning but is still significant. This discrepancy may suggest that the remaining NLROM coefficients, i.e., those of the form $K_{tt}^{(1)}$, $K_{td}^{(1)}$, $K_{dd}^{(1)}$, $K_{ttt}^{(2)}$, $K_{ttd}^{(2)}$, and $K_{tttt}^{(3)}$ may not be very accurately identified. To assess this possibility, a sensitivity analysis was performed by reducing by 0.5% percent each coefficient in turn and recomputing the corresponding change in the first eigenvalue of the tangent stiffness matrix at 3 psi. Those with the largest effect are listed in Table 9-Table 10.

Table 9. Relative Change in Lowest Eigenvalue of 3T8D NLROM Tangent Stiffness Matrix at 3 psi Induced by a Change of 0.5% of Selected Quadratic Coefficients.

Quadratic stiffness	K_{114}	K_{134}	K_{119}	K_{124}	K_{116}
Variation (%)	4.51	0.78	-0.61	0.22	-0.14

Table 10. Relative Change in Lowest Eigenvalue of 3T8D NLROM Tangent Stiffness Matrix at 3 psi Induced by a Change of 0.5% of Selected Cubic Coefficients.

Cubic stiffness	K_{1111}	K_{1113}	K_{1112}	K_{1123}	K_{1133}	K_{1233}	K_{1222}	K_{1122}
Variation (%)	-2.50	-0.67	-0.27	-0.20	-0.14	-0.029	-0.028	-0.023

A tuning of these terms was performed for the cleaned 3T8D NLROM focusing on the lowest eigenvalue of the tangent stiffness matrix at the pressure of 3 psi. It is seen from Figure 82 and Figure 83 that the matching of the lowest eigenvalue is improved after tuning of these terms and that the displacement did not worsen. Nevertheless, this process could not generate the dip of the lowest eigenvalue that is shown by the projection of the Nastran results on the basis in the neighborhood of local buckling.

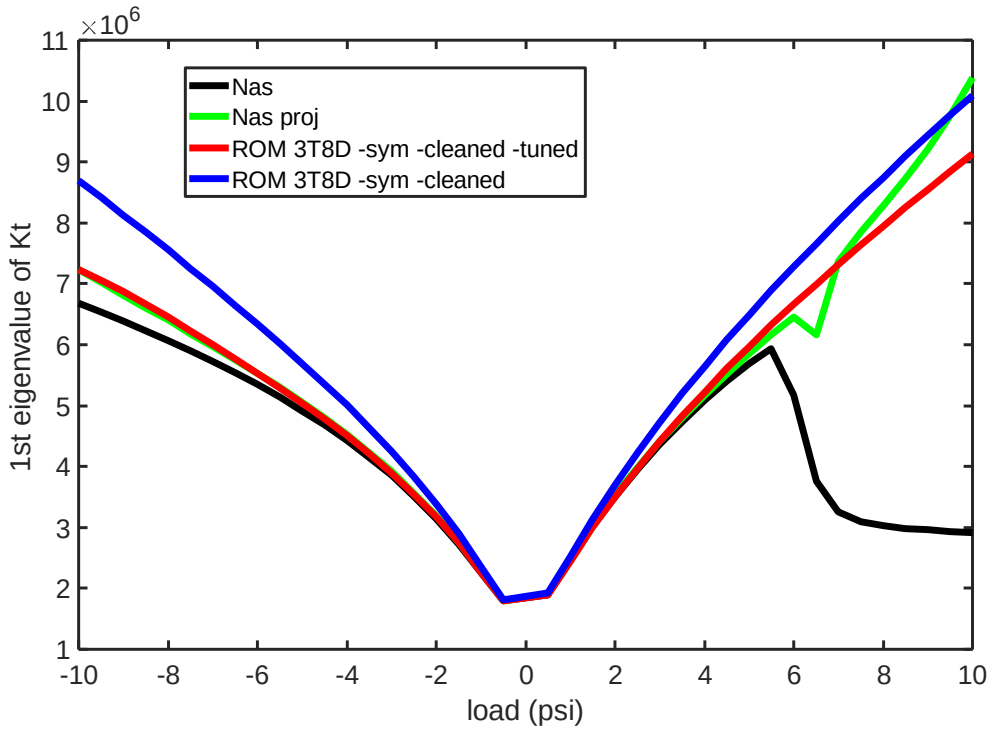

Figure 82. Lowest Eigenvalue of the Tangent Stiffness Matrix vs. Uniform Applied Pressure on Skin before and after Tuning. Nastran, its Projection on the 3T8D Basis, and Predictions from the 3T8D NLROM Before ('sym-cleaned") and After Additional Turning ("sym-cleaned-tuned").

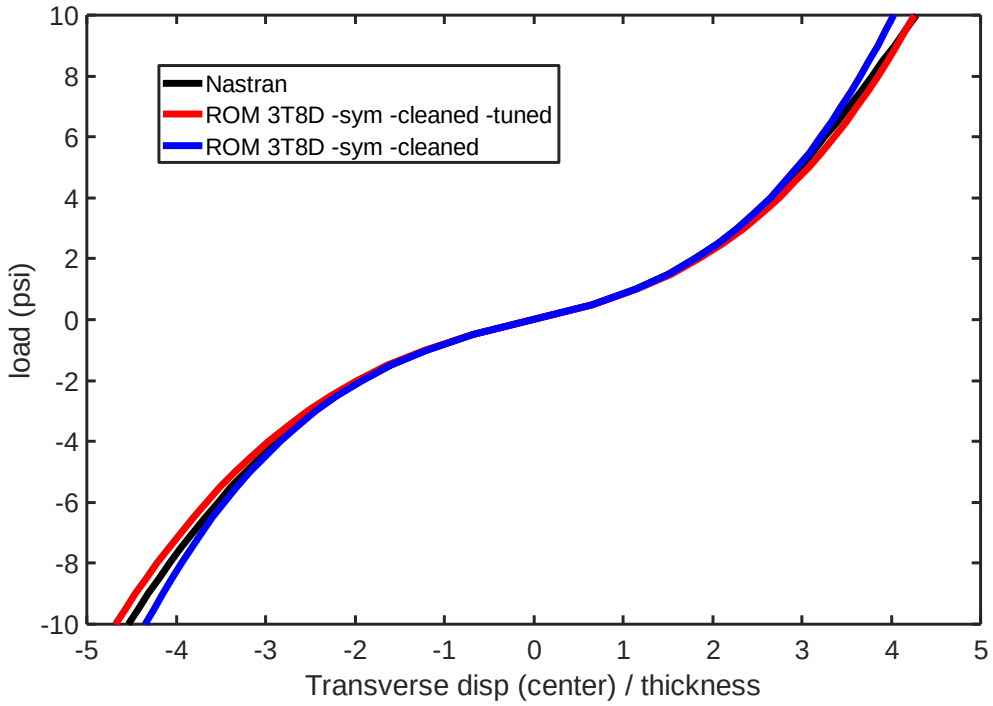

Figure 83. Transverse Deflection of the Center of the Panel vs. Uniform Applied Pressure on Skin. Nastran, and Predictions from the 3T8D NLROM Before ('sym-cleaned") and AfterAdditional Turning ("sym-cleaned-tuned").

The above discussion demonstrates that the NLROM basis would indeed need to be improved to capture the local buckling. The first efforts in this direction focused on enriching the basis with modes extracted from response quantities in the direct neighborhood of the local buckling. As seen from Figure 80-Figure 83, the tangent stiffness matrix is much more sensitive to this event that the displacements. Accordingly, the enrichment was attempted from the eigenvectors of the tangent stiffness matrix at the 10 load levels selected as [5.5:0.5:10] psi. For simplicity, the eigenvector corresponding to the lowest eigenvalue of the Nastran tangent stiffness matrix was simply appended to the basis and the projection of this matrix on the new basis recomputed and reanalyzed.

(a)

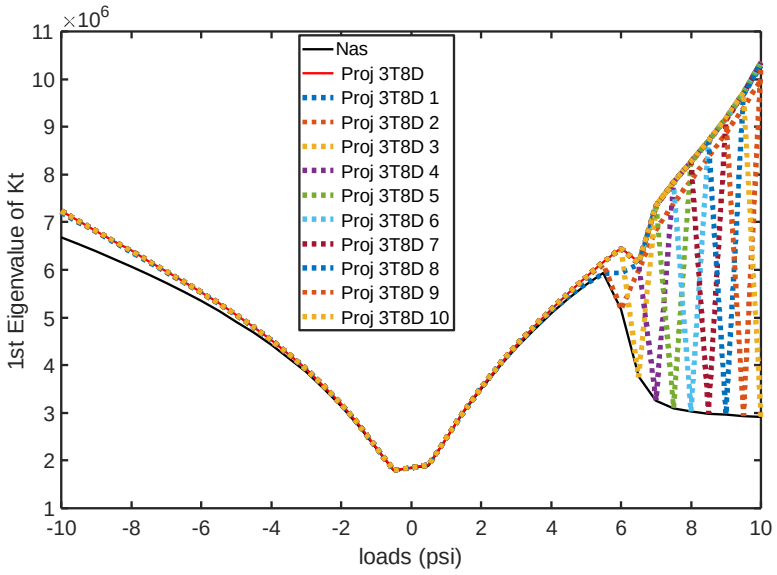

(b)

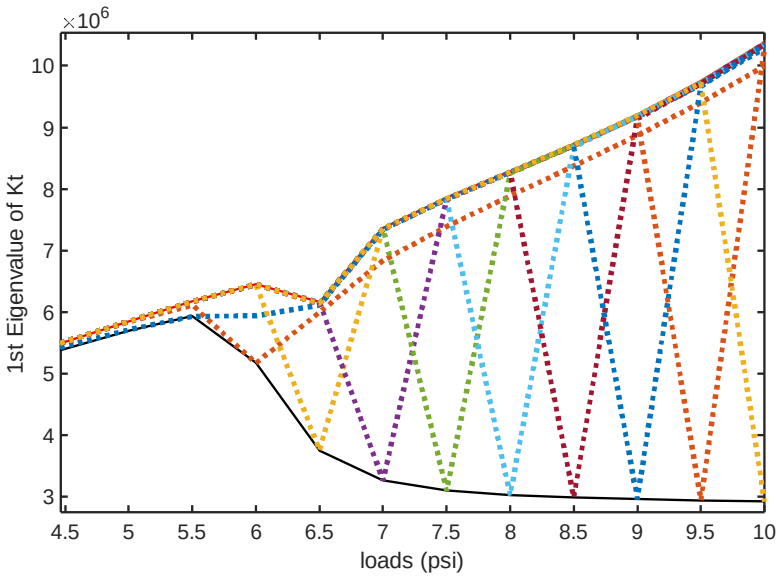

Figure 84. (a) Lowest Eigenvalue of the Tangent Stiffness Matrix vs. Uniform Applied Pressure on Skin. Nastran, its Projection on the 3T8D Basis, and 3T8D Basis Enriched with the Nastran Eigenvectors one at a Time.
(b) Same as (a) Zoomed.

Shown in Figure 84 is the result of this process when each one of the 10 eigenvectors is appended, one at a time, to the basis. Quite surprisingly, it is seen that the addition to the basis of the eigenvector corresponding to a particular load level only really improves the capturing of the lowest eigenvalue at that load level. This finding implies that

the behavior of the structure in this region changes quickly from one load to the other. To obtain a better understanding of this situation, the MAC values of the 10 eigenvectors were computed. The MAC, modal assurance criterion, is a standard measure introduced to make a correspondence between experimental mode shapes and finite element ones, but it can be used more broadly to compare two modes. It is defined as

$$MAC = \frac{\left|\phi_i^T \phi_j\right|}{\sqrt{\left(\phi_i^T \phi_i\right)\left(\phi_j^T \phi_j\right)}} \qquad (63)$$

where ϕ_i and ϕ_j are two different modes. The MAC is between 0 and 1 (by Cauchy-Schwarz inequality) and the modes look similar if MAC > 0.9 or so. The MAC numbers for the 10 eigenvectors are listed in Table 11.

Very surprisingly, it is found that many of these values are very close to 1 suggesting that the modes should be very similar – while in fact the results of Figure 84 show the contrary.

One possible option to explain these seemingly conflicting observations is that the difference between two eigenvectors is primarily along in-plane directions of which the components are small but stiff. Thus, small differences in those degrees of freedom would only marginally affect the MAC but would affect much more significantly the eigenvalues of the tangent stiffness matrix. To validate this possibility, the difference between the eigenvectors corresponding to the 4th and 8th loading levels was computed, then the potential energy (based on the linear stiffness matrix) corresponding to this difference determined. This energy was found to be 10.4% of the corresponding energy of either

eigenvectors, which is quite large considering that the MAC value is 0.984. This check validates the proposed explanation for the behavior of Table 10 and Figure 84.

Table 11. Modal Assurance Criterion (MAC) Values of the 10 Eigenvectors of the Nastran Tangent Stiffness Matrix Corresponding to the Lowest Eigenvalue and 10 Different Loads Near Local Buckling.

Enrichment	1	2	3	4	5	6	7	8	9	10
1	1.00	0.47	0.00	0.03	0.03	0.04	0.04	0.04	0.04	0.04
2	0.47	1.00	0.18	0.09	0.06	0.04	0.03	0.02	0.01	0.00
3	0.00	0.18	1.00	0.96	0.92	0.95	0.94	0.97	0.95	0.74
4	0.03	0.09	0.96	1.00	0.99	0.99	0.99	0.98	0.98	0.89
5	0.03	0.06	0.92	0.99	1.00	0.99	0.99	0.96	0.98	0.93
6	0.04	0.04	0.95	0.99	0.99	1.00	1.00	0.98	0.99	0.90
7	0.04	0.03	0.94	0.99	0.99	1.00	1.00	0.99	0.99	0.90
8	0.04	0.02	0.97	0.98	0.96	0.98	0.99	1.00	0.99	0.84
9	0.04	0.01	0.95	0.98	0.98	0.99	0.99	0.99	1.00	0.88
10	0.04	0.00	0.74	0.89	0.93	0.90	0.90	0.84	0.88	1.00

The overall conclusion of the above effort is that the local deformations around the local buckling zone change significantly as the load is increased past the buckling point. Thus, capturing the behavior of the panel in this loading region would require the addition

of a significant number of modes, e.g., those derived from the tangent stiffness matrix eigenvector analysis. This task was not accomplished here because another strategy may be better suited to the capturing of the buckling point and post buckling behavior. Specifically, it is thought at this point that a global-local modeling in the spirit of [25,26] would be a better alternative. The implementation of such a modeling strategy is outside the focus of the present work and is thus left as an open problem.

CHAPTER 7 DETECTION OF STRONGLY NONLINEAR EVENTS

7.1 Detection from the NLROM

Over the last three decades, the analysis of structures undergoing large, nonlinear geometric response by modal-like/reduced order modeling (NLROMs) methods has seen dramatic improvements in state of the art. One of the challenges in applying this methodology is often the appropriateness of the basis used: is it fully appropriate or does it neglect important components of the response? In the latter case, inaccurate predictions are essentially guaranteed. This issue is particularly significant for non-intrusive NLROMs which are constructed from finite element models developed in commercial software. In these situations, the computation of the NLROM solution is completely independent of the full finite element model. Through the development history of these non-intrusive methods, and in Chapter 6 of the present work, the appropriateness of the basis has been assessed by comparing the predictions of the response obtained by the full finite element model and the NLROM. In practice, such a validation strategy is not appropriate, it would defeat the purpose of the construction of the NLROMs to have the full finite element solution.

In this light, one focus of this dissertation is on a preliminary effort to formulate validation strategies of the NLROM predictions that use the least number of calls to the underlying full finite element model. Two situations are envisioned here:

(1) the structural response evolves “smoothly” as a function of time and/or loading which could be showed as in Figure 85(a)

(2) the structural response exhibits instances/segments in which it evolves very rapidly which could be showed as in Figure 85(b), e.g., due to snap-through,

buckling (global or local), symmetry breaking. These segments will henceforth referred to as “events”.

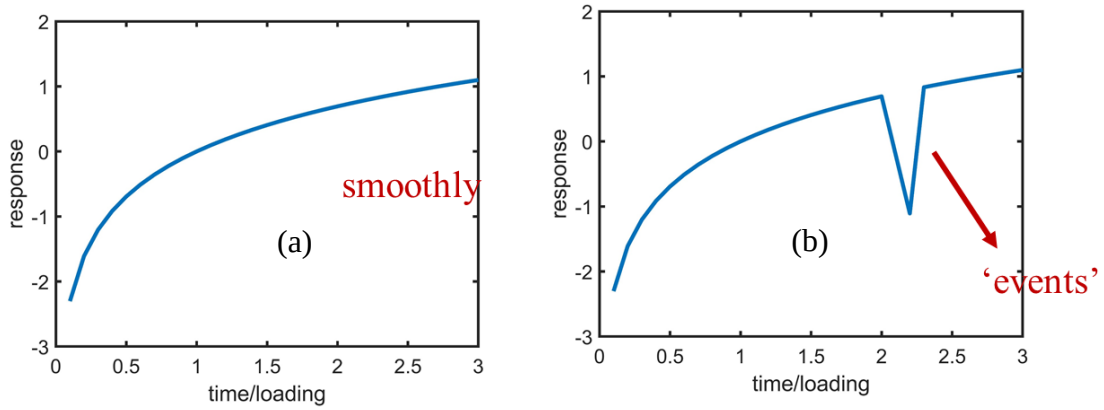

Figure 85. Relation between Response and Time/Loading (a) Smoothly (b)Rapidly

In static problems, a straightforward strategy would be to periodically subject the full finite element model to the loading and compare its response to the one predicted by the NLROM. If the magnitude of the difference is quantified as acceptable the NLROM computation moves on until the next check. Otherwise, the difference vector of the responses could be used as an enrichment to the basis to allow the NLROM to move forward.

The above approach is potentially applicable, although clumsy, in dynamic situations. The inertia and damping terms of the NLROM response could be construed as pseudo forces and combined with the actual loading to create forces that can be applied statically to the finite element model for validation.

Relying on such comparisons to reliably move forward through the set of computations assumes in fact that the evolution of the error will be slow enough, i.e., that situation (1) above is encountered. For situation (2), it is proposed here that the validation

of the NLROM be carried out on the eigenvalues of the tangent stiffness matrix, quantities that can be evaluated in both static and dynamic setting. In fact, an eigenvalue-based assessment would be a useful complement to analyzing responses even in situation (1).

For the curved beam, it is clearly seen from Figure 2 there is a 'jump' of static displacement when snap-through occurs. In this case, the displacement field reflects the 'sharp change' accurately but there are some cases for which displacements are not a good choice to exhibit the event, e.g. consider the hypersonic panel of Figure 6 for which the displacement at the center vs. applied pressure is shown in Figure 80. This curve is quite smooth and does readily point to the local buckling occurring near 5 psi.

Based on the above observations and the work of Chapter 6, it is proposed here to use the eigenvalues of the tangent stiffness matrix for detection of events. Figure 30 and Figure 81 show the eigenvalues vs. load for the clamped-clamped curved beam and the hypersonic panel. On both figures, the 'sharp change' of behavior is clearly seen and the event is detectable.

In this light, one focus of this thesis is on assessing the benefits of monitoring the eigenvalues of the tangent stiffness matrix for

(i) the detection of events and

(ii) the assessment of the NLROM basis to capture the response through the event.

This effort will be carried out on the curved shell of [32], see Figure 4, as it approaches symmetry breaking occurrences in dynamic simulations and on the clamped-

clamped curved beam of [42], see Figure 1, as it snap-through. These analyses will rely on NLROMs developed in Chapter 6.

Consider first the curved shell of Figure 4 under an acoustic loading of 170dB OASPL found in Chapter 6 to exhibit a symmetry breaking which is a bifurcation and thus should exhibit a vanishing first eigenvalue of the Nastran tangent stiffness matrix. To confirm this occurrence, some time intervals were first identified during which the asymmetry of the response, outputted at only a few symmetrically located nodes for time and storage efficiency, seemed to start/rapidly increase. Full field displacement data was then generated at every time step during those time intervals. Finally, these displacement fields were reimposed statically to the finite element model one by one and the corresponding Nastran tangent stiffness matrices outputted. The analysis of their eigenvalues, carried out of core with Matlab, did indeed yield some small negative values as seen in Figure 86.

The next question was then to ascertain whether the eigenvalues of the NLROM tangent stiffness matrix would also vanish. This check was performed at both 160dB and 170dB, see Figure 87. At 160dB, it is found that the lowest eigenvalue does dip below zero on a very limited number of occasions while such occurrences are quite continuous at 170dB. These observations indicate first and foremost that the NLROM does predict the occurrence of a change in response through a vanishing of the tangent stiffness eigenvalues. It does predict it to occur at 160dB, at too low a level, but the rare occurrence of the negative eigenvalues for that loading vs. at 170dB suggests that it is marginally present.

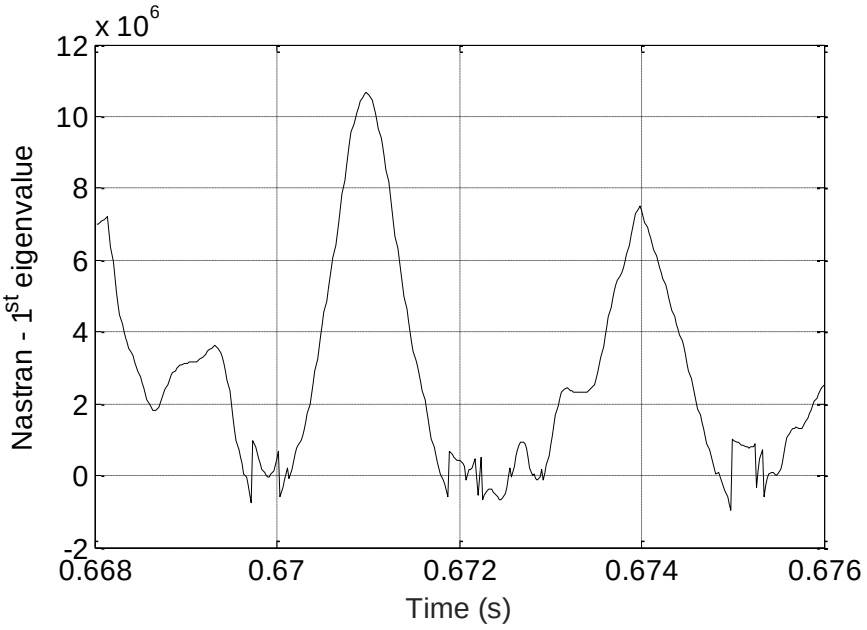

Figure 86. Lowest Eigenvalue of the Nastran Tangent Stiffness Matrix. Curved Shell, Dynamic Excitation of OASPL 170dB.

To use this information efficiently, it is proposed here that a check of the eigenvalues of the NLROM with those of Nastran be done punctually for displacement fields such that the NLROM predicts a negative lowest eigenvalue as well as for neighboring time steps where the eigenvalue is notably positive, see Figure 88 for the comparison of eigenvalues when the NLROM one is negative at 160dB.

The planned use of this data is as follows. If the accuracy of the NLROM eigenvalues in comparison with the Nastran ones is good, or similar, for both positive and negative cases, it would then be concluded that the strongly nonlinear event (bifurcation, snap-through, buckling, etc.) predicted by the NLROM is genuine. If the accuracy is dissimilar, i.e., good for the positive case, less so for the negative one, it would then be concluded that the strongly nonlinear event may not be occurring. However, the presence

of negative eigenvalues of the NLROM and of Nastran for those displacements would be indicative that the occurrence of the event is near.

The second scenario is observed in connection with the NLROM data at 160dB. As seen from Figure 88, the eigenvalues of the NLROM tangent stiffness matrix and their Nastran counterparts do not match well for the negative occurrence of the former. However, the matching is significantly better for the positive occurrences and improving as the magnitude of the eigenvalue increases. This increased accuracy of the eigenvalues away from zero suggests that the NLROM response is accurate except during the occurrence of near or below zero eigenvalues. This tentative conclusion is actually correct as demonstrated by the good match of the power spectral densities of the Nastran and NLROM responses at 160dB, see [50]. The poor matching of the near zero eigenvalues confirms the finding that the bifurcation is not correctly predicted, it does not happen for Nastran at 160dB but will happen at a slightly higher level.

Further validation of the above observations can be drawn from the clamped-clamped curved beam of Figure 1 which is shown in Figure 89. Since the NLROM provides an excellent match of the Nastran response through the snap-through, it would be expected that the NLROM eigenvalues and their Nastran counterparts would closely match each other for both positive and negative eigenvalues. This is indeed what Figure 89 demonstrates. Note, however, that the most negative eigenvalues are not as well captured as the other ones.

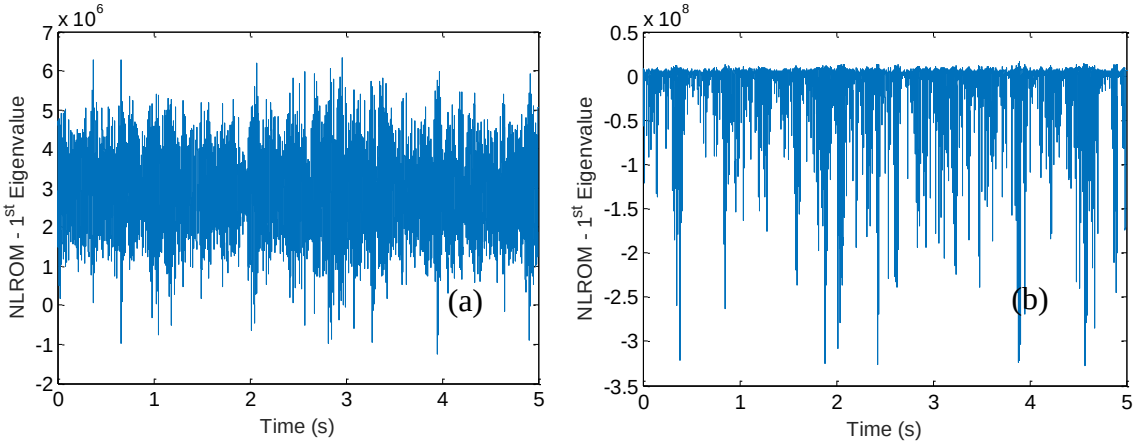

Figure 87. First Eigenvalues of the NLROM Tangent Stiffness Matrix vs. Time. Curved Shell OASPL Of (a) 160db, (b) 170db.

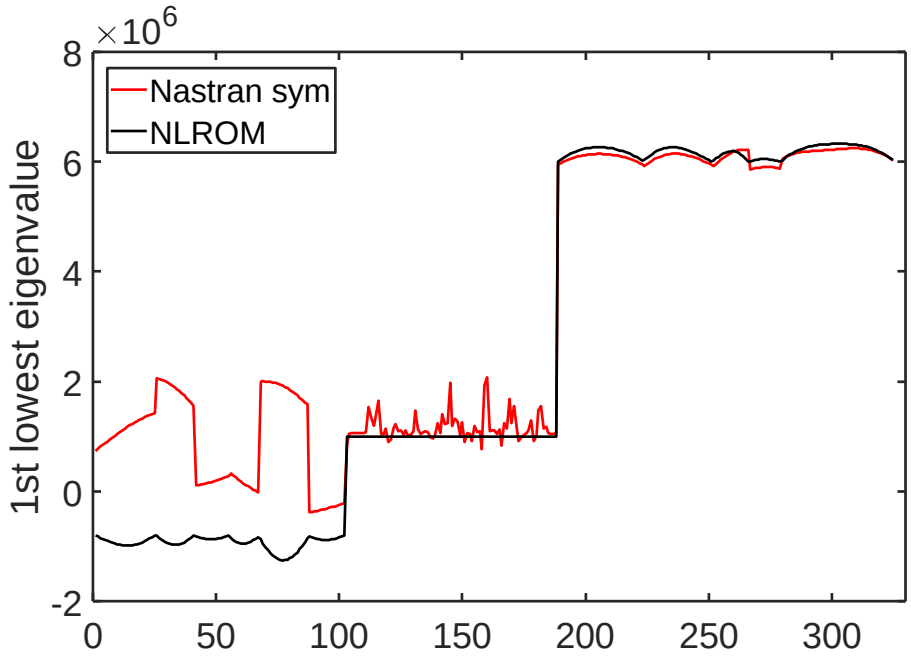

Figure 88. Lowest Eigenvalues of the Tangent Stiffness Matrix, Nastran and NLROM, when the Latter One is Negative, Curved Shell at OASPL 160db.

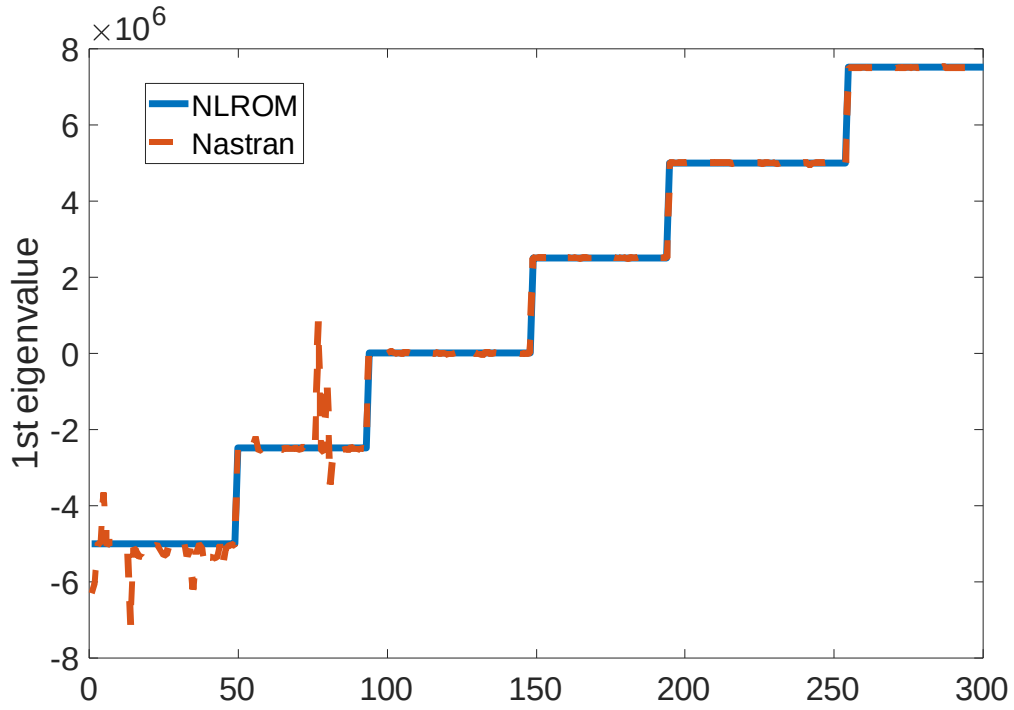

Figure 89. Comparison of Lowest Eigenvalues of the Nastran and NLROM Tangent Stiffness Matrices for NLROM Deformations Corresponding to Specific Sets of NLROM Eigenvalues. Clamped-Clamped Curved Beam.

With regard to the cylindrical panel, it is worthwhile to recognize that, hypothetically, the symmetry breaking might have influenced only the eigenvalues of the antisymmetric modes. In that case, it would have been unobserved in the NLROM since this model only includes the symmetric ones. It is not clear whether such a situation is possible or not but ultimately the split of modes into symmetric and antisymmetric only occurs for structures with high degree of symmetry which are typically not observed in real structures for which events such as snap-through and buckling would involve many of the low frequency linear modes.

7.2 Detection from Dual Construction Data

The discussion of the previous section has focused on detecting the occurrence of strongly nonlinear events from a NLROM, i.e., with a basis that represents well the response of the structure up to and including the event. The study of the hypersonic panel in Chapter 6 has demonstrated that some events may not be captured by the basis and thus would not be detected using the strategy of the previous section.

Accordingly, it was questioned what data could be used to detect such events and more specifically data that is already used in the construction of the NLROM. Of particular interest here are the static responses generated for the construction of the duals as they span a range of displacement levels. Shown in Figure 90 are the displacements of the hypersonic panel center vs. the load magnitude induced by the loading corresponding to the 1-1, 1-2, and 1-3 combinations. While none of these curves indicate the presence of the local buckling, this is consistent with the discussion of Chapter 6, e.g., Figure 73, that the displacements - at that location at least - are not sensitive to the buckling and that the eigenvalues of the tangent stiffness matrix should instead be investigated.

Then, shown in Figure 91 at the lowest three eigenvalues of the tangent stiffness matrices corresponding to the displacements of Figure 90. As observed with the uniform load, a sharp drop of the eigenvalues is observed mostly for the 2nd and 3rd eigenvalues that could be associated with the occurrence of local buckling in that data. To confirm this potential, shown in Figure 92-Figure 93 are selected eigenvectors of these tangent stiffness matrices and it is seen that some of these, more specifically the eigenvectors associated

with the 1-1 combination shown on Figure 92, exhibit the pattern of deflection on the stiffener that is consistent with the local buckling, see Figure 75 and Figure 77.

If these eigenvectors are indeed indicative of the local buckling, then enriching the 3T8D basis with them should improve the capturing of the dip of the Nastran tangent stiffness eigenvalue observed in Figure 81. Specifically, the three eigenvectors of the most 2 negative load factor of combination 1-1, most 3 negative load factor of combination 1-2 and combination 1-3, 24 eigenvectors in total, were appended to the model 3T8D. Then, the lowest eigenvalue of the Nastran tangent stiffness projected on this basis was plotted, see in Figure 95. It is seen in this figure that the enriched basis does notably better in predicting the Nastran eigenvalue, not only the onset of the dip but also the beginning of the decreasing value phase.

The above results demonstrate that the occurrence of the local buckling can indeed be detected from the data generated for the duals, more specifically the eigenvalues of the tangent stiffness matrix, and that the corresponding eigenvectors may produce worthwhile enrichments of the basis to capture the post event behavior.

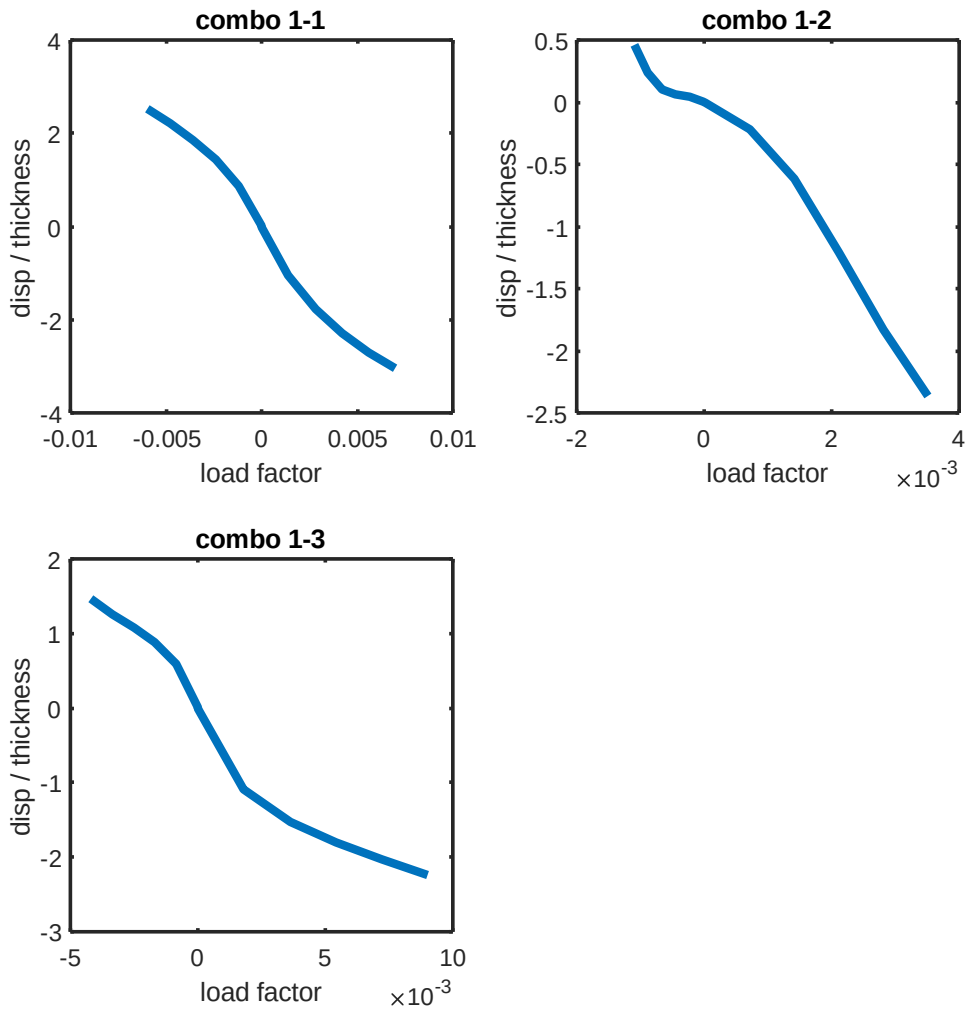

Figure 90 Transverse Deflection at the Center of the Hypersonic Panel vs. Load Factor Generated for the Construction of the 1-1, 1-2, and 1-3 Duals.

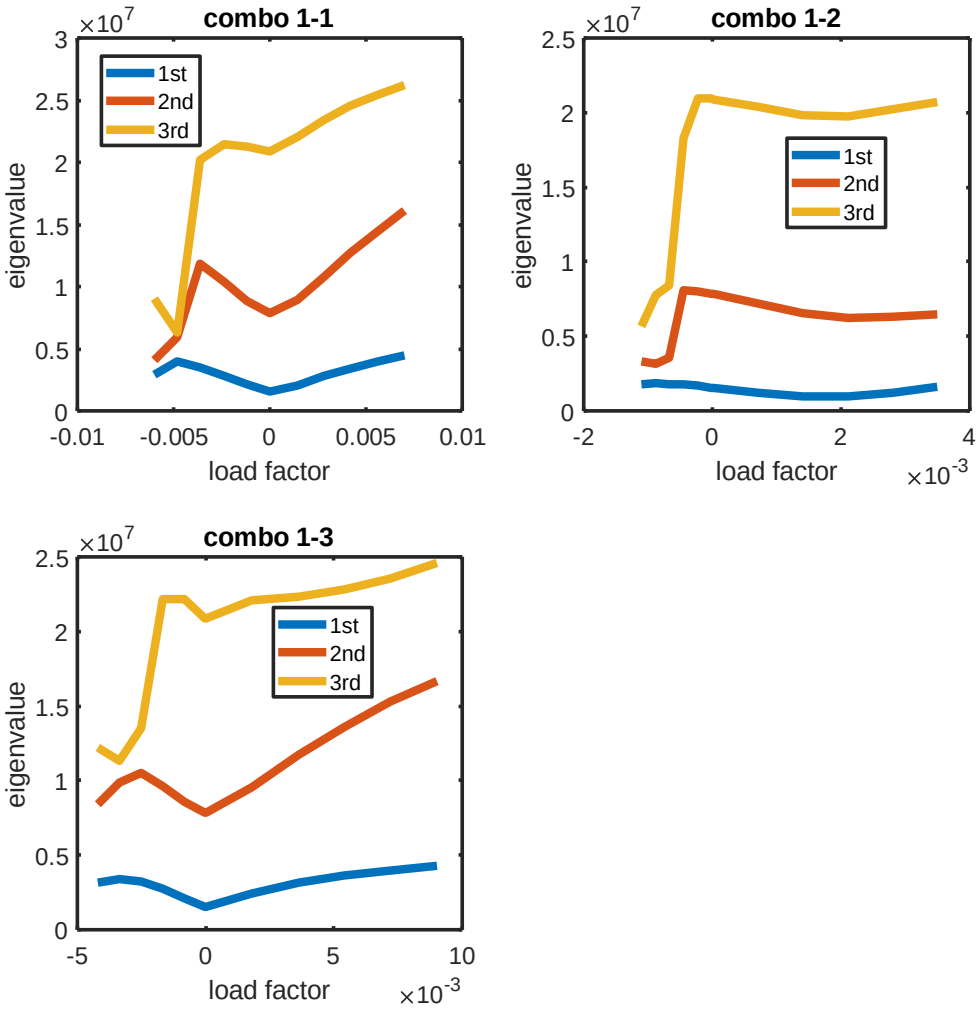

Figure 91. Eigenvalues of the Tangent Stiffness of the Hypersonic Panel vs. Load Factor Generated for the Construction of the 1-1, 1-2, and 1-3 Duals.

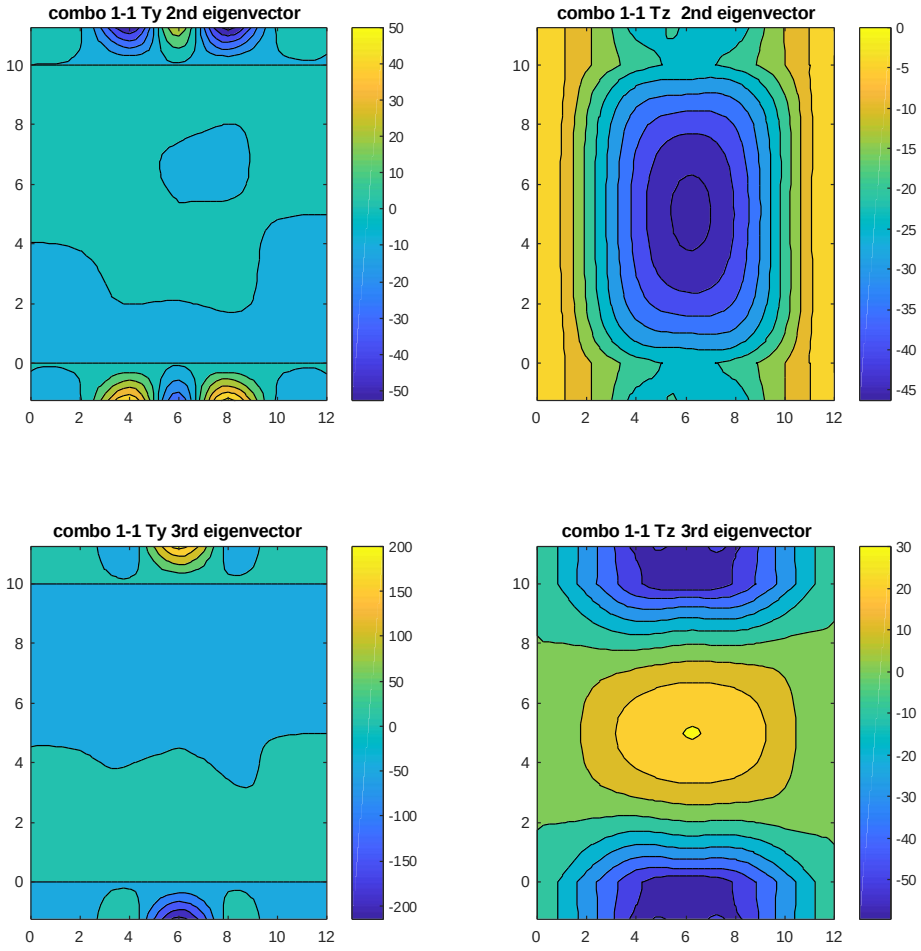

Figure 92. Selected Eigenvectors of the Tangent Stiffness of the Hypersonic Panel vs. Load Factor Generated for the Construction of the 1-1 Duals.

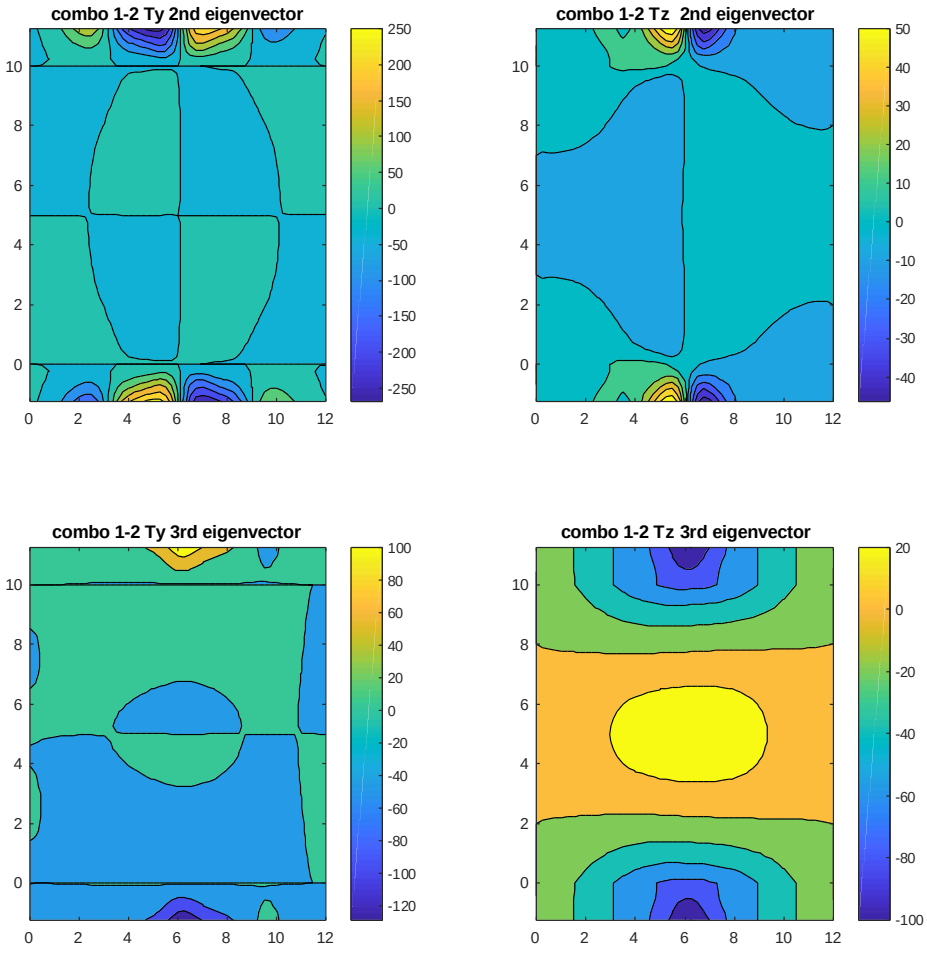

Figure 93. Selected Eigenvectors of the Tangent Stiffness of the Hypersonic Panel vs. Load Factor Generated for the Construction of the 1-2 Duals.

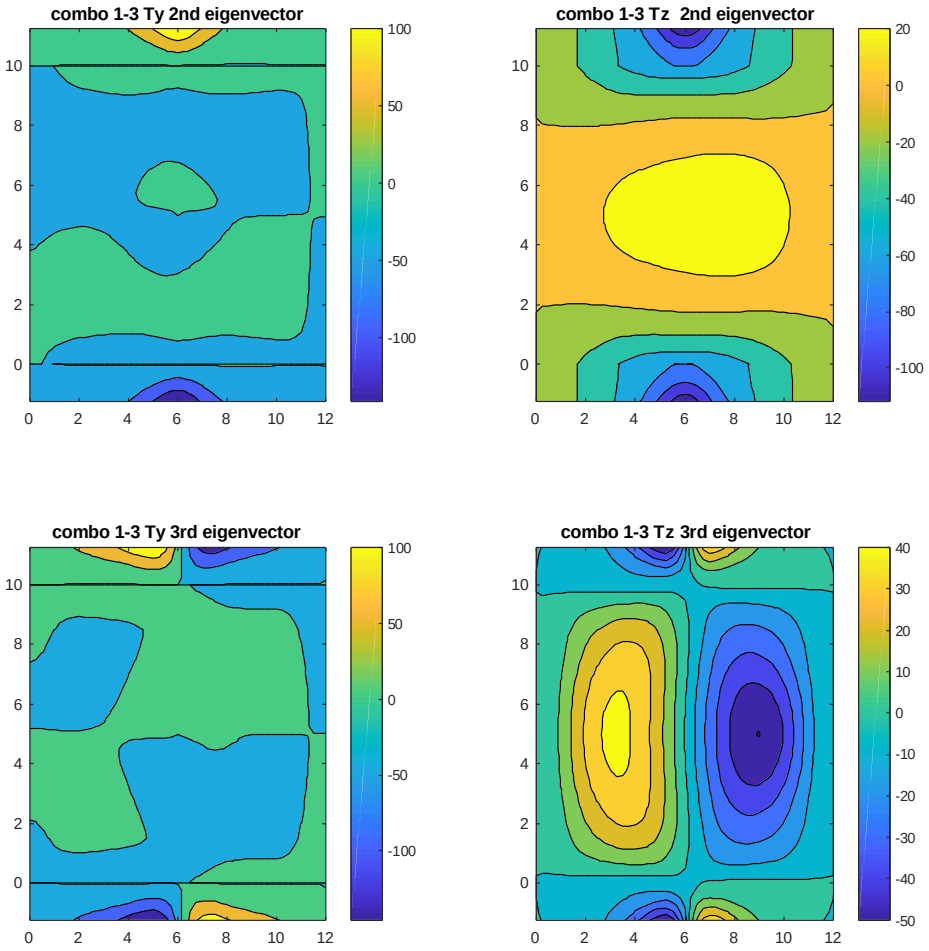

Figure 94. Selected Eigenvectors of the Tangent Stiffness of the Hypersonic Panel vs. Load Factor Generated for the Construction of the 1-3 Duals.

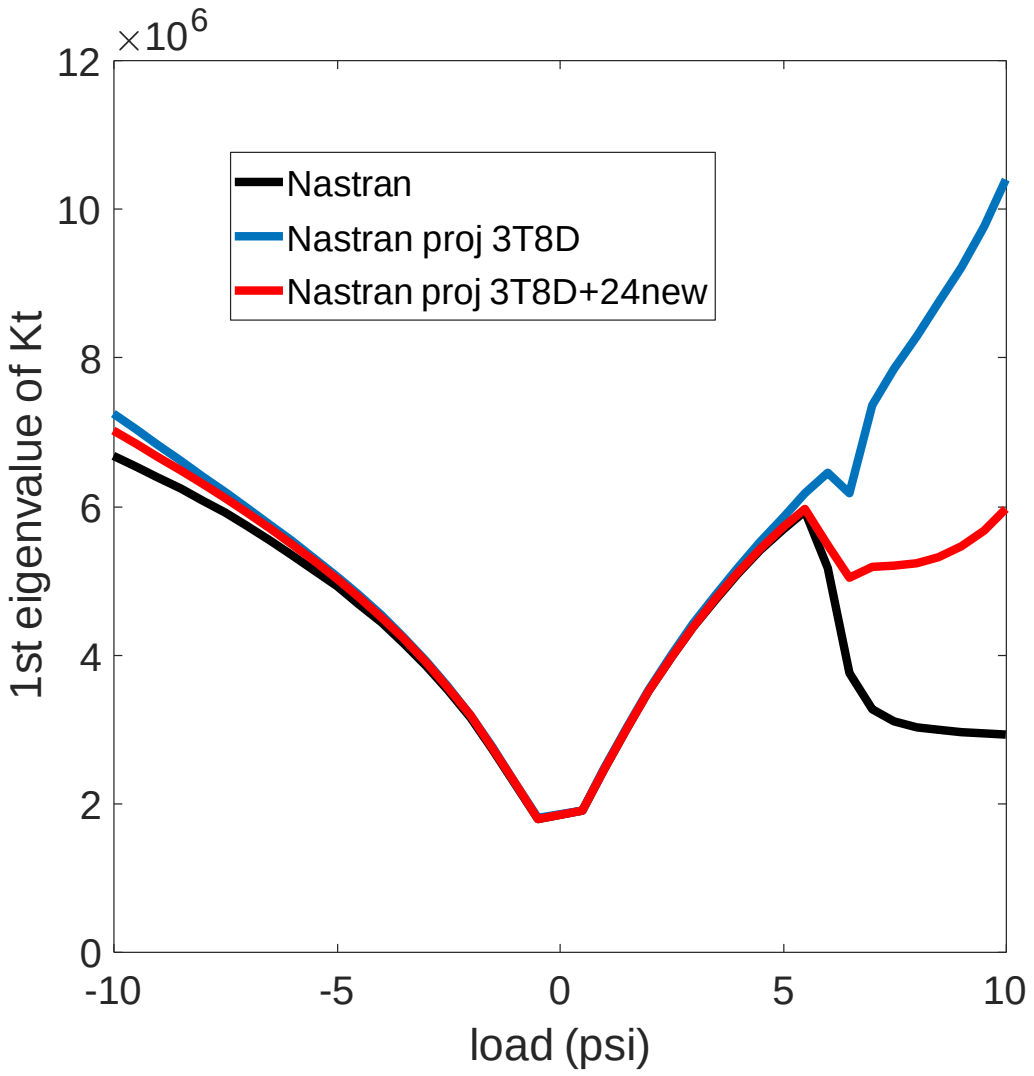

Figure 95. Lowest Eigenvalue of the Tangent Stiffness Matrix vs. Uniform Applied Pressure on Skin. Effect of Enriching the Basis with Dual Data Based Eigenvectors.

CHAPTER 8 SUMMARY & RECOMMENDATION FOR FUTURE WORK

The focus of the present investigation was on understanding and resolving the difficulties encountered in the past when constructing nonlinear reduced order models of structures exhibiting strongly nonlinear features, most notably the clamped-clamped curved beam, the shallow cylindrical shell, and the representative hypersonic panel.

Central to the present effort is the assertion that better predictions by the NLROM are obtained when the number of basis functions that have large components is as small as possible. For the linear part of the basis, this assumption is consistent with the current state of the art of NLROMs at ASU, most of the models considered so far have had one dominant linear mode and the predictions have been very good to excellent. When multiple linear modes are dominant, achieving similarly accurate predictions has been more challenging or not achieved.

It is believed that this correlation stems from two challenges of NLROM constructions. The first is the basis selection and most notably the determination of the duals which complement the linear modes to form the basis. This process is very straightforward when a single linear mode dominates the response but becomes more challenging when two or more modes play a key role owing to the need to create a set of loadings that induce displacements fields that are representative of the likely variable combination of dominant linear modes. The second challenge relates to the identification of the nonlinear stiffnesses. Specifically, having multiple dominant linear modes also implies that there exists a much larger number of stiffness coefficients that have an

important effect on the magnitude of the restoring forces, in particular, coefficients involving indices corresponding to multiple modes.

Based on the above assertion and observations, an optimization of the basis was defined seeking to concentrate the response on a small subset of modes. For the linear part of the basis, this effort was accomplished using a set of finite element static displacements obtained under relevant loading conditions, referred to as the reference data. These displacements fields are first projected on a series of linear modes and these projections are processed through a Proper Orthogonal Decomposition to determine the most significant combinations of linear modes in the response. Then, the eigenvector(s) with the largest eigenvalue(s) is (are) retained and their full finite element space counterpart determined. This (these) mode(s) then form the core of the linear basis. To this core are finally added the rest of the linear modes which are further orthogonalized. This process was shown to be very efficient in connection with the curved beam, the cylindrical shell and the hypersonic panel, leading to linear modes that very well represented the response.

An optimization of the dual modes was also proposed motivated by the desire to concentrate the response in a small number of modes to improve the identification/stability of the NLROM but also to address situations observed in the past where the number of dual modes necessary was unusually large (e.g., more than twice the number of linear modes). This effort was not carried out on the reference data used for the linear modes to avoid a bias of the model to this data. Rather, it was carried out using the identified stiffness coefficients seeking more specifically the linear combinations of the duals that maximize the coupling with the linear basis as measured by the dominant quadratic stiffness terms.

The combination of the above basis optimization schemes led to NLROMs of the clamped-clamped curved beam and the shallow cylindrical shell that provided the best and most stable predictions of the Nastran results of all attempts previously made for these models at ASU. These results demonstrate the validity of the starting assertion, i.e., that better predictions by the NLROM are obtained when the number of basis functions that have large components is as small as possible. The quality of the match of the NLROM predictions with their Nastran counterparts was generally excellent even in strongly nonlinear events. Moreover, the NLROMs were very compact, i.e., with small number of modes and coefficients, implying fast NLROM computations.

Next, the identification of the nonlinear stiffness coefficients was revisited. A key focus was to provide solid data regarding the accuracy of the coefficients identified from Nastran. To this end, the clamped-clamped curved beam was also modeled within an open source finite element code from the AFRL and the nonlinear stiffness coefficients associated with the basis derived from Nastran were identified. The comparison of the AFRL code and Nastran identified coefficients provided clear support for the long-held perspective that a series of nonlinear coefficients identified from Nastran are not reliable, a conclusion also supported by checking the applicability of the symmetry relations linking these coefficients.

Having determined what sets of nonlinear stiffness coefficients are reliably identified, several different remedies can be envisioned. In the absence of data for the structure considered, one approach is to proceed with the coefficients as identified. A second option is to zero out the coefficients which are deemed poorly identified. This is

the “cleaning” option that has occasionally been performed in the past. This option traditionally improves the stability of the NLROM for dynamic computations and has often improved predictions because many of the coefficients which are eliminated contribute little to the response. Yet, for structures such as the clamped-clamped curved beam with very large deflections, it is necessary to have a NLROM with a more complete set of nonlinear stiffness to obtain an accurate prediction, especially of the post snap-through behavior. In such situations, a third option is developed here to refine the nonlinear stiffness coefficients deemed inaccurate. In fact, two different approach of “fine tuning” of the NLROM stiffness coefficients were also devised and employed in connection with the curved beam to obtain the excellent results presented. The need to carry this effort stems from the high sensitivity of the NLROM response to some of the coefficients. A first tuning approach based on the matching of modal forces was shown to bring a significant improvement in the validation results, especially under static loading. However, such tuned NLROMs may not be stable enough under dynamic loading to give converged results. This is because some stiffness coefficients have been tuned to a value far away from their “correct” values although the error of modal forces calculated from them is small. The second tuning approach was devised to avoid that problem. It is based on the matching of the generalized displacements q_i computed by Nastran and the NLROM. This tuning approach was found to be better than the first one yielding stable NLROMs.

Another key question for this investigation is the “on-line” assessment of the NLROM, i.e., to determine whether it is accurately capturing the response that would be predicted by the underlying finite element model/software. A strategy to carry out this

effort minimizing the number of calls to the full finite element code is proposed here. Preliminary results were presented to suggest in particular that the monitoring of the eigenvalues of the NLROM tangent stiffness matrix and of the occurrence of zeros of the lowest one provide a framework to (i) predict strongly nonlinear events (snap-throughs, buckling, solution changes) and (ii) assess whether they are accurately predicted.

The work carried out during this investigation has demonstrated that:

(1) the monitoring of the NLROM tangent stiffness eigenvalues provides an approach to detect strongly nonlinear "events" such as symmetry breaking, snap-throughs, and global buckling that exhibit a zero eigenvalue of the tangent stiffness matrix,

(2) the accuracy of the prediction of the load (static or dynamic) at which the event occurs can be ascertained by comparing the eigenvalues of the NLROM tangent stiffness matrix and its Nastran equivalent obtained for the same deflection.

Based on the above findings, future work in NLROMs should focus on the following issues.

(1) The continuation of improvements in the identification of the nonlinear stiffness coefficients. The modal displacement tuning approach has performed well but is computationally demanding especially when the number of modes becomes large. A first possible avenue for improvement is to identify the nonlinear coefficients by separate batches. Those which are currently well identified stay identified as is. The next batch would be identified under displacement

conditions which fit more closely the behavior of the beam. For example, complex displacements of the structure corresponding to linear combinations of the linear modes only are not very physical. Significant membrane effects should accompany these motions. Adding them, based on the first batch of identified coefficients, would likely lead to more "physical", lower strain certainly, displacements. It is thought that the identified values of the second batch of nonlinear stiffness coefficients may then be improved.

(2) A second avenue to improve the identification process would be to develop/use an open source nonlinear finite element code that lead to identification issues similar to those experienced with Nastran. From limited observations, it is believed that a corotational formulation may lead to similar problems. If so, then efforts could be focused on (i) mathematically clarifying the issue and (ii) if possible, develop formulation-based "correction" methods that transform the poorly identified coefficients into more reliable ones.

(3) Revisit the hypersonic panel and the prediction of its behavior post local buckling. As stated in Chapter 6, a possible option is to use the global-local methodology adapted to NLROM using the current global modes but enriching the basis near the buckling zone by local modes. Past applications of this global-local approach have focused on accounting for local defects (notch, crack) which are not present here so that the approach would need to be modified. While this approach would still necessitate a prior knowledge that a local

buckling would take place, it would provide a systematic framework (vs. the ad-hoc enrichment approach attempted here) to capture these local events. Considering that many hypersonic panels have stiffeners, sometimes many of them, it is believed that this line of work is important for future, practical applications.

REFERENCES

[1] M.I. McEwan, J.R. Wright, J.E. Cooper, A.Y.T. Leung, A combined modal/finite element analysis technique for the dynamic response of a non-linear beam to harmonic excitation, Journal of Sound and Vibration, Vol. 243 (4), pp. 601-624, 2001.

[2] M.P. Mignolet, A. Przekop, S.A. Rizzi, and S.M. Spottswood, A Review of Indirect/Non-Intrusive Reduced Order Modeling of Nonlinear Geometric Structures, Invited Paper, Journal of Sound and Vibration, Vol. 332, No. 10, pp. 2437-2460, 2013.

[3] J.J. Hollkamp, R.W. Gordon, S.M. Spottswood, Nonlinear modal models for sonic fatigue response prediction: a comparison of methods, Journal of Sound and Vibration 284 (2005) 1145 - 1163.

[4] M.P. Mignolet, A.G. Radu, and X. Gao, Validation of Reduced Order Modeling for the Prediction of the Response and Fatigue Life of Panels Subjected to Thermo-Acoustic Effects, Proceedings of the 8th International Conference on Recent Advances in Structural Dynamics, Southampton, United Kingdom, Jul. 14-16, 2003.

[5] K. Kim, A. Radu, X.Q. Wang, M.P. Mignolet, Nonlinear reduced order modeling of isotropic and functionally graded plates, International Journal of Non-Linear Mechanics, Vol. 49, pp. 100-110, 2013.

[6] A. Przekop, S.A. Rizzi, Dynamic snap-through of thin-walled structures by a reduced-order method, AIAA Journal, Vol. 45, pp. 2510-2519, 2007.

[7] A. Przekop, S.A. Rizzi, Nonlinear reduced order finite element analysis of structures with shallow curvature, AIAA Journal, Vol. 44, pp. 1767-1778, 2006.

[8] A. Przekop, X. Guo, S.A. Rizzi, Alternative modal basis selection procedures for nonlinear random response simulation, Journal of Sound and Vibration, 331 (2012) 4005-4024.

[9] S.A. Rizzi, A. Przekop, System identification-guided basis selection for reduced-order nonlinear response analysis, Journal of Sound and Vibration 315 (2008) 467-485.

[10] A. Przekop, S.A. Rizzi, Nonlinear Acoustic Response of an Aircraft Fuselage Sidewall Structure by a Reduced-Order Analysis, Proceedings of the 9th International Conference on Recent Advances in Structural Dynamics, Southampton, UK, 17-19 July 2006.

[11] R.A. Perez, X.Q. Wang, and M.P. Mignolet, Non-Intrusive Structural Dynamic Reduced Order Modeling for Large Deformations: Enhancements for Complex Structures, Journal of Computational and Nonlinear Dynamics, Vol. 9, No. 3, pp. 031008-1 - 031008-12, 2014.

[12] M.P. Mignolet, C. Soize, C., Stochastic reduced order models for uncertain geometrically nonlinear dynamical systems, Computer Methods in Applied Mechanics and Engineering 197 (2008) 3951-3963.

[13] X.Q. Wang, R. Perez, M.P. Mignolet, R. Capillon, and C. Soize, C., Nonlinear Reduced Order Modeling of Complex Wing Models, Proceedings of the 54th Structures, Structural Dynamics and Materials Conference, Apr. 8-11, 2013, Boston, Massachusetts, AIAA Paper AIAA-2013-1520.

[14] X.Q. Wang, M.P. Mignolet, and C. Soize, Nonlinear Geometric Modeling of Uncertain Structures through Nonintrusive Reduced Order Modeling, Proceedings of the Eighth International Conference On Computational Stochastic Mechanics, Paros, Greece, Jun. 10-13, 2018.

[15] A.A. Muravyov, S.A. Rizzi, Determination of nonlinear stiffness with application to random vibration of geometrically nonlinear structures, Computers and Structures, 81 (2003) 1513-1523.

[16] K. Kim, V. Khanna, X.Q. Wang, M.P. Mignolet, Nonlinear reduced order modeling of flat cantilevered structures, Proceedings of the 50th Structures, Structural Dynamics, and Materials Conference, Palm Springs, California, May 2009. AIAA-2009-2492.

[17] X.Q. Wang, J. Lin, B.A. Wainwright, and M.P. Mignolet, Multiple-Level Identification of Stiffness Coefficients in Nonlinear Reduced Order Modeling, Proceedings of the International Modal Analysis Conference, IMAC XXXVII, Orlando, Florida, Jan. 28-31, 2019.

[18] S.M. Spottswood, R.J. Allemang, On the investigation of some parameter identification and experimental modal filtering issues for nonlinear reduced order models, Experimental Mechanics 47 (2007) 47 511–521.

[19] Y. Wang, X.Q. Wang, and M.P. Mignolet, Component-Centric Reduced Order Modeling for the Prediction of the Nonlinear Geometric Response of a Part of a Stiffened Structure, Journal of Computational and Nonlinear Dynamics, Vol. 13, pp. 121006-1 – 121006-12, 2018.

[20] A. Gogulapati, K. Brouwer, X.Q. Wang, R. Murthy, J.J. McNamara, and M.P. Mignolet, Full and Reduced Order Aerothermoelastic Modeling of Built-Up Aerospace Panels in High-Speed Flows, Proceedings of the AIAA Science and Technology Forum and Exposition (SciTech2017), Dallas, Texas, Jan. 9-13, 2017, AIAA Paper AIAA 2017-0180.

[21] A. Gogulapati, R. Deshmukh, J.J. McNamara, V. Vyas, X.Q. Wang, M.P. Mignolet, T. Beberniss, S.M. Spottswood, and T.G. Eason, Response of a Panel to Shock Impingement: Modeling and Comparison with Experiments - Part 2, Proceedings of the AIAA Science and Technology Forum and Exposition (SciTech2015), Orlando, Florida, Jan. 5-9, 2015, AIAA Paper AIAA 2015-0685.

[22] A. Gogulapati, R. Deshmukh, A.R. Crowell, J.J. McNamara, V. Vyas, X.Q. Wang, M.P. Mignolet, T. Beberniss, S.M. Spottswood, and T.G. Eason, Response of a Panel to Shock Impingement: Modeling and Comparison with Experiments, Proceedings of the AIAA Science and Technology Forum and Exposition (SciTech2014), National Harbor, Maryland, Jan. 13-17, 2014, AIAA Paper AIAA 2014-0148.

[23] R. Perez, X.Q. Wang, M.P. Mignolet, Steady and unsteady nonlinear thermoelastodynamic response of panels by reduced order models, Proceedings of the 51st Structures, Structural Dynamics, and Materials Conference, Orlando, Florida, April 2010, AIAA-2010-2724.

[24] R.A. Perez, X.Q. Wang, and M.P. Mignolet, Prediction of Displacement and Stress Fields of a Notched Panel with Geometric Nonlinearity by Reduced Order Modeling, Journal of Sound and Vibration, Vol. 333, pp. 6572-6589, 2014.

[25] X.Q. Wang, G.P. Phlipot, R.A. Perez, and M.P. Mignolet, Locally Enhanced Reduced Order Modeling for the Nonlinear Geometric Response of Structures with Defects, International Journal of Non-Linear Mechanics, Vol. 101, pp. 1-7, 2018.

[26] X.Q. Wang, P.J. O'Hara, M.P. Mignolet, and J.J. Hollkamp, J.J., Reduced Order Modeling with Local Enrichment for the Nonlinear Geometric Response of a Cracked Panel, AIAA Journal, , Vol. 57, No. 1, pp. 421-436, 2019.

[27] A. Matney, S.M. Spottswood, M.P. Mignolet, Nonlinear Structural Reduced Order Modeling Methods for Hypersonic Structures, Proceedings of the 53rd Structures, Structural Dynamics and Materials Conference, Honolulu, Hawaii, April 2012, AIAA-1972.

[28] R. Perez, X.Q. Wang, M.P. Mignolet, Nonlinear reduced order models for thermoelastodynamic response of isotropic and FGM panels, AIAA Journal 49 (2011) 630-641.

[29] A. Matney, R. Perez, M.P. Mignolet, Nonlinear unsteady thermoelastodynamic response of a panel subjected to an oscillating flux by reduced order models, Proceedings of the 52nd Structures, Structural Dynamics and Materials Conference, Denver, Colorado, April 2011, AIAA 2011-2016.

[30] A.K. Matney, M.P. Mignolet, S.M. Spottswood, A.J. Culler, and J.J. McNamara, Thermal Reduced Order Model Adaptation to Aero-Thermo-Structural Interactions, Proceedings of the AIAA Science and Technology Forum and Exposition (SciTech2014), National Harbor, Maryland, Jan. 13-17, 2014, Paper AIAA 2014-0493.

[31] A. Matney, M.P. Mignolet, A.J. Culler, J.J. McNamara, and S.M. Spottswood, Panel Response Prediction through Reduced Order Models with Application to Hypersonic Aircraft, Proceedings of the AIAA Science and Technology Forum and Exposition (SciTech2015), Orlando, Florida, Jan. 5-9, 2015, AIAA Paper AIAA 2015-1630.

[32] R.W. Gordon and J.J. Hollkamp, Reduced-Order Models for Acoustic Response Prediction of a Curved Panel, Proceedings of the 52nd AIAA/ASME/ASCE/AHS/ASC Structures, Structural Dynamics and Materials Conference, Denver, Colorado, April 4-7 2011, AIAA Paper AIAA 2011-2081.

[33] J.J. Hollkamp, and R.W. Gordon, Application of Reduced-Order Models for Thermoelastic Trajectory Simulation, Proceedings of the 53rd Structures, Structural Dynamics and Materials Conference, Honolulu, Hawaii, April 2012, AIAA-1550.

[34] E. Capiez-Lernout, C. Soize, and M.P. Mignolet, Post-buckling nonlinear static and dynamical analyses of uncertain cylindrical shells and experimental validation, Computer Methods in Applied Mechanics and Engineering, Vol. 271, pp. 210-230, 2014.

[35] P. Song, X.Q. Wang, A. Matney, R. Murthy, M.P. Mignolet, Nonlinear Geometric Thermoelastic Response of Structures with Uncertain Thermal and Structural Properties, Proceedings of the AIAA Science and Technology Forum and Exposition (SciTech2017), Dallas, Texas, Jan. 9-13, 2017, AIAA Paper AIAA 2017-0181.

[36] R.J. Kuether, M.S. Allen, J.J. Hollkamp, Modal Substructuring of Geometrically Nonlinear Finite-Element Models, AIAA Journal Vol. 54 (2), pp. 691-702, 2016.

[37] R.J. Kuether, M.S. Allen, J.J. Hollkamp, Modal Substructuring of Geometrically Nonlinear Finite Element Models with Interface Reduction, AIAA Journal, Vol. 55 (5), pp. 1695-1706, 2017

[38] Y. Wang, and M.P. Mignolet, Component-Centric Reduced Order Modeling of the Dynamic Response of Linear Multibay Structures, Journal of Vibration and Acoustics, Vol. 139, 041007, 2017.

[39] J.J. Hollkamp, R. Gordon, Coupling acoustic modal models to nonlinear structural reduced- order models, Proceedings of the 51st Structures, Structural Dynamics, and Materials Conference, Orlando, Florida, April 2010, AIAA-2010-2542.

[40] R.W. Gordon, J.J. Hollkamp, Coupled Structural-Acoustic Response Prediction with Complex Modal Models, Proceedings of the 50th Structures, Structural Dynamics and Materials Conference, Schaumburg, Illinois, May 2009, AIAA-2009-2307.

[41]Vyas, V., X.Q. Wang, Jain, A., and M.P. Mignolet, Nonlinear Geometric Reduced Order Model for the Response of a Beam with a Piezoelectric Actuator, Proceedings of the AIAA Science and Technology Forum and Exposition (SciTech2015), Orlando, Florida, Jan. 5-9, 2015, AIAA Paper AIAA 2015-0692.

[42] S.M. Spottswood, T.G. Eason, X.Q. Wang, M.P. Mignolet, Nonlinear reduced order modeling of curved beams: a comparison of methods, Proceedings of the 50th Structures, Structural Dynamics, and Materials Conference, Palm Springs, California, May 2009, AIAA-2009-2433.

[43] A. Culler, J. McNamara, Impact of Fluid-Thermal-Structural Coupling on Response Prediction of Hypersonic Skin Panels, AIAA Journal, Vol. 49, pp 2393-2406, 2011.

[44] G. Phlipot, X.Q. Wang, M.P. Mignolet, L. Demasi, and R. Cavallaro, Nonintrusive Reduced Order Modeling for the Nonlinear Geometric Response of Some Joined Wings, Proceedings of the AIAA Science and Technology Forum and Exposition (SciTech2014), National Harbor, Maryland, Jan. 13-17, 2014, AIAA Paper AIAA 2014-0151

[45] P. Song, X.Q. Wang, and M.P. Mignolet, Nonlinear Reduced ROMs: Formulation and Applications, Proceedings of the AIAA Science and Technology Forum and Exposition (SciTech2019), San Diego, California, Jan.7-11, 2019.

[46] R. Murthy, X.Q. Wang, A. Matney, and M.P. Mignolet, A Construction of Thermal Basis Functions for Coupled Structural - Thermal Reduced Order Models, Proceedings of the AIAA Science and Technology Forum and Exposition (SciTech2017), Dallas, Texas, Jan. 9-13, 2017, AIAA Paper AIAA 2017-0179.

[47] R.A. Perez, B.P. Smarslok, and M.P. Mignolet, Deterministic and Stochastic Partial Linearization Approach for Nonlinear Reduced Order Models of Structures, Proceedings of the AIAA Science and Technology Forum and Exposition (SciTech2015), Orlando, Florida, Jan. 5-9, 2015, AIAA Paper AIAA 2015-2052.

[48] Y.-W. Chang, X.Q. Wang, E. Capiez-Lernout, M.P. Mignolet, C. Soize, Reduced order modeling for the nonlinear geometric response of some curved structures, Proceedings of the 2011 International Forum of Aeroelasticity and Structural Dynamics, June 2011, Paris, France, IFASD-2011-185.

[49] Lin, J., Wang, X.Q., and Mignolet, M.P., "Nonlinear Reduced Order Modeling of Strongly Nonlinear Behavior: A Revisit of a Curved Beam Example," *Proceedings of the International Modal Analysis Conference, IMAC XXXVI*, Orlando, Florida, Feb. 12-15, 2018.

[50] Lin, J., Wang, X.Q., and Mignolet, M.P., "Nonlinear Reduced Order Modeling of a Cylindrical Shell Exhibiting Mode Veering and Symmetry Breaking," *Proceedings of the International Modal Analysis Conference, IMAC XXXVII*, Orlando, Florida, Jan. 28-31, 2019.

[51] Lin, J., Wang, X.Q., and Mignolet, M.P., "Nonlinear Reduced Order Modeling of Strongly Nonlinear Behavior: A Revisit of a Curved Beam Example," *Proceedings of the International Modal Analysis Conference, IMAC XXXVI*, Orlando, Florida, Feb. 12-15, 2018.

[52] Cook, R.D., Malkus, D.S., Plesha, M.E., and Witt, R.J., Concepts and Applications of Finite Element Analysis, 4th Edition, Wiley&Sons, 2002.